ABSTRACT

Studying parton energy loss in hot nuclear matter using dihadron correlations

Oana Catu
Yale University
June 2008

Results from the experiments at RHIC showed evidence that a strongly interacting medium is formed in ultra-relativistic heavy ion collisions at RHIC energies. Di-hadron correlations provide major contributions to the support of this claim. Namely, on the away-side of a high transverse momentum (p_T) trigger hadron, the associated jet-like hadron yield is strongly suppressed at high p_T in heavy ion collisions, as opposed to d+Au collisions which show behavior similar to p+p collisions. These two facts indicate that the suppression is a result of the scattered parton losing energy in the medium. Various theoretical calculations presently available attempt to use present data in order to estimate the initial gluon density. We attempt to constrain the models by using the dependence of the parton energy loss on the path length through the medium. To this end, we present a systematic study of the near- and away-side di-hadron correlation yields as a function of number of participant nucleons (N_{part}) for 3 systems with different geometries (d+Au, Cu+Cu and Au+Au) at $\sqrt{s_{NN}} = 200GeV$ in STAR. Taking the method one step further, we investigate the modification of the away-side di-hadron fragmentation functions for high p_T particles in Au+Au and Cu+Cu. A comparison with theoretical predictions using NLO pQCD is also presented. The calculation allows the determination of the transport coefficient of the medium ($\hat{q}$) using previous Au+Au data. We compare it with our data for the various centralities in Au+Au and Cu+Cu, corresponding to various N_{part} and different geometries. The data presented in this work puts constraints on the different models and will allow a more quantitative description of the properties of the matter formed in ultra-relativistic heavy ion collisions.

Studying parton energy loss in hot nuclear matter using dihadron correlations

A Dissertation
Presented to the Faculty of the Graduate School
of
Yale University
in Candidacy for the Degree of
Doctor of Philosophy

By
Oana Catu

Dissertation Director: John Harris

June 2008

Acknowledgements

The past six years have been a time of discovery and growth, as a PhD should be. The people I encountered on this road made the trip easier, fruitful, and frankly, much more fun. First of all I would like to express my gratitude to my adviser, John Harris, for giving me the opportunity to join his group and making it possible for me to pursue a PhD at Yale. Thank you for your support and understanding, giving me great opportunities to learn and participate in conferences, and for fostering such a great environment in the group. My deepest gratitude to Helen, from whom I learned so much, be it about heavy ion physics, analysis techniques or programming. Thank you for your patience, thank you for putting up with me during the time we shared an office, thank you for being so supportive and encouraging and thank you for being such a great inspiration. Also thank you for being so down to earth and approachable and fun. You are a great example for women in science and I'm sure you'll have a great career and be the most loved professor. A very important person for the work on my thesis has been Marco van Leeuwen, who was incredibly helpful with all of his suggestions as the high-p_T physics working group convener in STAR. Thank you so much for all your help, for all the suggestions on my work - they were always spot on and help me progress. I wouldn't have done this work without your helpful supervision.

Among my peer graduate students, I want to thank Christine Nattrass for being a great friend and the most fun officemate, for letting me crash at her place, for being supportive when I was down, bringing cinnamon rolls and having great dinner parties. Also, thank you for sharing your knowledge of computers, for all your work for the computer cluster and extracting data files and moving them to our

computers, you've been essential for the productivity of the group. I'm sure I will never find such a great officemate and I will surely miss you. I would like to thank other present or past members of the group for their help and for being a wonderful family during my time at Yale. Richard Witt, thank you for all your patience answering questions about software, Mike Miller, thank you for introducing me to analysis in this field. Sevil Salur, thank you for being always encouraging and helpful; Christina Markert, thank you for bringing your fun attitude to the group and initiating the RHIG annual dance parties. Jana Bielcikova, thank you for your helpful collaboration, especially as the working group convener. Jon Gans, Betty Abelev, Mark Heinz, Boris Hippolyte, Matt Lamont, Nikolai Smirnov, Thomas Ullrich, Jaro Bielcik, Joern Putschke, Elena Bruna, thank you all for making the RHIG group the best group to work in.

On a personal note, I would like to thank my parents for always being supportive of my dreams and always doing the best they can to help me achieve my goals and be happy. *Mama, multumesc pentru ca ai fost totdeauna alaturi de mine, chiar si cand nu meritam, si m-ai ajutat sa fac tot ce mi-am propus. Tata, multumesc pentru ca ai facut tot ce ti-a stat in puteri sa-mi fie bine si sa ma ajuti.* I can't forget to thank the women who raised me for 13 years, *Mami*, she is my role model of strong but warm, generous and caring woman, and is responsible for me turning out surprisingly well.

Raluca Ilie, thank you or being the most wonderful friend through all these years, thank you for your support and friendship in bad times and good times. I'm lucky to have such a friend. My friend Rachel Lash (Maitra), thank you for all the good times we spent in New Haven, and thank you for being so wonderfully supportive when I was sad. My awesome friend and tango partner Brian McCarthy - thank you for all the great conversations and all the fun times dancing or laughing our hearts out. Thank you for your friendship, for never letting me down and always being there to count on when I really needed help. You've been a great moral support and a moral compass. Now when I am writing this, after such a hectic period in which my friendships have suffered because of my crazy schedule, I truly appreciate the luck of having such wonderful friends, and the importance of keeping them in my life. Thank you all for being a part of my life, I'll do much

more to keep you in my life - you're too great to just let you slip away because of circumstances or because there are so many thousands miles between us now.

Last, but definitely not least, I'd like to thank Luke Iepuras Theogarajan, my partner in life and crime. Thank you for being so loving and caring, for always being there for me, especially through this difficult and busy last year, for your understanding and support of my career choices, and of course for your help with Latex and Illustrator tricks. I'm so incredibly lucky that I met you, the most warm, generous, smart, funny and crazy human being. This is an appropriate ending of this part of my life and a great new start.

Contents

List of Figures

Chapter 1

Introduction

The Standard Model (SM) of particle physics is at the base of our understanding of the world and it has proved remarkably successful. Since its conception in the '70s, it has been confirmed by experiments of increasing precision. In the near future, the Large Hadron Collider (LHC) at CERN, Geneva, will offer an exciting opportunity to test the SM at much higher energies and search for the Higgs, the only particle in the SM framework that has not been experimentally detected. The SM provides us with a coherent picture of the particles that make up the observable matter in the universe, and three of the four fundamental interactions: electromagnetic, weak and strong interactions. Gravitation still eludes physicists' attempts of a Grand Unification of all known forces, such attempts constituting one of the major research efforts today. A schematic picture of the fundamental particles and the particles that mediate each interaction is presented in Fig. 1.1. The quarks and leptons are divided into three families. The corresponding particles from the three families have similar properties but different masses, their masses increasing from family I to family II and then family III. The mediating particles for each force are also listed: the photon (γ) for the electromagnetic force, the weak bosons W^+, W^- and Z for the weak force, and the gluons for the strong force.

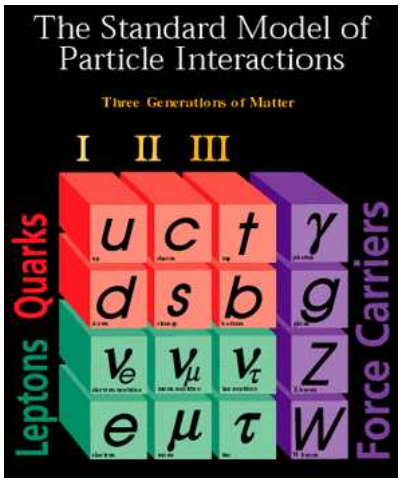

Figure 1.1: Schematic representation of the fundamental particles and interactions described by the Standard Model.

1.1 Quantum Chromodynamics

The focus of this work is the strong interaction, which acts between quarks and is mediated by gluons. The theory of the strong interaction is Quantum Chromodynamics (QCD), which is a non-abelian gauge field theory. QCD has emerged as an exquisite solution to what was a very confusing experimental data landscape in the 1960's. The concept of quarks was proposed in the early 60's by Murray Gell-Mann and George Zweig as a way of understanding the plethora of particles discovered in the previous decades. The new concept, along with the concept of color charge associated with quarks, provided a way to understand the various baryons and mesons as different configurations of three quarks, and a quark and antiquark, respectively. Still, even after deep inelastic scattering experiments led by J. Friedman, H. Kendall and R. Taylor at SLAC in 1969 showed that protons have a sub-structure and therefore quarks are indeed physical entities, there were many puzzling observations left unexplained. One of the main mysteries was the failure to observe free quarks - although quarks were proved to exist inside nucleons, all attempts to observe free quark-like particles in high energy experiments failed - instead, only bound states of quarks (or quarks and antiquarks) were observed. This result is known as the principle of confinement. Paradoxically, although quarks

seemed to interact strongly with each other when attempts were made to separate them, in deep inelastic scattering experiments they seemed to behave like free particles - in fact, with increasing energy of the incoming electrons, their observed behavior became more and more like that of free particles. This peculiar behavior was named "asymptotic freedom".

The apparent contradiction between confinement and asymptotic freedom was solved in 1973 when David Gross, Frank Wilczek, and David Politzer discovered that a class of quantum field theories presented the property of asymptotic freedom and formulated Quantum Chromodynamics, the theory of the strong interaction. We understand quarks in the framework of QCD as particles that carry color and interact with each other via gluons, which are massless bosons. What gives QCD its unique characteristics, compared to the quantum field theories describing the other two forces in the Standard Model (the electromagnetic and the weak force), is the fact that gluons themselves carry color charge. This property leads to anti-screening, opposite to the well-known screening of electrical charges in the case of Quantum Electrodynamics (QED). In QED, a free electric charge is surrounded by a cloud of virtual photons, which screen the charge and therefore the field created by the charge has a magnitude that decreases with distance from the source. Since gluons carry color, the cloud of virtual gluons surrounding a free color charge is self-reinforcing, and therefore the color field increases with distance from the source. Confinement comes as a natural consequence of the theory, since separating two quarks would require an infinite amount of energy.

QCD is a gauge theory based on the SU(3) group, with three colors and eight gluons. It is a quantum field theory characterized by the following Lagrangian:

$$\mathcal{L}_{QCD} = \sum_f \imath\bar{\psi}_f(\gamma^\mu D_\mu - m_f)\psi_f - \frac{1}{4}F^\alpha_{\mu\nu}F^{\mu\nu}_\alpha \tag{1.1}$$

with D_μ and $F_{\mu\nu}$ defined as

$$D_\mu\psi \equiv (\partial_\mu - \imath g A^\alpha_\mu T^\alpha)\psi \tag{1.2}$$

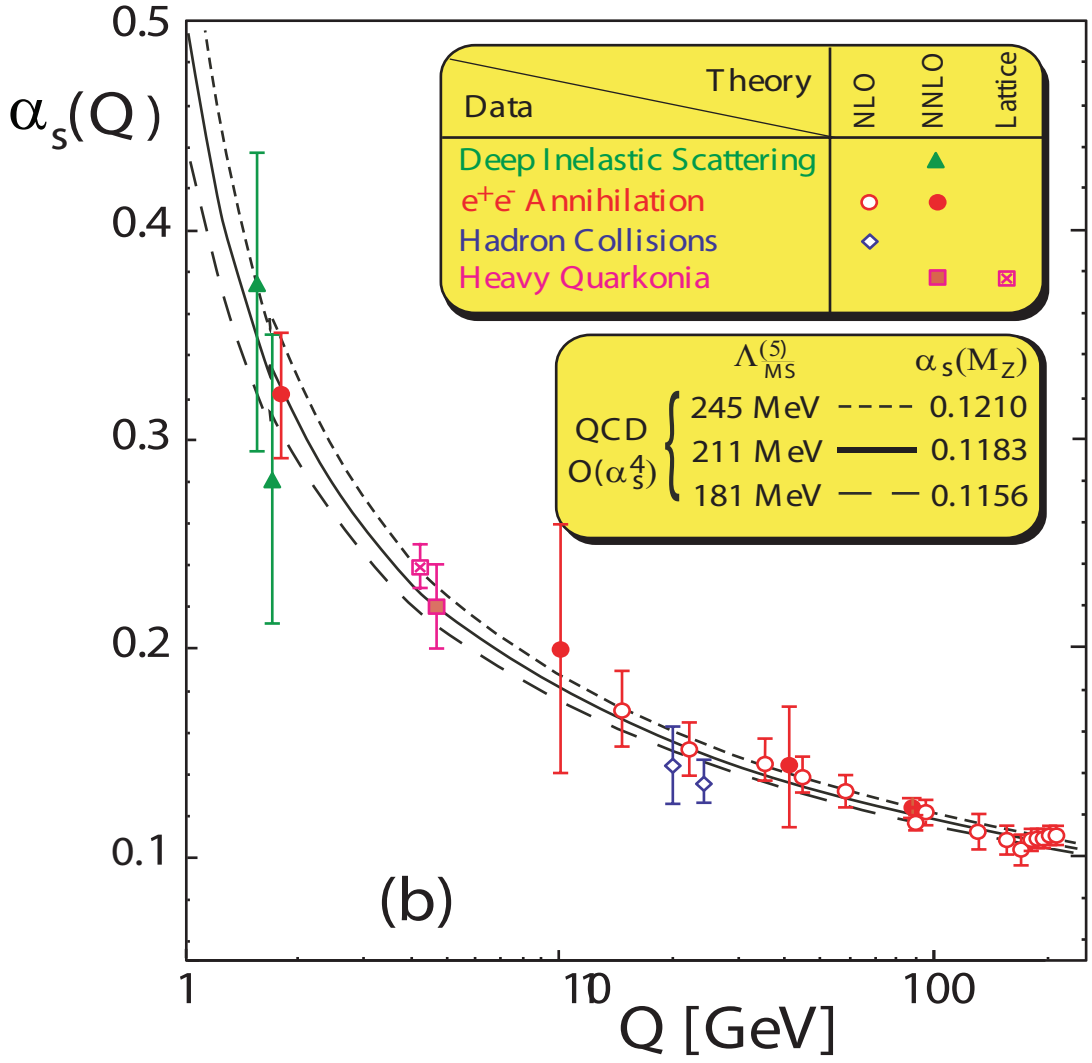

Figure 1.2: The running QCD effective coupling constant - $\alpha_s(Q)$ vs. Q [1].

$$F_{\mu\nu} \equiv \partial_\mu A_\nu - \partial_\nu A_\mu + g f^{abc} A^b_\mu A^c_\nu \tag{1.3}$$

where D_μ is the covariant derivative, $F_{\mu\nu}$ is the field strength tensor, A_μ are gluon vector fields, f is the flavor index (up, down, strange, charm, top and bottom), m_f are the quark masses, T^α are the 8 SU(3) generators, f^{abc} are the SU(3) structure constants, and g is the QCD coupling constant.

Calculating cross sections for various QCD processes involves calculating matrix elements for various Feynman diagrams - and in principle summing over all orders. Divergences in integrals involved in higher order loop diagrams lead to what are called "renormalization schemes" - removing the divergences by reframing the integrals in terms of an arbitrary mass scale μ. Since the cross section has to be independent of the arbitrary chosen parameter, these schemes lead to the Renormalization Scheme Equation(RGE) $\mu\frac{d\sigma(p,\mu)}{d\mu} = 0$. The divergences are practically incorporated in the dependence on the scale of the *effective coupling constant* $\alpha_s(\mu) = \frac{g^2}{4\pi}$. To lowest order, α_s is given by

$$\alpha_s(\mu^2) = \frac{\alpha_s(\mu_0^2)}{1+\beta_1/4\pi\alpha_s(\mu_0^2)\log(\mu^2/\mu_0^2)},\ \beta_1 = \frac{11N_c - 2n_f}{3} \tag{1.4}$$

where N_c is the number of colors, n_f is the number of quark flavors, and $\alpha_s(\mu_0)$ is a boundary condition of the differential equation. Because α_s appears to depend on both $\alpha_s(\mu_0^2)$ and μ_0^2, this is often rewritten as

$$\alpha_s(\mu^2) = \frac{4\pi}{\beta_1\log(\mu^2/\Lambda^2)},\ \Lambda = \mu_0 e^{-2\pi/(\beta_1\alpha_s(\mu_0^2))} \tag{1.5}$$

where Λ is the famous "scale constant" in QCD. Fig. 1.2 shows the running of α_s with Q, where Q is a measure of energy scale and is defined as $Q^2 = -q^2$. q^2 is the four-momentum transfer in a strong interaction. Both confinement (strong coupling at small momentum scales or large distances) and asymptotic freedom (weak coupling at high momentum scales or short distances) are encompassed in the scale dependence of the QCD running coupling constant.

1.2 Quark Gluon Plasma

In order to understand the strong interaction and its consequences, physicists have tried to infer the properties of thermally equilibrated nuclear matter and construct the "QCD phase-diagram". The experimental data available and the theoretical predictions based on QCD have led to our current image of the QCD phase diagram shown in Fig. 1.3. At high temperatures and small baryon chemical potential μ_b -

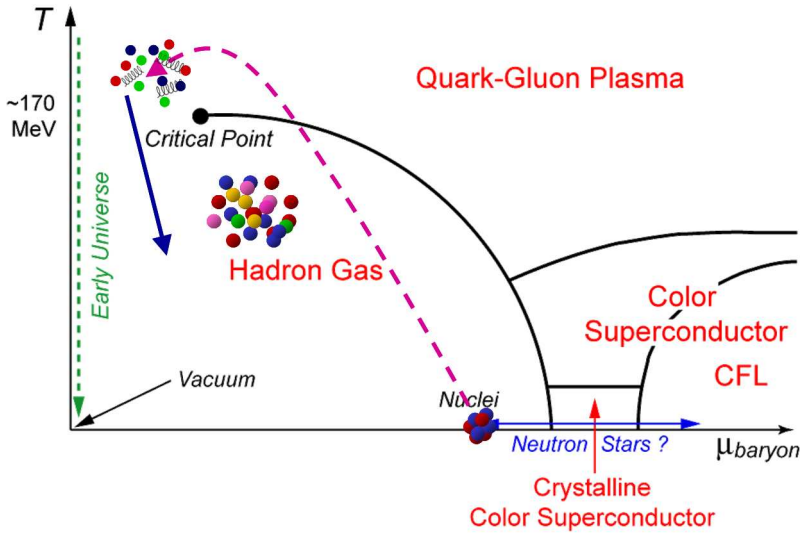

Figure 1.3: Sketch of QCD phase diagram.

conditions that existed in the very early universe - a state of deconfined quarks and gluons is believed to exist. Inferred initially from the asymptotic freedom behavior of QCD, the existence of a phase transition to such a state, called Quark Gluon Plasma (QGP), was later confirmed by lattice QCD calculations. Due to the running nature of the strong coupling constant, analytic calculations in QCD are possible only for high energy processes, where the coupling is small enough to allow a perturbative analysis. In the non-perturbative regime, the calculations are performed numerically by calculating path integrals on a lattice representing the discretized space-time coordinates. These methods require ample computing resources and have undergone a great development in recent years. Such calculations show that there is indeed a predicted transition of some form between a hadronic and a QGP phase, occurring at a temperature in the vicinity of $T_c \sim 160$ MeV for zero chemical potential. The precise value of the transition temperature depends on the treatment of quarks in the calculation. The dependence of the energy density ϵ divided by T^4 rises rapidly around T_c, then saturates, but at values substantially below the Stefan-Boltzmann (ideal gas) limit (see Fig. 1.4). The deviation from the SB limit indicates substantial remaining interactions among the quarks and gluons in the QGP phase.

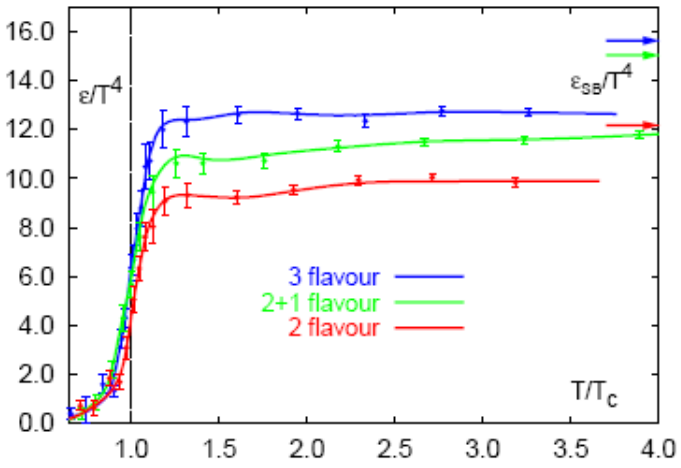

Figure 1.4: The energy density divided by T^4 (ϵ/T^4) in QCD from lattice calculations as a function of T/T_c. The number of degrees of freedom ($\propto \epsilon/T^4$) rises steeply for temperatures larger than T_c. Arrows indicate the ideal gas values of energy density for the three cases shown. Figure is taken from [2].

Chapter 2

Heavy ion collisions

Ultra-relativistic heavy ion collisions were seen as a tool to explore the QGP in the laboratory. The collisions deposit a large energy in a very small region, creating matter at temperature and energy density well above the hadronic phase transition. Fig. 2.1 shows a sketch of a heavy-ion collision, depicting the two nuclei Lorentz contracted [1] in the center of mass frame. The nucleons in the overlapping region are called participant nucleons, whereas the other non-interacting nucleons are called

[1] The sketch just indicates the fact that the nuclei are Lorentz contracted, however it is not drawn to scale (the width of the nucleus does not accurately represent the amount of contraction).

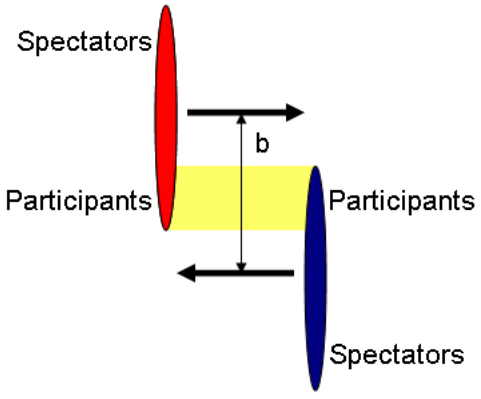

Figure 2.1: Illustration of a heavy ion collision. The two nuclei are Lorentz contracted in the center of mass frame. The impact parameter b and the participant and spectator regions are indicated.

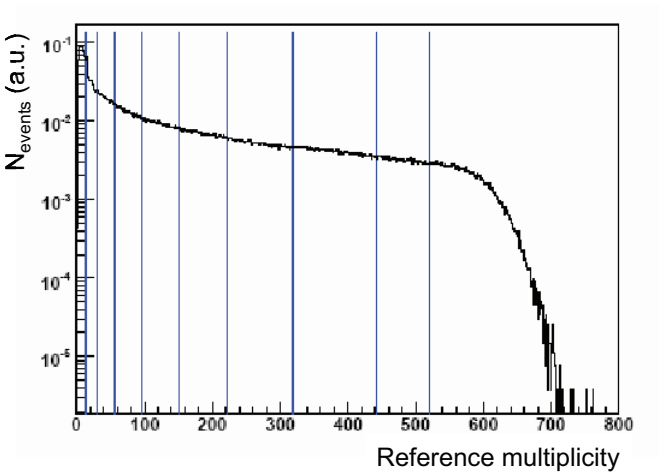

Figure 2.2: Uncorrected (reference) multiplicity distribution for Au+Au collisions at $\sqrt{s_{NN}}$ = 200 GeV. Blue lines separate the centrality bins. The bins are 80-100%, 70-80%, 60-70%, 50-60%, 40-50%, 30-40%, 20-30%, 10-20%, 5-10%, and 0-5% most central collisions from left to right. The uncorrected charged particle multiplicity per unit pseudo-rapidity is plotted on the x-axis, whereas the number of events (in arbitrary units) is plotted on the y-axis.

spectators. Collisions with a large overlap region are referred to as central collisions, whereas those with few participant nucleons are called peripheral collisions. The centrality of the collision is determined by the impact parameter b. Since the impact parameter is not known a priori, and cannot be measured on an event by event basis, the number of produced particles (the multiplicity) is used as a selection criterion to select collision centrality classes. The STAR collaboration, of which I am a member and whose data is the basis of this work, uses the charged particle multiplicity in the pseudorapidity region $|\eta| < 0.5$ for centrality selection. Fig. 2.2 shows the reference multiplicity distribution for Au+Au collisions at $\sqrt{s_{NN}}$ = 200 GeV, and the centrality bins containing the specified percentage of the total cross-section. The average impact parameter and number of participants (N_{part}) for each centrality bin are calculated using Monte Carlo simulations based on a Glauber model describing the geometry of the collisions [3]. The highest multiplicities correspond to the most central collisions.

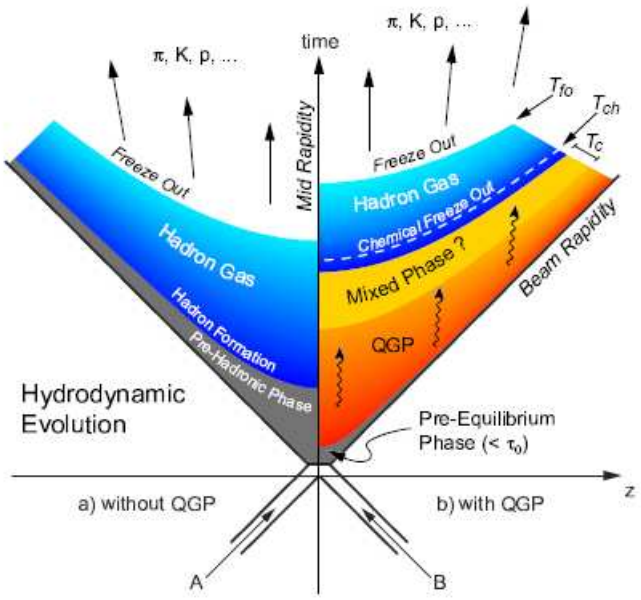

Figure 2.3: Light-cone diagram of a collision (a)without QGP formation and (b)with QGP formation. T_{fo} and T_{ch} represent the thermal and the chemical freeze-out temperatures, whereas T_c is the critical temperature for a transition from QGP to hadronic matter.

2.1 Experimental results

The experimental results available since 2000 from the Relativistic Heavy Ion Collider have produced much excitement in the field, providing convincing evidence for the creation of a new state of matter. Some of the results have also been surprising, constituting the driving force in the attempt to understand the properties of QCD matter under extreme conditions. The task of determining the properties of the new state of matter formed in the collisions is not an easy one. A collision of heavy nuclei (up to A=197 for Au) at energies up to 200 GeV in the center of mass for each colliding nucleon pair results in the production of 1000 particles per pseudorapidity unit. The experimentalist's task is to infer the properties of the hot and dense medium created in the early stages of the collision, by measuring the particles resulting from the collision.

Fig. 2.3 presents a light-cone diagram of a collision, considering two scenarios:

(a)without formation of a QGP and (b)with the formation of a QGP state. The QGP medium expands and cools, and hadronizes upon reaching the critical temperature T_c (under the simplifying assumption of a sudden hadronization, in reality the details of the hadronization process are not fully understood). The system continues to expand and cool, reaching the chemical freeze-out temperature T_{ch}, after which point the particle ratios are constant and no flavor changing reactions occur. Upon further cooling, the system reaches the thermal freeze-out temperature T_{fo}, after which no more interactions occur and the particles free-stream to the detectors. The experimental data used in trying to determine the properties of the hot medium can be divided into two categories: bulk observables and hard probes. Bulk observables focus on produced particles with transverse momenta $p_T < 2$ GeV/c, which are the vast majority of the produced particles, and which exhibit collective behavior. Hard probes refer to highly energetic, rare processes that occur in the initial parton hard scatterings and that can act as "probes" of the medium formed. In this work, the focus will be on one such hard probe: back-to-back partons, resulted from hard parton scatterings, that lose energy while passing through the medium. Understanding the energy loss mechanism can provide information on the properties of the medium.

2.2 Bulk properties

A first estimate of the energy density of the medium formed in heavy ion collisions can be obtained using the measurement of transverse energy per unit rapidity. Under certain simplifying assumptions first suggested by Bjorken (longitudinal boost-invariance, free-streaming expansion in which the matter does no work), the initial energy density of the created matter can be estimated as

$$\epsilon_{Bj} = \frac{1}{\tau A_\perp} \frac{dE_T}{dy} \tag{2.1}$$

where $A_\perp$ is the transverse overlap area of the nuclei and τ is the particle formation time. Since the two nuclei are Lorentz contracted to very thin disks, the nuclear overlap will be very thin in the longitudinal direction and very short in duration.

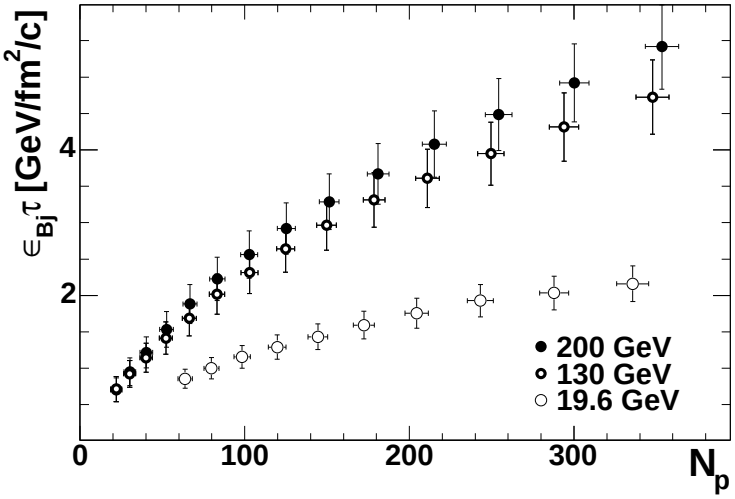

Figure 2.4: $\epsilon_{Bj} \cdot \tau$ as a function of number of participants for three values of $\sqrt{s_{NN}}$. Data are taken from [4]

In this limit, then, we can describe all secondary produced particles as having been radiated out from a very thin disk, and that they are all created at essentially the same time. We can then estimate the local energy density of these created particles if we make one further assumption: that the secondaries can be considered formed at some proper time τ after they are radiated out from the thin source disk. This estimate should be a measure of peak energy density of created particles.

Using the PHENIX measurements of $dE_T/d\eta$ and a conservative estimate of $\tau \approx 1$fm/c, one obtains an estimate $\epsilon_{Bj} = 5\,\mathrm{GeV/fm^3}$ for the initial energy density in central Au+Au collisions at $\sqrt{s_{NN}} = 200\,\mathrm{GeV}$. This value is well above the critical energy density $\epsilon \simeq 1\,\mathrm{GeV/fm^3}$ for the QGP phase, obtained from lattice QCD calculations. In Fig. 2.4, values for $\epsilon_{Bj} \cdot \tau$ are presented as a function of number of participants for three collision energies. As can be seen, the energy density increases with center of mass energy and with centrality (i.e. central collisions with the largest N_{part} reach the highest energy densities).

The measurements of identified particle yields can be used to constrain the temperature at chemical freezout, under the statistical model assumption that the system is in thermal and chemical equilibrium at that stage, and therefore establish

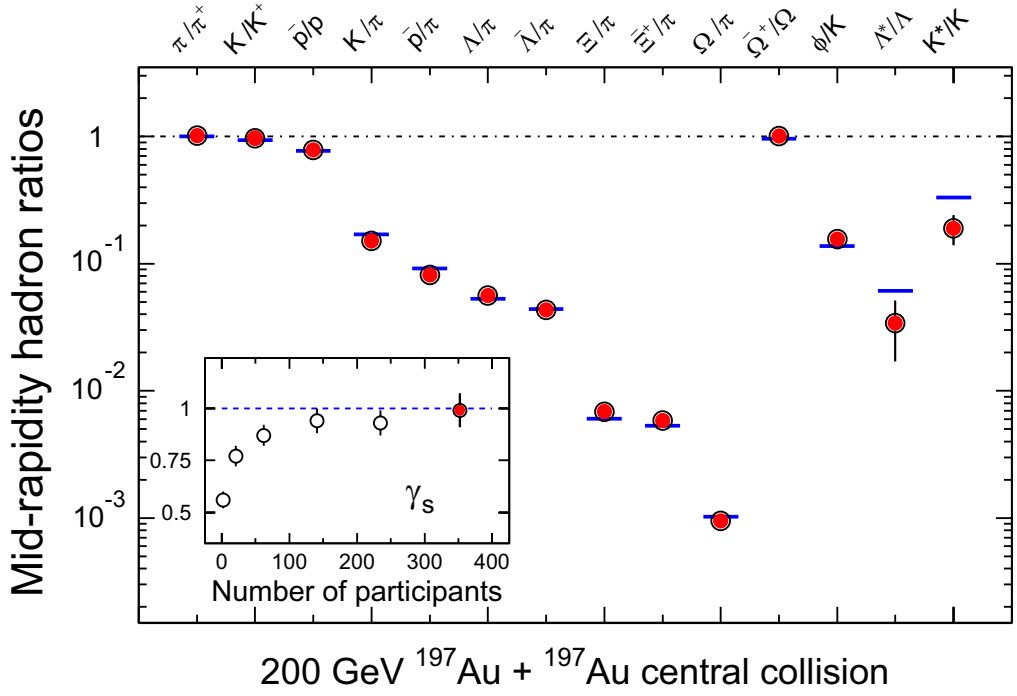

Figure 2.5: Ratios of p_T-integrated mid-rapidity yields for different hadron species measured in STAR for central Au+Au collisions at $\sqrt{s_{NN}} = 200$GeV. The horizontal lines are the statistical model fit to the ratios of the long-lived stable hadrons. The inset presents the dependence of γ_s on N_{part}. Figure taken from [5].

a lower bound on the initial temperature. Fig. 2.5 presents STAR measurements of integrated hadron yield ratios for central Au+Au collisions at $\sqrt{s_{NN}} = 200$GeV. The statistical model fit suggests a temperature $T_{ch} = 163 \pm 5$MeV, consistent with the lattice calculations of the critical temperature for QGP formation. The fact that the statistical model describes the ratios for strange particles, unlike in p+p collisions, is consistent with chemical equilibration of the u, d and s quarks. As shown in the inset of Fig. 2.5, the parameter γ_s, used to quantify the deviation of strange particle yields from the equilibrium predictions, increases with centrality and is consistent with unity for central Au+Au collisions. The saturation of the strangeness sector yields, indicated by the behavior of γ_s, signifies the change from canonical ensemble ($p+p$, $e^+ + e^-$) with hadronization dominated statistical phase space distributions, to grand canonical ensemble (central Au+Au), characterized

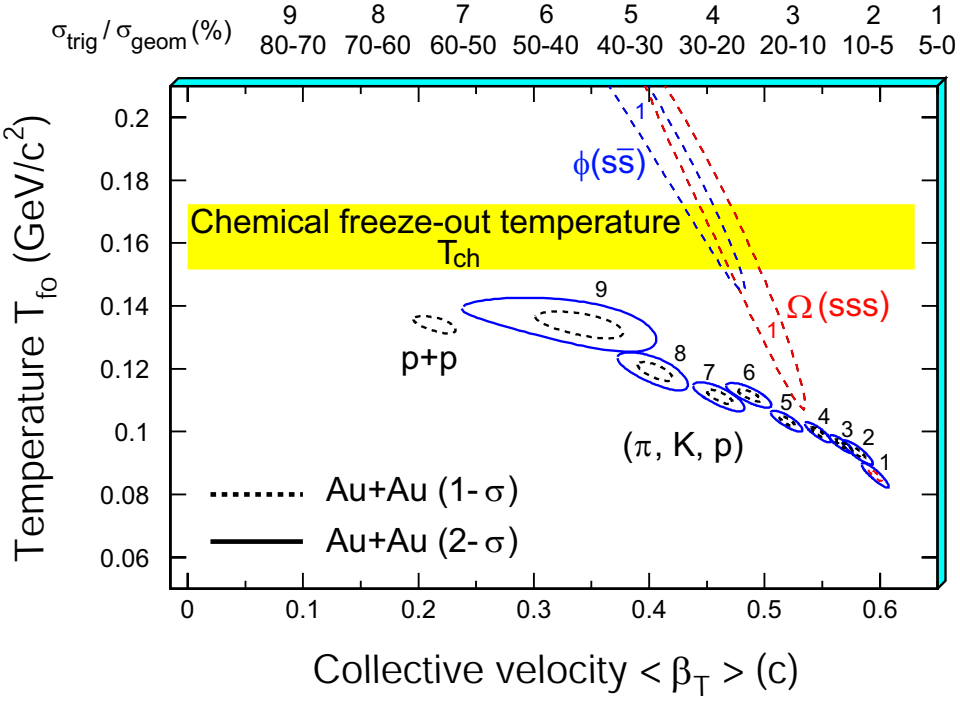

Figure 2.6: Kinetic freezout temperatures and radial flow velocity for different centralities, extracted from a thermal+radial flow fit. The dashed and solid lines represent $1-\sigma$ and $2-\sigma$ contours, respectively. On the top of the plot, the numerical labels indicate the centrality selection for Au+Au collisions at $\sqrt{s_{NN}} = 200$ GeV. For π, K, p 9 centrality bins have been used, whereas for Ω and ϕ only the most central bin is shown. Data from [5].

by (at least approximately) thermal and chemical equilibration.

Information about the system at kinetic freezout can be obtained from the hadron spectra. Hydrodynamics-motivated fits ([6]) to the measured transverse momentum spectra have been performed for various hadron species. The fit parameters are interpreted in an ansatz of an expanding thermal source as the kinetic freezout temperature T_{fo} and the collective radial flow velocity $< \beta_T >$. Fig. 2.6 presents the determined values of these parameters for π, K, p, Ω and ϕ. As the collisions become more central, the bulk of the material, dominated by π, K, p, appears to grow cooler at kinetic freezeout and to develop stronger collective flow. These results may indicate a more rapid expansion with increasing collision centrality.

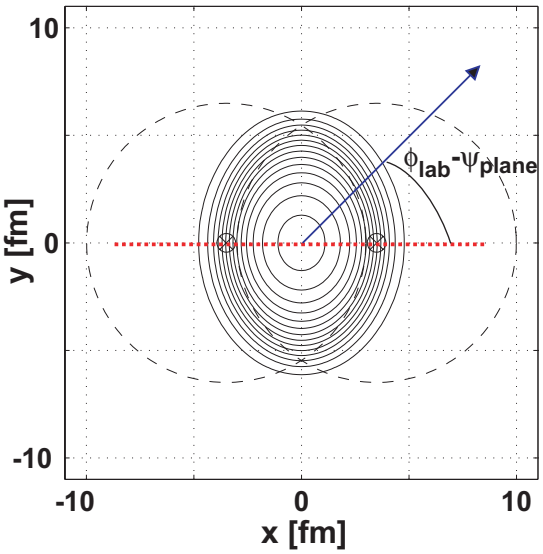

Figure 2.7: The asymmetric overlap region in a non-central heavy ion collision. The red dotted line represents the reaction plane direction.

2.2.1 Elliptic flow

In non-central heavy-ion collisions, the overlap region of the two nuclei is asymmetric in the transverse plane (perpendicular to the beam direction). Fig. 2.7 shows a sketch of a beam's-eye view of the two overlapping nuclei. The reaction plane is defined by the beam direction and the impact parameter. Given the different pressure gradients for different orientations with respect to the reaction plane, the interactions in the overlap region transfer the initial spatial anisotropy into an anisotropy in the final momentum distributions, that can be measured. A figurative illustration is shown in Fig. 2.8 The observed particle yield versus azimuthal angle with respect to the event plane (the experimentally determined reaction plane) can provide information on the strength of the interactions in the early phase of the collision. The anisotropy of the particle yields with respect to the event plane can be described using a Fourier expansion:

$$\frac{d^3N}{p_T dp_T dy d\phi} = \frac{d^2N}{p_T dp_T dy}\left[1 + 2\sum_{\alpha} v_\alpha \cos(\alpha[\phi - \Psi_{RP}])\right]. \tag{2.2}$$

The harmonic coefficients, v_α, are anisotropy parameters, p_T, y, and ϕ are the

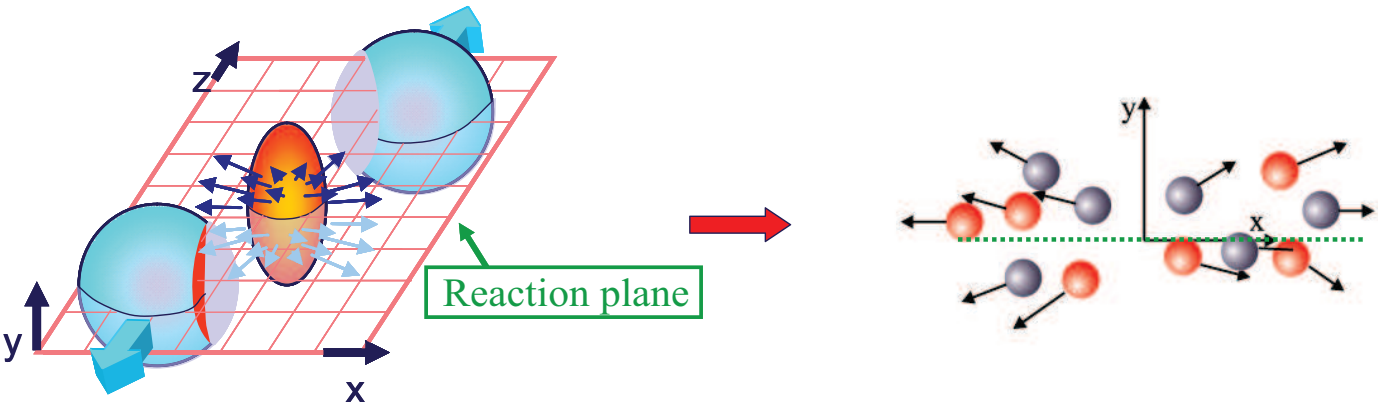

Figure 2.8: Illustration of elliptic flow in a non-central heavy ion collision.

respective transverse momentum, rapidity, and azimuthal angle for the particle, and Ψ_{RP} is the reaction plane angle. Due to the specific geometry of the overlap region, the second anisotropy coefficient, v_2, commonly referred to as *elliptic flow*, dominates the distributions. A more detailed description of the methods used to measure elliptic flow will be given later, since it creates a correlated background for the analysis presented in this work.

The most direct evidence that v_2 is related to spatial asymmetries present early in the reaction is that v_2 at low p_T approximately scales with the initial eccentricity ϵ [2] of the overlapping region. The measured values of v_2 normalized by ϵ are shown in Fig. 2.9 as a function of centrality for two different p_T ranges [7]. At low momentum, v_2/ϵ is independent of centrality to within 20%.

The elliptic flow measured at RHIC energies is about 70% larger than the previous measurements at lower SPS energies, as shown in Fig. 2.10. In contrast to the results at lower energies, hydrodynamic model calculations reproduce relatively well the magnitude of the elliptic flow, while at the same time fitting the various spectra. Fig. 2.11 shows the p_T dependence of v_2 for various hadrons.

The observation of such a large elliptic flow in heavy ion collisions at RHIC is one of the most important results from RHIC. There are several implications of this result. First, the hydrodynamic-based calculations reproduce the data only if they

[2] $\epsilon = \frac{<y^2>-<x^2>}{<y^2>+<x^2>}$

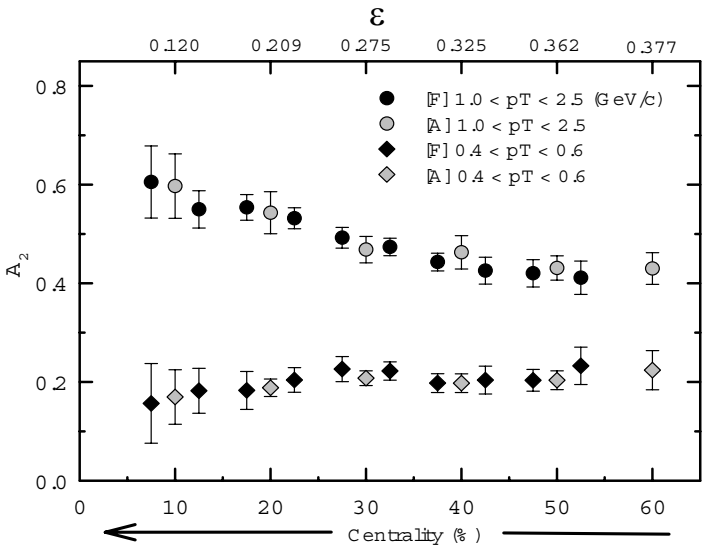

Figure 2.9: $A_2 = v_2/\epsilon$ vs. centrality for Au+Au collisions at $\sqrt{s_{NN}}$ = 130 GeV [7]. The data points come from two different types of two particle correlations: "fixed"-p_T correlations, when both particles have the same p_T (black symbols labeled as "F"), and "assorted"-p_T correlations, when the two particles have different p_T (gray symbols labeled as "A"). In this case the labeled p_T range is for the higher momentum particle of the pair.

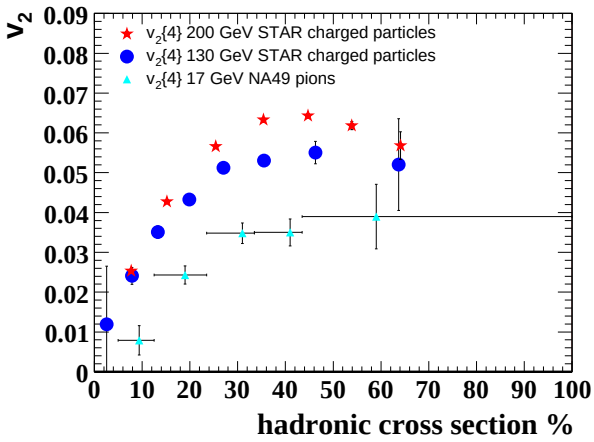

Figure 2.10: Centrality dependence of v_2, integrated over p_T. The triangles are the NA49 measurements for charged pions at $\sqrt{s_{NN}}$=17 GeV. The circles and stars are STAR measurements for charged particles at $\sqrt{s_{NN}}$=130 GeV and 200 GeV, respectively. Figure from [5].

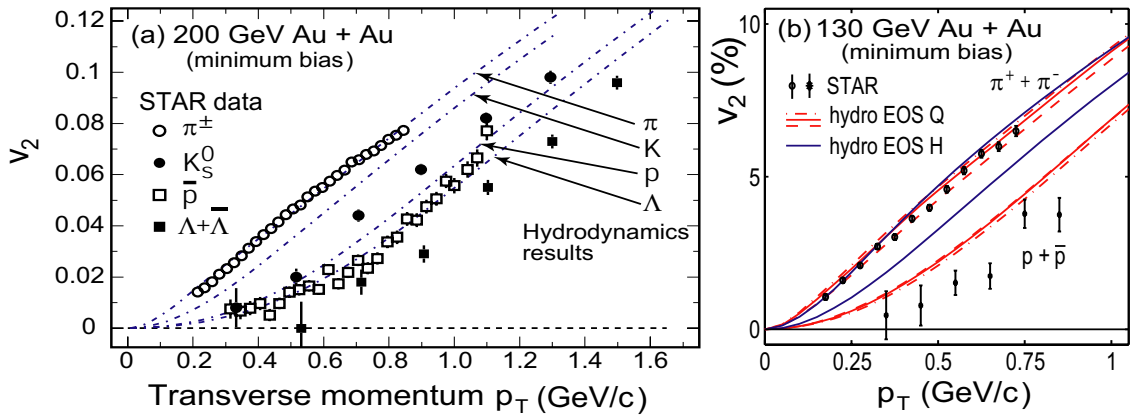

Figure 2.11: a) The p_T dependence of v_2 for $\pi^+ + \pi^-$, K^0_s, $\bar{p}$, and $\Lambda + \bar{\Lambda}$ in 200 GeV Au+Au collisions from STAR. The dashed lines represent hydrodynamics calculations assuming early thermalization, ideal fluid expansion, an equation of state consistent with LQCD calculations including a phase transition at T_c=165 MeV and a sharp kinetic freezeout at a temperature of 130 MeV. b) Hydrodynamics calculations using a hadron gas equation of state (EOS H - blue lines) and an equation of state including the aforementioned QGP phase transition. Figures from [9, 10].

have as their initial condition an equation of state containing a transition to a QGP phase, and fail to describe the data when using a purely hadronic equation of state. Also, the fact that an ideal hydrodynamic approach reproduces the magnitude of the elliptic flow implies local thermalization, and the consistency between the hydrodynamic calculations and the data require that local thermal equilibrium is attained very early (τ <1 fm/c). The early thermalization suggests that the early collision stages are dominated by very strongly interacting matter. The fact that the calculations use ideal hydrodynamics, and even small shear viscosities introduce large deviations from the data, implies very short constituent mean free paths – the matter created is essentially a perfect liquid, free of viscosity [8]. This was a big surprise for the community at large, given the initial rationale behind the search for QGP, which was based on the simplifying assumption that asymptotic freedom leads to a weakly interacting QGP gas. Later studies revealed that strong interactions are consistent with the lattice QCD results (Fig. 1.4) that show only a 20% deviation from the Stefan-Boltzman limit for the energy density.

Another surprising and interesting result appears in an "intermediate" p_T region $1.5-4$ GeV/c (below the p_T region in which fragmentation dominates particle production). In Fig. 2.12, particle-identified elliptic flow measurements for 200 GeV Au+Au minimum-bias collisions are presented by dividing both v_2 and p_T by the number of valence quarks n in the hadron of interest. The apparent scaling behavior seen in this figure for $p_T/n > 1$ GeV/c is intriguing, as the data seem to point to constituent quarks as the degrees of freedom determining the observed hadron flow at intermediate p_T. Several recombination-coalescence models have emerged, explaining this feature and others featuring differences between mesons and baryons. In addition to the well understood fragmentation of hard-scattered partons that give rise to a power-law component of the spectrum, the hadrons in this p_T region are also formed via the coalescence of n constituent quarks of transverse momenta p_T/n, drawn from a thermal (exponential) spectrum [11, 12, 13](see Fig. 2.13).

2.3 Hard Probes

The previous results on global observables show that heavy ion collisions at RHIC create a highly interacting medium that can be described in an ideal hydrodynamics approach and that requires an equation of state with a QGP phase transition. Another class of experimental evidence used to investigate the properties of the medium comes from "hard probes" - partons from hard scattering events early in the collision. These must traverse the medium created and, through their interaction with the medium, provide information on properties of the matter formed in heavy ion collisions. They serve as calibrated probes, since they are well understood processes that can be described using perturbative QCD, which has been shown to describe very accurately hadron production in elementary collisions (p+p). This can be seen in Fig. 2.14, which shows a π^0 spectrum in p+p collisions at RHIC compared with Next to Leading Order (NLO) pQCD calculations.

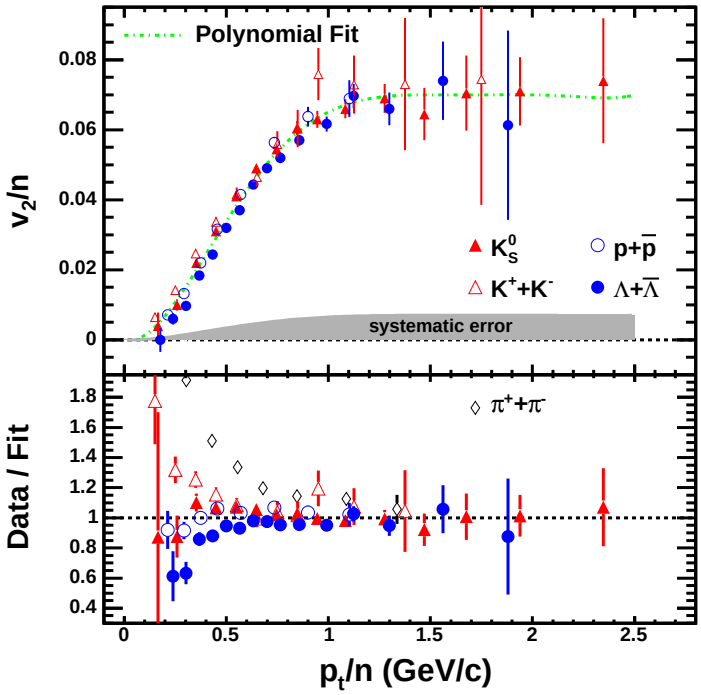

Figure 2.12: Top panel: Identified particle v_2 from minimum bias Au+Au collisions at $\sqrt{s_{NN}} = 200$ GeV. The vertical and horizontal axis have been scaled by the number of constituent quarks (n). A polynomial curve is fit to the data. Bottom panel: The ratio of v_2/n to the fitted curve. Figure from [14].

2.3.1 Hard scattering cross-sections in pQCD

Hard scattering cross-sections cannot be calculated entirely from first principles using pQCD, since they involve a combination of short- and long-distance behavior. However, the QCD factorization theorem allows us to calculate these cross-sections by providing a systematic method of separating (factorizing) the long-distance from the short-distance behavior. The long-distance components cannot be calculated (since they are non-perturbative), they need to be measured experimentally, but QCD can be used to predict their value at an arbitrary energy scale after they have been measured at a particular energy. The non-perturbative components entering the calculation of the hard scattering cross-sections in p+p collisions are the Parton Distribution Functions (PDFs) and Fragmentation Functions (FFs). The

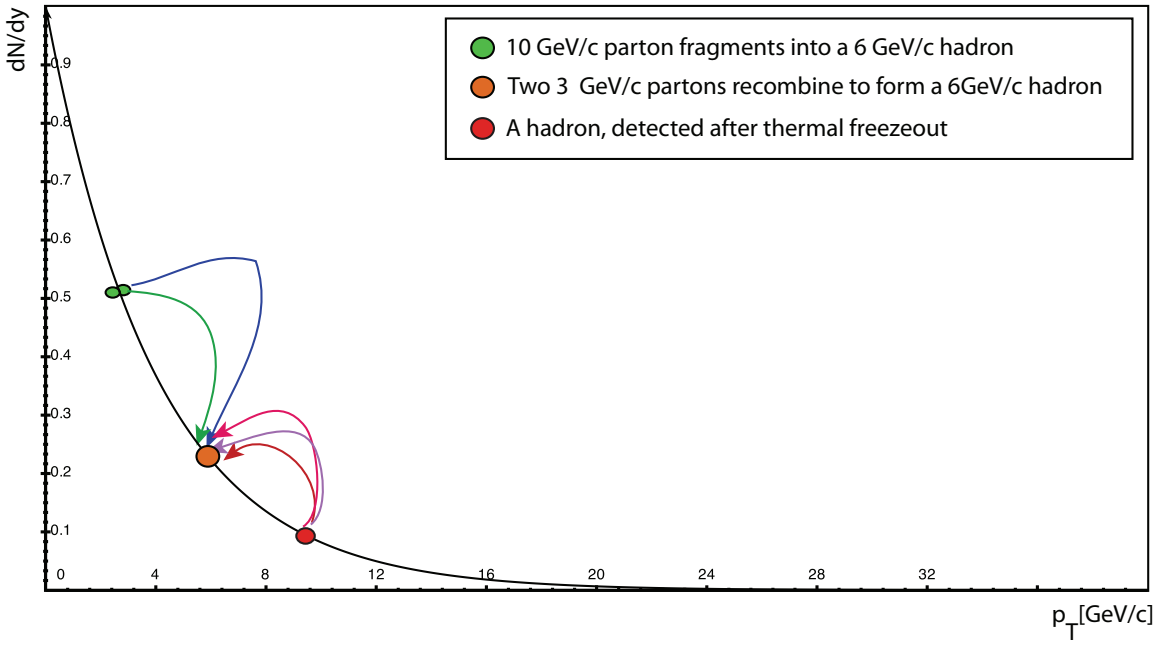

Figure 2.13: A cartoon illustrating possible particle production mechanisms. The blue arrows show two 3 GeV/c partons recombining to form a 6 GeV/c meson. The red arrows represent a 10 GeV/c parton fragmenting to form a baryon of the same p_T as the meson produced via recombination.

PDFs $f_{i/h}(x_i)$ are defined to be the probability density of finding a parton i of momentum fraction x_i in hadron h, where x_i is the Bjorken $x = p_{parton}/p_{hadron}$, $0 < x < 1$. [3] At the other end, the FFs $D_{h/p}(z)$ describe the probability density of a hard-scattered parton p to hadronize (fragment) into a hadron h carrying a fraction z of its momentum ($z = p_{hadron}/p_{parton}, 0 < z < 1$). The semi-inclusive cross-section for a certain particle type, $A + B \rightarrow C + X$ can be then written as

$$\frac{d\sigma}{dy} = \sum_{a,b} \int_0^1 dx_A \int_0^1 dx_B \int_0^1 dz_c \; f_{a/A}(x_A, \mu_F)\; f_{b/B}(x_B, \mu_F)\; \frac{D_{C/c}(z_c, \mu_F)}{z_c} \frac{d\hat{\sigma}_{ab\rightarrow cd}(\mu, \mu_F)}{dy} \tag{2.3}$$

where $d\hat{\sigma}_{ab\rightarrow cd}(\mu, \mu_F)/dy$ (which is calculated perturbatively) gives the cross section for these partons to produce the outgoing partons c and d, which fragment into jets of hadrons.

[3] For nucleons bound in a nucleus, PDFs are modified with respect to free nucleons. They are measured in Deep Inelastic Scattering processes.

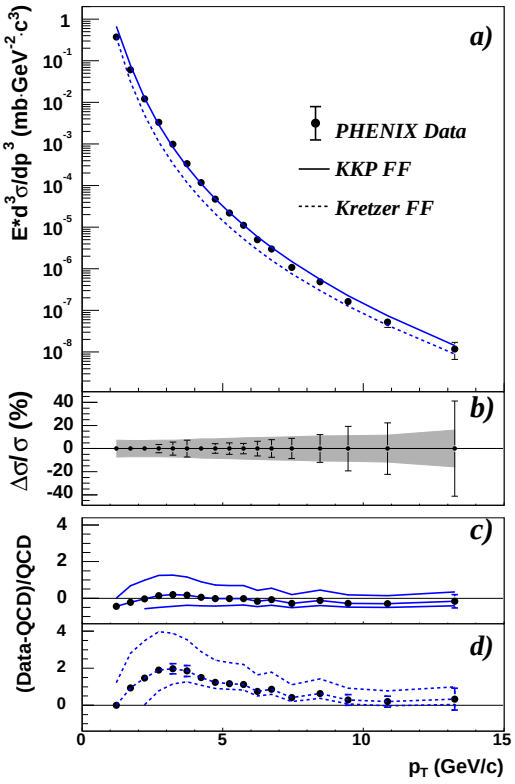

Figure 2.14: Figure taken from [15] comparing results from p+p collisions at $\sqrt{s}$ = 200 GeV with NLO calculations. a) The invariant differential cross-section for inclusive π^0 production (points) and the results from NLO pQCD calculations using the Kniehl-Kramer-Potter (solid line) and Kretzer (dashed line) sets of fragmentation functions. b) The relative statistical (points) and point-to-point systematic (band) errors. c,d) The relative difference between the data and the theory using KKP (c) and Kretzer (d) fragmentation functions with renormalization and fragmentation scales of 1/2 p_T(lower curve), p_T, and 2p_T(upper curve). In all figures, a normalisation error of 9.6% is not shown

2.3.2 Hard probes results

Given that hard-scatterings are point-like events, the cross section for hard scatterings in nucleus-nucleus collisions is given by the number of possible point-like nucleon-nucleon collisions times the nucleon-nucleon cross-section from Eq. 2.3. Deviations from this scaling observed for heavy ion collisions will indicate medium

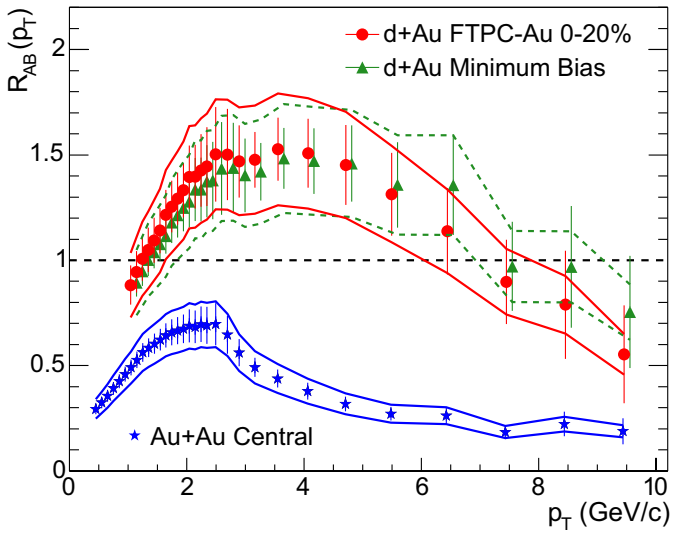

Figure 2.15: Nuclear modification factor $R_{AB}(p_T)$ (Eq. 2.4) of charged hadron inclusive yields from 200 GeV Au+Au and d+Au from STAR[5].

effects. To quantify these effects, one can define the "nuclear modification factor"

$$R_{AB} = \frac{d^2N_{AB}/d\eta dp_T}{< N_{coll} > d^2N_{pp}/d\eta dp_T} \tag{2.4}$$

where $<N_{coll}>$ is the average number of binary nucleon-nucleon collisions for a centrality class.

Figure 2.15 shows STAR measurements of the nuclear modification factor R_{AA} for Au+Au and d+Au collisions. The data shows that in Au+Au central collisions the high p_T hadron yield is suppressed by a factor of ~ 5 with respect to the expectation of binary collision scaling discussed above. Since the d+Au yields do not show a similar suppression, the suppression cannot be a result of initial state nuclear effects, but rather it is a result of final state interactions in the medium formed in Au+Au collisions. The intermediate p_T enhancement seen in d+Au is an effect of initial state nuclear effects, such as the Cronin effect[16] and anti-shadowing of the parton distribution functions [17]. Further results from PHENIX show (Fig. 2.16) the high-p_T hadron suppression increases with N_{part}, and therefore with centrality and size of the participant region.

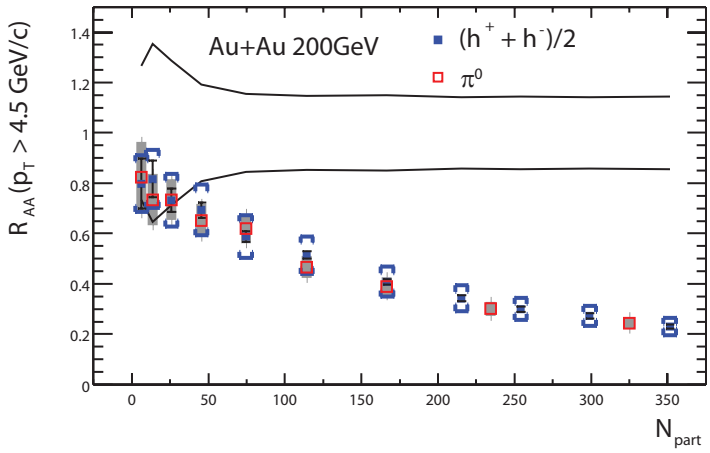

Figure 2.16: Nuclear modification factor in Au+Au collisions as a function of N_{part}[15].

A seminal result from STAR was the discovery of away-side suppression in azimuthal high-p_T dihadron correlations. Fig. 2.17a shows the azimuthal distribution of charged hadrons with $p_T > 2$ GeV/c relative to a "trigger" hadron with momentum $4 < p_T < 6$ GeV/c in p+p, central d+Au and central Au+Au collisions. In a p+p collision, the hard-scattered partons fragment into collimated jets of hadrons. The hard-scattering events with highest cross-section are those with two back-to-back partons in the final state, leading to back-to-back jets. The initial parton momentum distribution inside the nucleons leads to a smearing of the η correlations of the two resulting jets, but their azimuthal back-to-back correlation is preserved (it is just slightly modified by initial and final state scattering). Therefore, a dijet event will result in dihadron correlations with two peaks, at $\Delta\phi \approx 0$ and $\Delta\phi \approx \pi$. The p+p and d+Au data indeed have this characteristic, while the central Au+Au data shows a complete suppression of the away-side peak ($\Delta\phi \approx \pi$). This striking fact reinforces the previous results on the suppression of the nuclear modification factor and suggests that the suppression is due to final state interaction of hard-scattered partons in the dense medium generated in Au+Au collisions. In this case, the high-p_T surviving hadrons come mostly from the surface of the interaction region, leading to an unmodified near-side peak, while the back-scattered parton has to traverse the medium and loses energy, leading to a dramatically suppressed away-side peak.

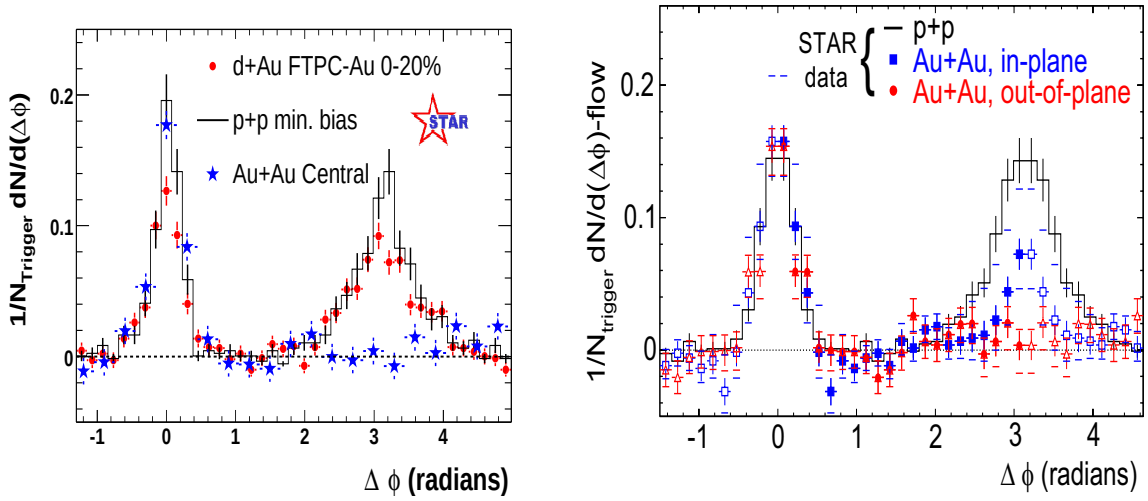

Figure 2.17: (a) Dihadron azimuthal correlations at high p_T for p+p, central d+Au and central Au+Au collisions (background subtracted). (b) Background subtracted dihadron azimuthal correlations for different directions of the trigger particle with respect to the reaction plane in Au+Au collisions. Figure from [5].

The lost energy re-emerges in softer hadrons.

Fig. 2.17b shows dihadron azimuthal distributions in Au+Au collisions for two directions of the trigger hadron: in the reaction plane (”in-plane”) and perpendicular on the reaction plane (”out-of-plane”). The away-side peak is more suppressed for the out-of-plane trigger than for the in-plane one. This is consistent with the partonic energy loss picture: the path length in medium for a jet oriented out of the reaction plane is longer than in the reaction plane (see Fig. 2.7), leading to correspondingly larger energy loss.

The suppression of high-p_T hadrons and of the away-side dihadron correlations are novel phenomena first seen in heavy ion collisions at RHIC energies [3, 18]. They indicate the formation of an extremely dense medium, and the only currently known mechanism that can describe the magnitude of these effects is partonic energy loss in a colored QCD medium.

2.4 Partonic energy loss

The exciting results from RHIC have initiated intense theoretical research aimed at describing and quantifying the energy loss suffered by a parton traversing dense QCD matter. In 1982 Bjorken first proposed that a final state parton would suffer collisional energy loss via elastic scatterings in a deconfined quark-gluon plasma. Later studies [19] focused on radiative energy loss due to multiple interactions with color charges in the high-density medium, which is thought by some theorists to be the dominant energy loss mechanism [20, 21]. There are others who suggest that the collisional energy loss is comparable [22]. There has been much progress in recent years and various approaches to modeling the radiative energy loss have emerged [23, 19]. The Landau-Pomeranchuk-Migdal (LPM) effect (coherence effect) is shown to be of critical importance to the magnitude of the energy loss and is incorporated in the calculations. The total energy loss in a finite medium is calculated to be proportional to L^2, where L is the path length in the medium. However, the treatment of the energy loss in heavy ion collisions is more complicated since the medium is rapidly expanding; the energy and charge densities decrease rapidly in time due to the medium expansion, leading to a weaker dependence on L. There are many different calculations of medium-induced energy loss currently available. They are based on a variety of assumptions about the thickness of the medium, or the coherence in the radiation process itself. The different calculations also use different approximations of the density of the reaction region, its time-dependence due to the medium expansion etc. [20, 21, 24].

2.5 Scope of present work

The theoretical approaches use different assumptions to model the path length distribution of the hard scattered parton. The predictions for the correlated yield measured experimentally is a weighted average of the energy loss over the path length distribution. It is therefore important to study systems with different average path lengths in order to learn more about the path length dependence of energy

loss. In order to constrain the models, we investigate Cu+Cu and Au+Au collisions, systems with similar numbers of participant nucleons but different geometries. The combination of these measurements with measurements of inclusive hadron suppression may allow us to determine whether elastic or radiative energy loss is dominant. The hard-scattered parton will be associated with a jet of hadronic particles in the lab. The jet will contain contributions from both the fragmentation products of the parton and the fragmentation products of the bremsstrahlung gluons, since the angular spectrum of radiated gluons is nearly collinear with the direction of the fast parton. These jets will be characterized by a shift to softer fragmentation. Since full jet reconstruction using classical jet finding algorithms is problematic in the high multiplicity environment at RHIC, we use the hadron-triggered fragmentation function ("dihadron fragmentation function") defined[25] as

$$D_{AA}(z_T, p_T^{trig}) \equiv p_T^{trig} \frac{d\sigma_{AA}^{h_1 h_2}/dp_T^{trig} dp_T^{assoc}}{d\sigma_{pp}^{h_1 h_2}/dp_T^{trig}}, \tag{2.5}$$

where $z_T = p_T^{assoc}/p_T^{trig}$.

We start in Chapter 3 with a description of the experimental facilities used to acquire the data, then we present in Chapter 4 the techniques used in analyzing the data, after which we present the results in Chapter 5. We end with conclusions and suggestions about further directions in Chapter 6.

Chapter 3

Experimental Facilities

3.1 Introduction

The experiments for this thesis were performed at the Relativistic Heavy Ion Collider (RHIC) operating at the Brookhaven National Laboratory (BNL). RHIC was designed to study relativistic heavy ion collisions and search for a new form of nuclear matter at high energy density (Quark Gluon Plasma). RHIC was also designed to collide polarized protons for a spin physics program and is presently by far the highest energy polarized proton collider. It started operations in the year 2000 with Au+Au collisions at $\sqrt{s_{\rm NN}}$= 130 GeV. Four dedicated detectors are taking advantage of the data produced at RHIC - STAR, PHENIX, PHOBOS, and BRAHMS. So far they have produced an impressive collection of experimental results in various collision systems (p+p, d+Au, Cu+Cu and Au+Au) at several different energies ranging from 9 to 200 GeV per nucleon for heavy ions, and 200 to 400 GeV for protons. In this chapter we describe the RHIC experimental facility and the STAR detector, which was used to collect the data presented in this thesis.

3.2 RHIC

RHIC is a unique collider, capable of accelerating and colliding a variety of ion species at different energies, whereas most accelerators usually operate only at a

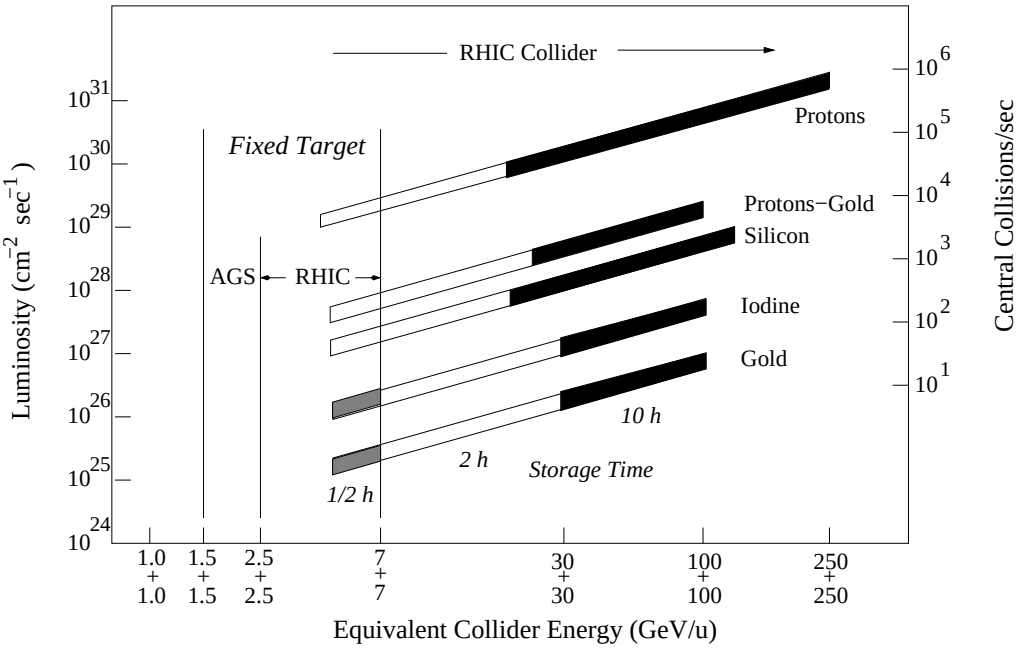

Figure 3.1: Design specifications for RHIC

.

maximum energy. The particle species that can be accelerated range from protons (A=1) to Au (A=197). The two independent rings and two separate sources of ions (two Van de Graafs or a Van de Graaf and a proton linac) allow for collisions with unequal ion species such as proton on gold, or light nuclei on gold. The top collision energy is $\sqrt{s_{\rm NN}}$= 200 GeV for heavy ions and $\sqrt{s}$ = 500 GeV for protons. The design luminosity is $L = 2\times10^{26} cm^{-2}s^{-1}$ for Au+Au and $L = 1.4\times10^{31} cm^{-2}s^{-1}$ for p+p collisions. Design performance specifications for RHIC are illustrated in Fig. 3.1.

The RHIC accelerator complex includes two Tandem Van de Graaffs that can operate exclusively or in parallel, a proton linear accelerator (LINAC), the Booster synchrotron, the Alternating Gradient Synchrotron (AGS), and ultimately the RHIC synchrotron rings. The RHIC collider consists of two 3.8 km quasi-circular concentric accelerator/storage rings in the same horizontal plane, one (”Blue ring”) for clockwise beams, and another (”Yellow ring”) for counter-clockwise beams. Bending and focusing of the ion beam is done by the two rings of superconducting

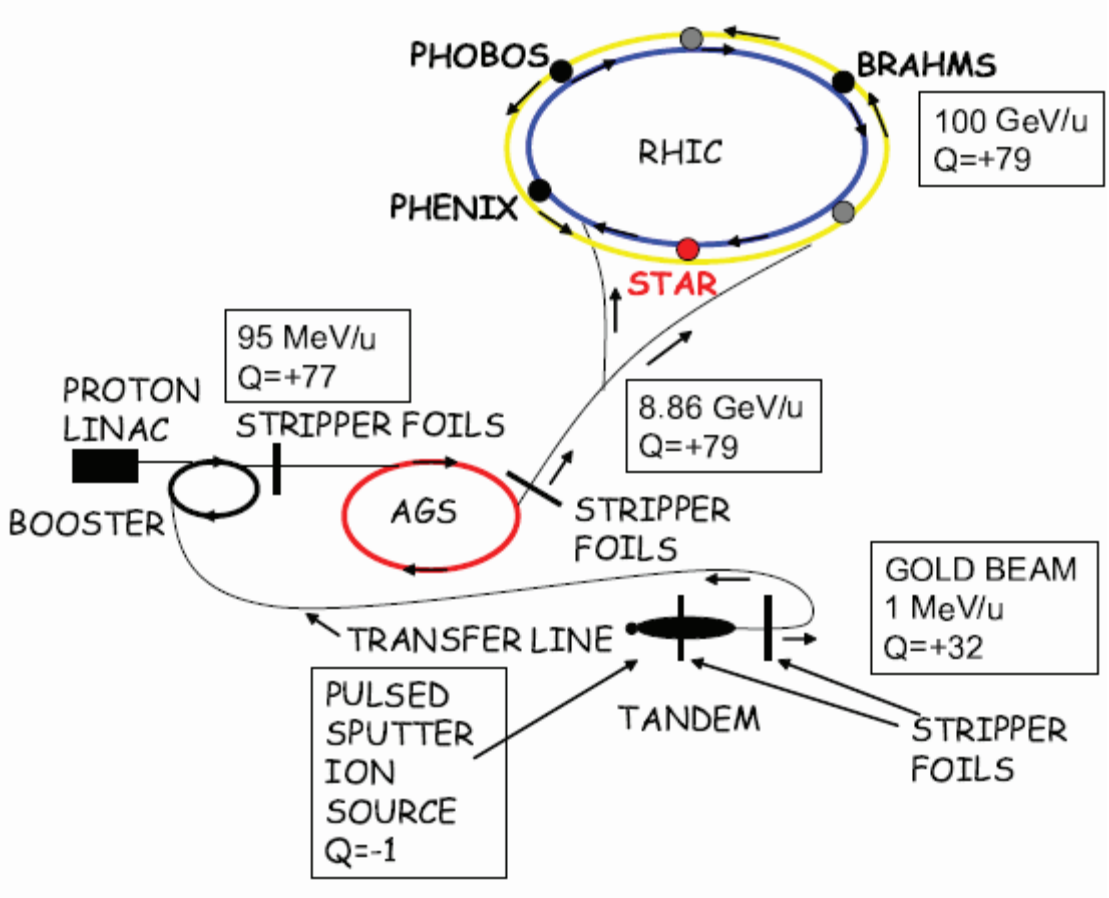

Figure 3.2: View of the RHIC accelerator complex at BNL from above. The RHIC rings are 3.8 km in circumference. See text for details.

magnets, cryogenically cooled to $< 4.7°$ K that yield a nominal magnetic field value of $\approx$3.8 T at the top of the ramp[1]. Each ring consists of six arc sections and six interaction points, allowing for simultaneous collisions at six locations. A pair of dipoles, DX and D0, located at ~10m and ~23m from each collision point, steer the beams into collision.

The acceleration scenario for Au+Au collisions at RHIC is illustrated in Fig. 3.2. Negative Au ions with charge Q=-1 are extracted from the Pulsed Sputter Ion Source. They are then accelerated through the Tandem Van de Graaff to an

[1]The ramping of a magnet involves applying an increasingly large current to reach the nominal value of magnetic field.

energy of 1 MeV/nucleon and are stripped of some of their electrons by passing through a series of stripping foils. The Au ions with net charge Q = +32 are then delivered to the Booster synchrotron via a 850m transfer line. After being accelerated to 95 MeV/nucleon in the Booster and further stripped to Q = +77, the ions are transferred to the AGS. There they are accelerated to the RHIC injection energy of 10.8 GeV/nucleon and sorted into four final bunches. The bunches are ejected from the AGS, one at a time, stripped to the final charge state of Q = +79 and transferred to RHIC. The final stage of acceleration to the top energy of 100 GeV/nucleon in the RHIC rings takes approximatively 2 minutes and it is achieved using the 28 MHz acceleration RF system. The bunches are then stored in the two rings (”yellow” and ”blue”) using the 197 MHz storage RF system. For p+p operations, protons are injected from the 200 MeV Linac directly into the Booster synchrotron, followed by acceleration in the AGS and injection into RHIC.

3.3 STAR

The Solenoidal Tracker at RHIC (STAR) is one of the two large detectors taking data at RHIC (the other is PHENIX). STAR was designed to work in a high multiplicity environment (1000 charged particles per unit pseudo-rapidity) and provide hadron detection over a large solid angle. It is an azimuthally symmetric detector that has excellent tracking, momentum determination, and particle identification capabilities for hadrons over the full azimuth ($\Delta\phi = 2\pi$). Electromagnetic calorimeters are used to measure high transverse momentum photons and electrons. The layout of the STAR detector is shown in Fig. 3.3.

The main component of STAR is a large cylindrical Time Projection Chamber (TPC) with inner radius of 50 cm and outer radius of 2 m. It is 4.2 m long and covers the pseudo-rapidity range $|\eta| \leq 1.8$. It has excellent tracking and particle identification capabilities. Two other tracking detectors are located between the beam pipe and the TPC. They are used for charge particle tracking close to the interaction region, and for improving the primary and secondary vertex resolution. These are the Silicon Vertex Tracker (SVT) and the Silicon Strip Detector (SSD).

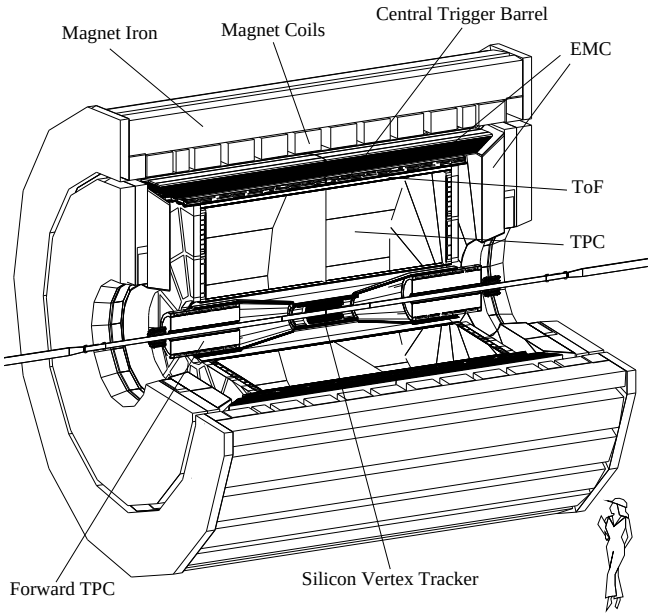

Figure 3.3: STAR layout with a cutaway for showing the inner detectors

The SVT consists of three concentric cylindrical barrels of silicon drift detectors located at 7, 11 and 15 cm from the beam axis. The SSD, located at 23 cm from the beam axis, acts as the fourth layer of the inner tracking system, which covers the pseudo-rapidity range $|\eta| \leq 1$. Both the TPC and the silicon detectors have azimuthal symmetry and full azimuthal coverage ($\Delta\phi = 2\pi$). Two radial drift TPCs (FTPC) extend the tracking and particle identification to forward pseudo-rapidity ($2.5 < |\eta| < 4$); they have the same azimuthal symmetry and coverage as the aforementioned tracking detectors. A barrel electromagnetic calorimeters (BEMC) and an end-cap electromagnetic calorimeter (EEMC) are used to measure the transverse energy deposited by electrons and photons. The detectors mentioned are encompassed by a room temperature magnet that provides a 0.5T uniform solenoidal magnetic field. The BEMC and EEMC are also used for triggering on events with high transverse energy or rare processes. STAR also has several trigger detectors used for triggering and centrality determination: two Zero Degree Calorimeters (ZDCs), two Beam Beam Counters (BBCs) and a Central Trigger Barrel (CTB). The ZDCs are located 18 m from the nominal interaction point on each side

and measure the energy deposited by the non-interacting neutral particles that propagate along the beam direction. The CTB is composed of scintillator tiles surrounding the outer cylinder of the TPC at $|\eta| < 1$ and measures the charged particle flux in the mid-rapidity region. The BBCs are situated at each end-cap of the TPC at 3.5 m from the interaction point. Each BBC consists of hexagonal scintillating tiles arranged in concentric circles forming a disk. The following sections will present in more detail the STAR magnet, the trigger detectors and the TPC, which is the detector used in the present analysis.

3.4 STAR magnet

The STAR magnet is an essential part of the detector, as it provides the magnetic field used for determining the momentum of charged particles. The characteristics of the magnet were chosen to allow good momentum resolution at high transverse momentum (p_T) and tracking at low momenta (500 MeV), which led to the choice of a 0.5 T field. A very homogeneous field is needed in order to minimize the electron drift distortions that would negatively impact the momentum resolution, especially at high-p_T (the resolution depends on the accuracy in determining the curvature of the tracks). A room temperature technology was chosen because of cost considerations.

The magnet is approximately cylindrical and surrounds the TPC and the other tracking detectors. It is 6.85 m in length, has an inner diameter of 5.27 m and an outer diameter of 7.32 m [26]. A sideview quarter-section of the magnet is shown in Fig. 3.4. The magnet has main coils that produce the solenoidal magnetic field, and trim coils, that help reduce distortions. When the magnetic field is at the maximum value of 0.5 T, the current in the main and trim coils has a value of 4500A. A water cooling system dissipates approximately 3.5 MW of power in order to maintain a temperature of 29° C. The steel of the magnet serves as a return path for the field flux and consists of 30 flux return bars (backlegs), four end-rings and two poletips, with a total weight of 1100 tons.

The magnet is used either at the nominal value of the field (0.5 T) or at half-field

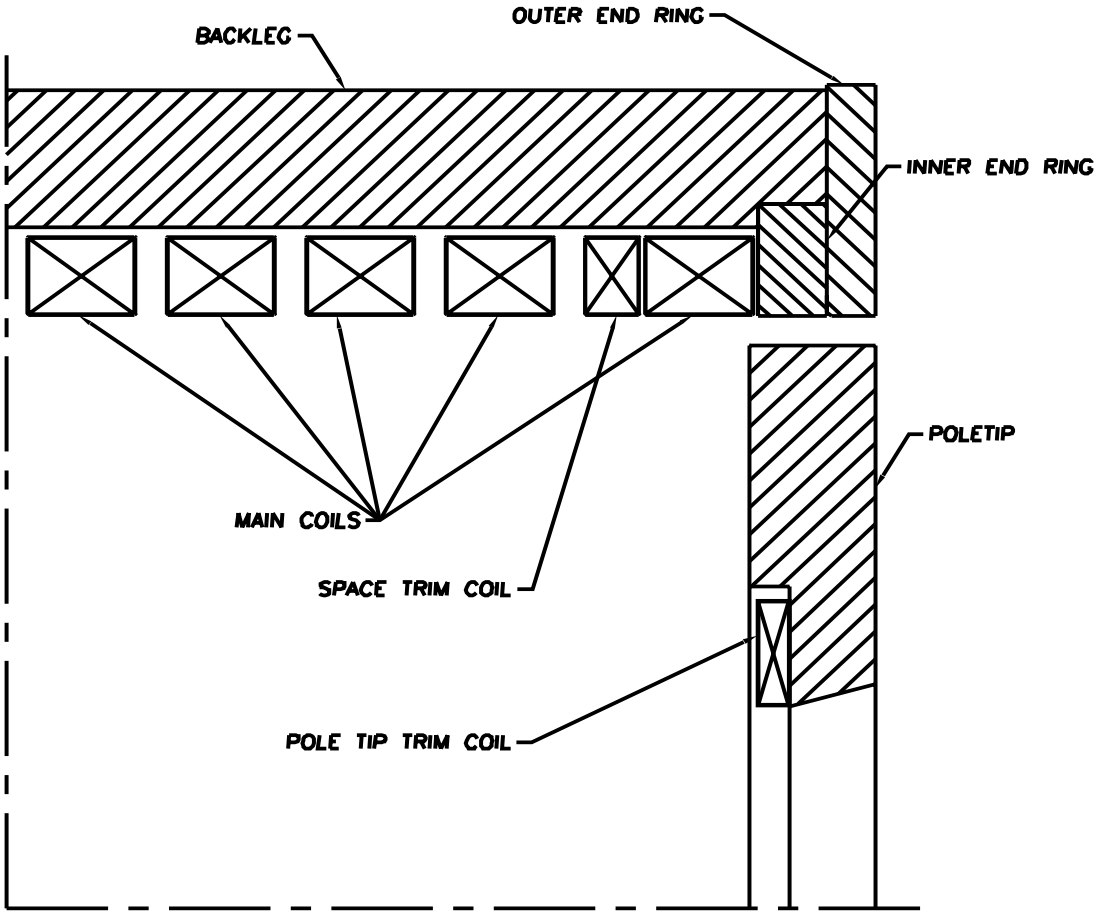

Figure 3.4: STAR magnet cross-section [26].

(0.25 T). At the nominal value the field is used for both polarities (referred to as "full-field" and "reverse full-field"). The magnetic field components, B_z, B_r and B_ϕ were mapped using a steerable array of Hall probes. The reproducibility of the field is better than ±0.5 Gauss. The radial component of the field (B_r) at $\phi = 0$ [2]as a function of axial distance (z) is presented in Fig. 3.5a for three different radii. As can be seen, the value of the radial component is ±50 Gauss. The maximum value of the ϕ field component is ±3 Gauss. These values are a factor 2 better than the design specifications. The corresponding field integrals, $\mathfrak{I}_r$ and $\mathfrak{I}_\phi$[3], have absolute

[2] ϕ is measured in the STAR lab coordinate system with the x-axis on the horizontal, the y-axis is vertical, and the z-axis is along the beam-line

[3] $|\mathfrak{I}_r| = |\int \frac{B_r}{B_z} dz|$, $|\mathfrak{I}_\phi| = |\int \frac{B_\phi}{B_z} dz|$

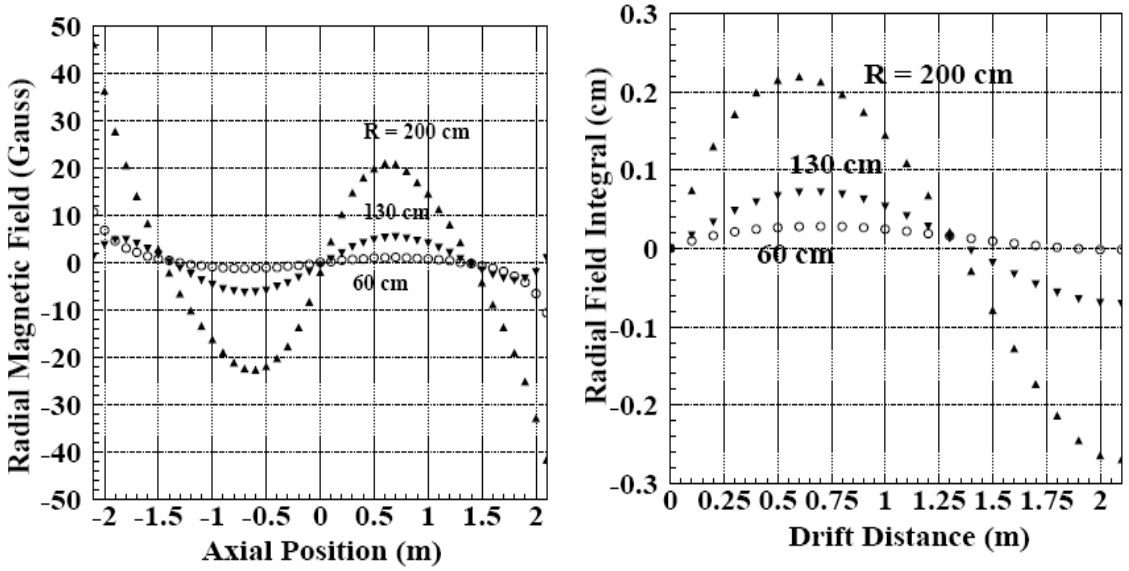

Figure 3.5: (a) STAR radial magnetic field component at $\phi = 0$ for three radii. The values are plotted versus the axial distance (z) with respect to the center of the magnet and of the TPC. The outer radius of the TPC is 200 cm. (b) Corresponding radial field integral as a function of drift distance [26].

values smaller than 0.30 cm and 0.035 cm, respectively. The radial field integral is shown in Fig. 3.5b.

3.5 Trigger detectors

The process of making the online decision of what data to read out from the detector and write to tape is called triggering. At the most basic level, one wants to record all events in which a collision has occurred - the trigger scheme in this case is called ”minimum bias” trigger. One may also need to select only events with a specific topology, or containing highly energetic particles above a certain threshold, etc. The detectors used for triggering in the data presented in this thesis are the Zero Degree Calorimeter (ZDC) and the Central Trigger Barrel.

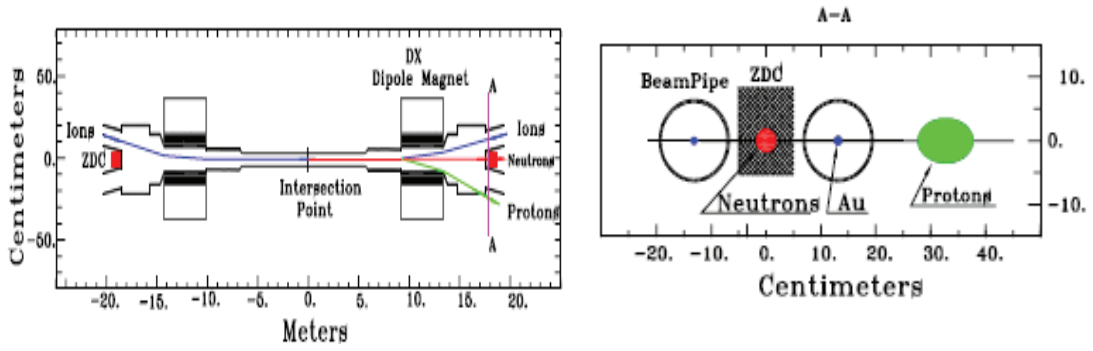

Figure 3.6: (a)Plan view of the collision region, (b)Beam-eye view of the ZDC location showing the location of the deflected protons [27].

3.5.1 Zero Degree Calorimeters

Each of the four experiments at RHIC is equipped with 2 Zero Degree Calorimeters used as minimum bias triggers in the heavy ion runs. They are located along the beam direction at 18 m on each side of the nominal interaction point and subtend 2.5 mrad. Their position can be seen in the view of the collision region in Fig. 3.6a. When an inelastic heavy ion collision occurs, remnant neutrons from the colliding nuclei propagate along the beam direction at very small angles. The ZDCs are hadron calorimeters designed to detect the beam remnant neutrons. Since the DX magnets are located between the interaction point and the ZDCs, the beams are bent back into their orbits and charged fragments are swept away, such that only the neutral beam remnants reach the ZDCs. This can be seen in Fig. 3.6b, which presents a cartoon of a beam's eye view of the ZDC.

The ZDCs consist of layers of tungsten absorbers and optical fibers for sampling. The neutrons hitting the ZDC produce particle showers in the layers of tungsten. The light generated by the resulted particles is transmitted through the optical fibers and collected by three PMTs (Photo Multiplier Tubes), whose summed analog output determine the ZDC signal. The minimum bias trigger used by STAR in Au+Au collisions requires a coincidence of the two ZDCs, with each ZDC signal required to be higher than 40% of a single neutron signal.

3.5.2 Central Trigger Barrel

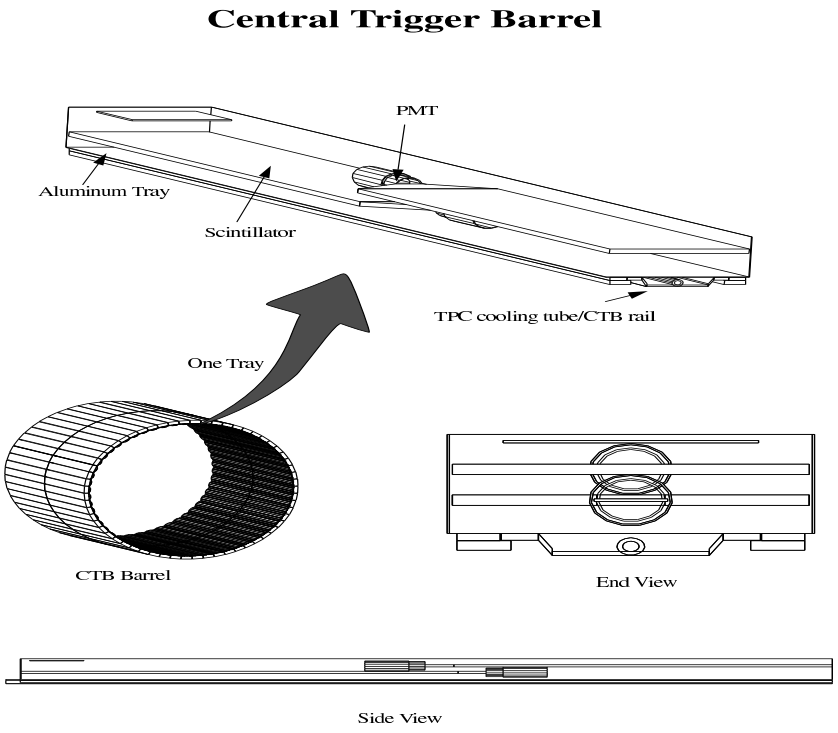

Figure 3.7: CTB cylinder and detail of one of its trays [28]. Each aluminum tray houses 2 CTB slats end to end. Each slat covers 1/2 unit in pseudorapidity and consists of a radiator, light guide, and mesh dynode photomultiplier tube.

The Central Trigger Barrel [28] is a barrel of scintillating tiles that measures charged particle multiplicity at mid-rapidity and allows for real-time event selection based on its information. It consists of 240 plastic scintillator slats of 4 m length arranged in a cylindrical fashion around the exterior of the TPC (see Fig. 3.7). It covers an azimuthal and pseudo-rapidity range $0 < \phi < 2\pi$ and $-1 < \eta < 1$, respectively. As a charged particle passes through a CTB tile, scintillation light is produced; it is then collected and transformed into an electrical signal by a PMT and then digitized through Analog to Digital Converters. The signal is summed over all the slats and its value is proportional to the number of charged particles

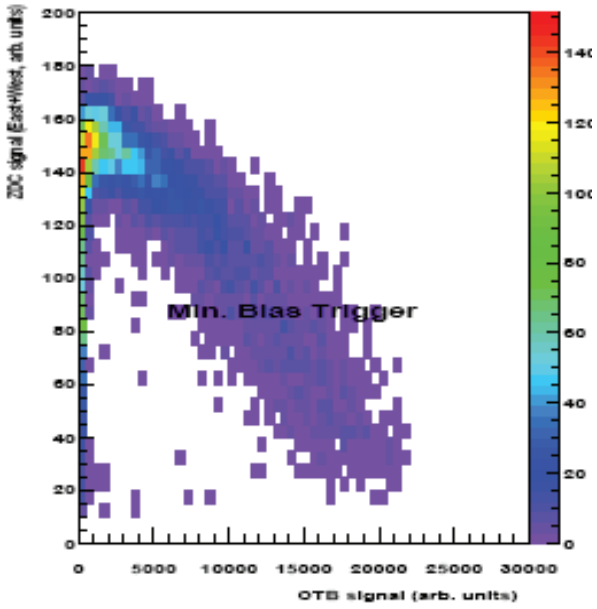

Figure 3.8: ZDC vs CTB signal strength correlation.

that crossed the CTB. Since it is a fast detector, the CTB, used in conjunction with the ZDC, is a powerful charged particle multiplicity trigger.

Fig. 3.8 shows the correlation between the ZDC summed signal and that of the CTB for minimum bias events. The largest number of events have large ZDC signal values and small CTB values. Simulations show that these are peripheral collisions, with a large impact parameter and small overlapping regions, which typically leave a large amount of energy in the forward region (large number of non-participating nucleons) and have a small charged particle multiplicity at mid-rapidity, therefore they leave a small amount of energy in the CTB. Collisions with progressively smaller impact parameter occur less frequently and give rise to higher charged particle multiplicity at mid-rapidity (and therefore higher CTB signal), but they have fewer non-participating neutrons, and therefore lower ZDC pulse hight. The observed correlation can be used to trigger on centrality. The ZDC is double-valued since collisions at either small or very large impact parameter can result in a small amount of energy in the forward ZDC direction.

3.6 TPC

The main detector used in this analysis is the TPC, which allows for charged particle tracking in a large transverse momentum range. The TPC was designed keeping in mind the requirements imposed by the unique environment of heavy ion collisions at RHIC. Key features of this environment are a large number of produced particles (up to approximately one thousand per unit pseudo-rapidity) and high momentum particles from hard parton-parton scattering. STAR was designed to measure many observables simultaneously in order to study signatures of a possible QGP phase transition and to understand the space-time evolution of the collision process in ultra-relativistic heavy ion collisions. In order to cover a large acceptance and have a large lever arm for improved momentum resolution at high p_T, the TPC is a large volume detector, 4.2 m in length, with an inner radius of 0.5 m and an outer radius of 2m (Fig. 3.9). The inner radius defines a pseudo-rapidity acceptance of $-2 \leq \eta \leq 2$, but the requirement that a particle passes a minimum number of rows (15-20, depending on the analysis) leads to a useful tracking range of $|\eta| \lesssim 1.5$. Its cylindrical shape allows for a full azimuthal coverage ($0 \leq \phi \leq 2\pi$) with azimuthal symmetry.

The TPC is divided at its center by a large diaphragm made of carbon-coated Kapton (the central membrane). The central membrane acts as a cathode, being kept at high voltage (28 kV). The end-caps are maintained at 0 V. A series of equipotential rings placed on the surface of the inner and outer field cages insure a highly uniform electric field, needed for uniform drift velocity, which is essential for good tracking and momentum resolution. The volume of the TPC is filled with P10, a gaseous mixture of 90% Argon and 10% Methane. P10 was chosen for its fast drift velocity (5.4 cm/μs), which is less sensitive to small pressure and temperature variations. The pressure in the TPC is maintained at 2 mbar above atmospheric pressure, in order to prevent outside air contamination due to leakeage into the gas volume of the TPC.

A charged particle crossing the TPC volume ionizes the P10 gas along its track. The secondary electrons drift in the electric field toward the closest end-cap, where

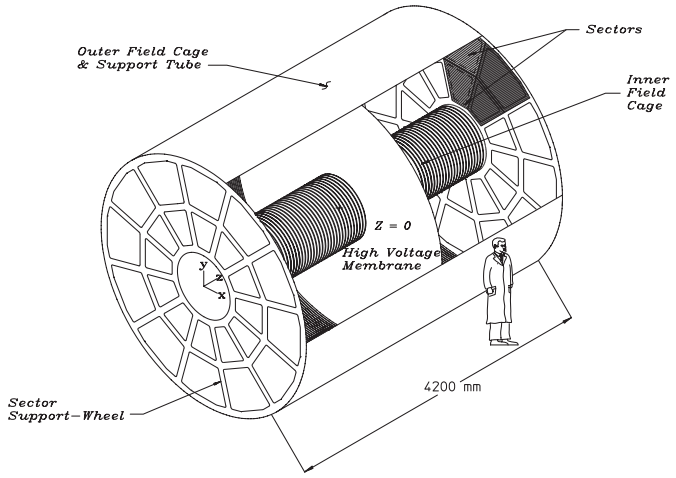

Figure 3.9: Schematic view of the STAR TPC [29].

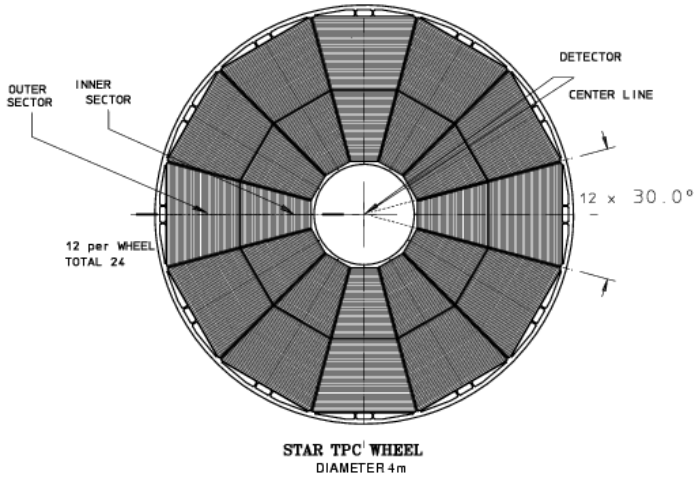

Figure 3.10: Beam's-eye view of a TPC end-cap, showing the sector layout

they produce a signal in the detector planes, consisting of the MWPC with pad readout. Each end-cap is divided into 12 radial sectors, each sector being divided into an inner and an outer sub-sector. A beam's-eye view of one of the end-caps is shown in Fig. 3.10.

A detailed view of a sector can be seen in Fig. 3.11. The inner sector consists of 1750 small pads (2.85 mm $\times$ 11.5 mm) arranged in 13 rows, whereas the outer sector consists of 3940 larger pads (6.2 mm $\times$ 19.5 mm) arranged in 32 rows. The inner

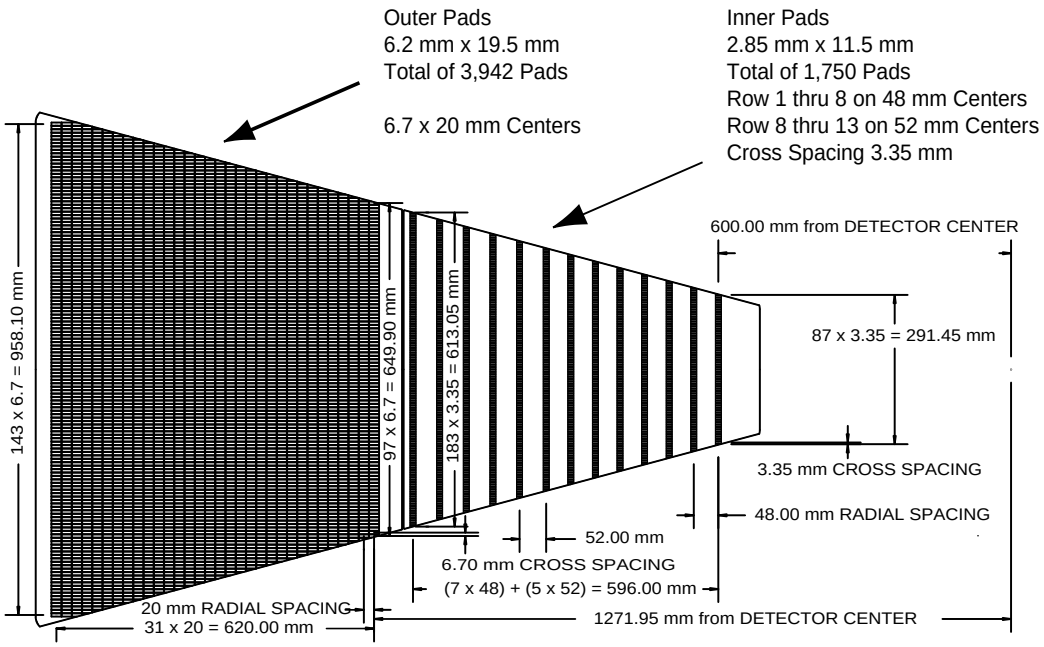

Figure 3.11: Detailed view of a single sector of the TPC, showing the inner and outer sectors, and their pad rows [29].

sector pads are smaller in order to cope with the high track density at smaller radii. The available packing density of the front end electronics channels constrain the number of pads, therefore the inner pads are more widely spaced (larger distance between rows). The larger pads in the outer sector maximize the amount of charge collected, and are closely spaced to optimize the dE/dx resolution.

Figure 3.12 shows the layout of the wire planes that together with the pads constitute the MWPC. The relative positions of the three wire grids - the gating grid, the ground plane and the anode layer - are shown for the inner and outer sector, respectively. The electrons released by ionization, when a charged particle passes through the TPC, drift toward the end-cap in the uniform electric field. The gating grid controls the entry of the electrons into the MWPC volume. The electrons are collected on the gating grid when it is closed, and they are allowed to pass in the amplification region when it is open, for events that meet the triggering conditions. The grid is open when all of the wires are biased to the same potential (typically 110 V). The grid is closed when the voltages alternate ± 75 V from the

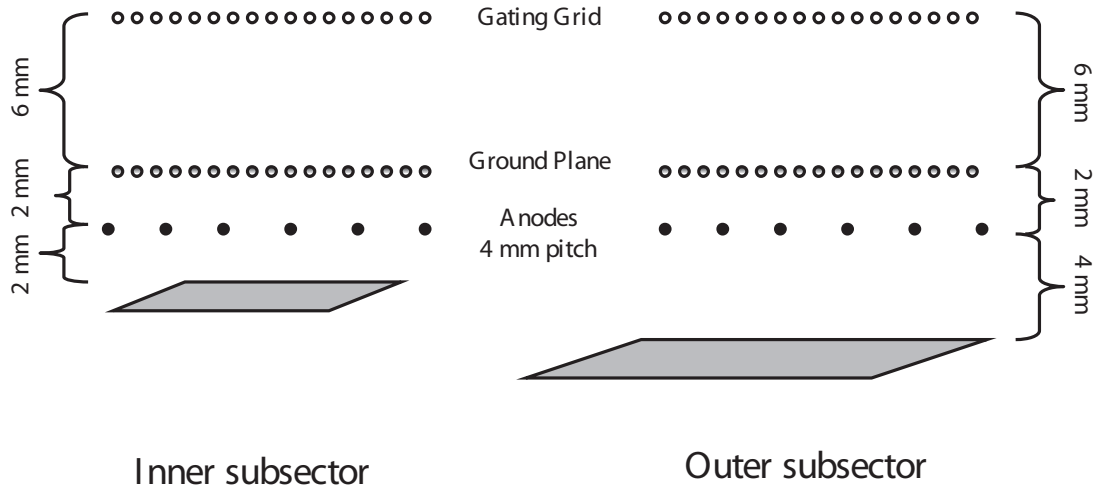

Figure 3.12: The readout chamber region of the TPC. The pitch of the gating and ground grids is 1 mm, while the anode wires are spaced 4 mm from each other [30].

nominal value. The positive ions are too slow to escape during the open period and get captured during the closed period. The gating grid driver has been designed to open and settle rapidly (100 V in 200 ns).

The ground plane defines the boundary of the active MWPC volume. The anodes are kept at high voltage (1170 V for the inner sector and 1390 V for the outer sector) and are placed immediately before the pad planes. The electrons passing through the gating grid and the ground plane initiate avalanches in the high field next to the anode wires. The ions created in the process induce a signal on the readout planes. The gas gain, controlled by the anode wire voltage, has been set independently for the two sector types to maintain a 20:1 signal to noise for pads intercepting the center of tracks that have drifted the full 2 meters. The effective gas gain needed to achieve this signal to noise is 3,770 for the inner sector and 1,230 for the outer sector.

During their drift, the electrons diffuse in both the transverse and longitudinal direction, setting limits on the x,y and z resolution. The z coordinate is determined by measuring the arrival time of the drifting electrons and dividing by the average drift velocity, which is measured using laser tracks of known position. Fig. 3.13

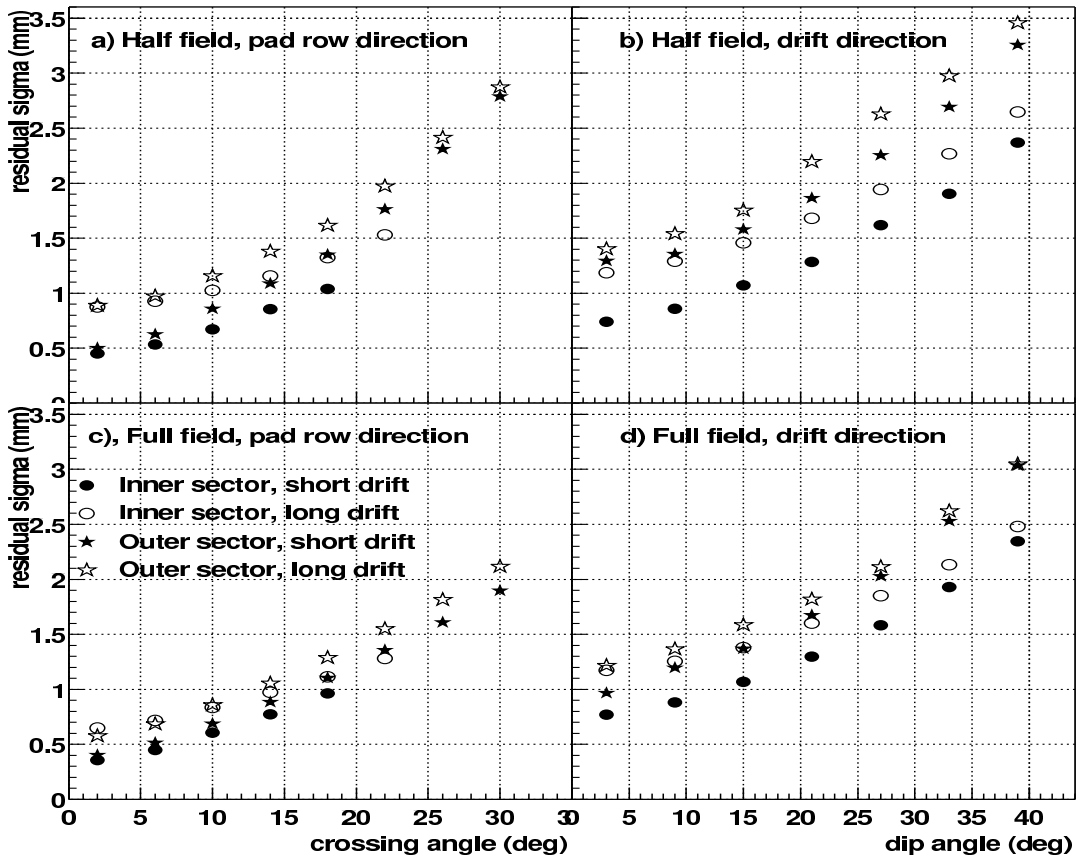

Figure 3.13: Position resolution in the pad row direction (a,c) and in the beam direction (b,d). The residual sigma is determined by fitting a Gaussian to the residual [4] distribution. The crossing angle is the angle between the particle momentum (defined as the tangent to the track) and the pad row direction. The dip angle is the angle between the particle momentum and the drift direction, $\theta = cos^{-1}(p_z/p)$ [29].

shows the position resolution for both full- and half-field configurations. For a track perpendicular to the pad row direction, a resolution of 400 μm and 750 μm is achieved in the transverse and longitudinal direction, respectively.

Chapter 4

Data Analysis

4.1 Data selection

The data used for this analysis consists of three different data sets - d+Au, Cu+Cu and Au+Au collisions at $\sqrt{s_{NN}}$=200 GeV - recorded in the 2003, 2004 and 2005 runs, respectively. In order to select the data satisfying the necessary quality criteria, both online and offline data selection is performed. Triggering uses information from the fast detectors to decide whether to record an event or not. Triggering is an efficient way of using the running time. Given the slow response of the TPC (rates of ~100 Hz) and the bandwidth limitations of the data acquisition system, it is only possible to record a small fraction of the collisions (which have rates of 10 MHz at high luminosity). Triggering allows us to record the ones we are interested in analyzing. At any given time during a run, multiple triggering configurations are used with different bandwidths to record various samples of interest for various analyses. It is possible for an event to satisfy the criteria for different triggers and so an event can be labeled as belonging to multiple trigger classes. In this analysis we used the minimum bias triggered data sets for all of the three collision systems, as well as the central triggered Au+Au data set.

The minimum bias trigger allows the sampling of the entire hadronic cross section and is implemented by requiring coincidences between the two zero degree

calorimeters (ZDCs), with each ZDC having a summed analog output corresponding to at least 40% of a single neutron energy. The central triggered Au+Au data set uses a CTB (Central Trigger Barrel) threshold to select events with high multiplicity, which are central events. Offline simulations show that the central trigger selects events with a reference multiplicity corresponding to the 12% most central events. A preliminary vertex cut is implemented online using the Time to Amplitude Converter (TAC) signals from the ZDCs.

In the offline analysis, the events are selected so that they satisfy certain criteria: they belong to the trigger configuration desired, the tracking software has identified a proper primary vertex. The primary vertex is found by considering all tracks reconstructed in the TPC and then extrapolating them back to the origin. When the multiplicity of an event is low, accurate identification of the primary interaction vertex in that event is not feasible, and the event cannot be used. This is the reason why we only use events with centrality 0-80% for Au+Au and 0-60% for Cu+Cu collisions. Another requirement we impose is that the primary vertex is within ±30 cm from the nominal vertex position along the beam axis. This cut is aimed at reducing biases due to asymmetry in the detectors.

4.1.1 Tracking selection

In order to ensure that the tracks used in the analysis are correctly reconstructed by the tracking algorithm, we require that a track has been reconstructed using at least 15 hit points (corresponding to 15 TPC row pads) out of the maximum 45 possible. The tracks inadvertently lost by using this cut are corrected for by using the same cut in the simulations used to determine the track efficiency. In this analysis we are interested in particles produced in the collision (as opposed to their decay products). To insure that the particles selected satisfy this condition, and also eliminate stray tracks, we only select tracks with a distance of closest approach to the primary vertex $|DCA| \leq 1$ cm. An additional cut limiting the tracks' pseudorapidity range at $|\eta| < 1$ insures that the tracks fall within the pseudorapidity range of the outer TPC barrel. It ensures that there is sufficient path length in the TPC for the

possibility of good reconstruction of the track, allowing for a tracking efficiency that does not vary dramatically with η.

4.2 Tracking efficiency

The efficiency of reconstructing a particle passing through the detector needs to be studied and corrected for when determining absolute yields. This involves a full characterization of the detector efficiency and acceptance as a function of momentum, azimuth and pseudorapidity. The limited acceptance of the detector leads to the loss of tracks which do not pass through the active volume of the detector. Additionally, the tracks that penetrate an active detector volume may still be incorrectly reconstructed due to various factors: dead channels in the detector, space-charge distortions, merging of tracks, fake tracks and algorithm inefficiencies. The effect of these inefficiencies needs to be corrected for in order to obtain the true produced particle yields.

The combined result of these effects is studied by simulating the detector response to Monte Carlo generated particles with a known kinematic distribution (the input) and then adding this simulated detector response to the detector response recorded from a real STAR event. The simulation of the detector response is done using the GEANT software [31], which contains a library that models electromagnetic and nuclear interactions of particles with matter. A detailed three dimensional model of all material present in the STAR interaction region is implemented in the GEANT code, which allows for the simulation of a particle's interaction with the material, its deposited energy and its resulting path. Software describing the TPC response to ionizing particles is used to simulate the propagation of the ionized charge (the GEANT output) through the TPC gas as well as details of the deposition of the charge on the pad planes and their response up to the point of producing digitized outputs (from Analog-to-Digital Converters - ADCs). These ADC values are added to the raw data of real events, and then track reconstruction is done using the full STAR data reconstruction software. Finally, an association algorithm is performed to associate reconstructed tracks with the input Monte Carlo tracks at

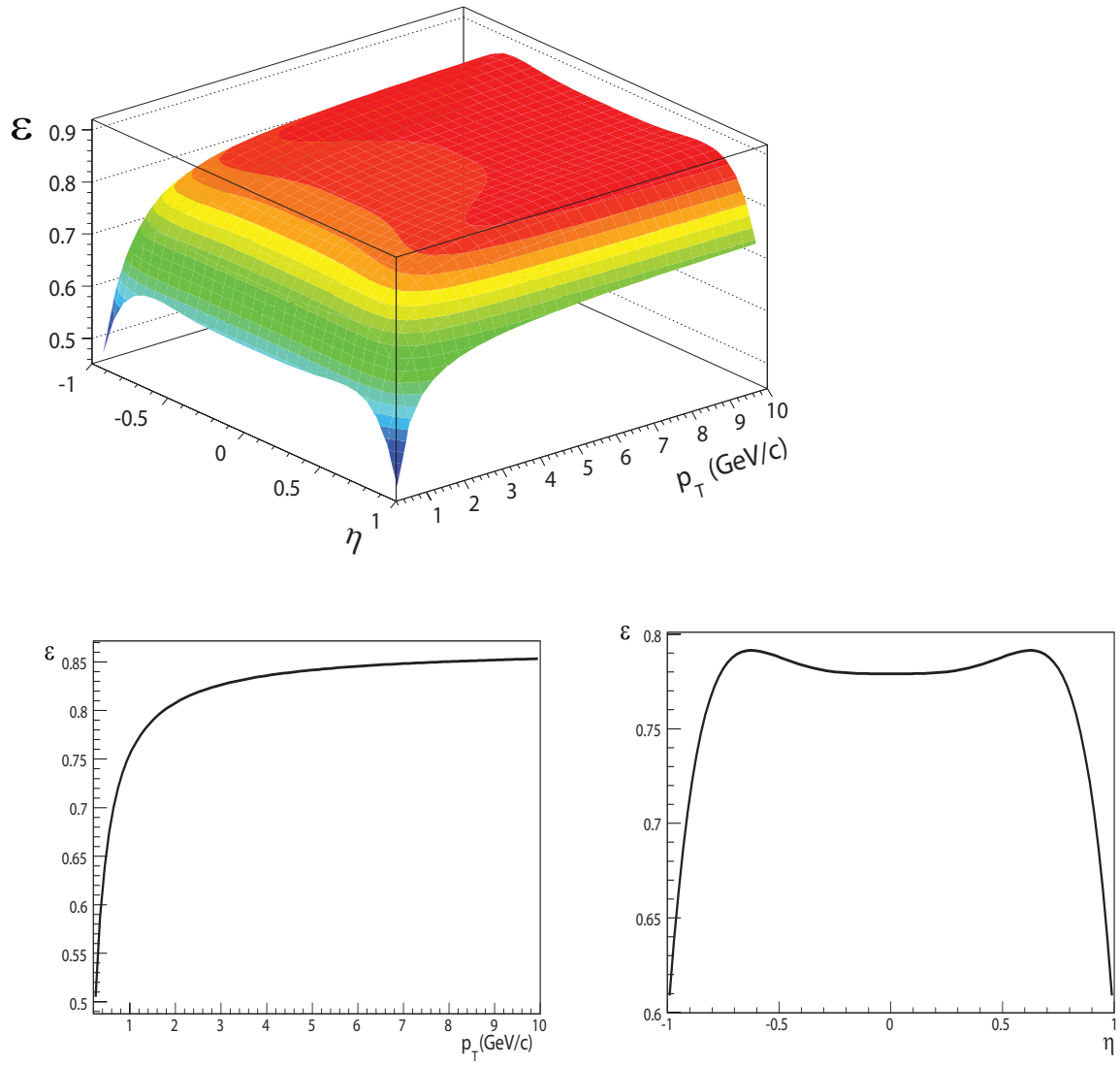

Figure 4.1: (a) Tracking efficiency as a function of transverse momentum and pseudorapidity. (b) η-integrated efficiency as a function of p_T. (c) p_T-integrated efficiency as a function of η. All three panels refer to central (0-10%) Cu+Cu collisions at $\sqrt{s_{NN}} = 200$ GeV.

hit level. The distance between the reconstructed hits and the input hits is used to determine if the input hit was reconstructed. If the Monte-Carlo track is associated with a minimum number of hits included in the reconstructed track fit, the Monte-Carlo track is associated with the reconstructed track. All quality cuts used in the

analysis of real data are imposed on these reconstructed tracks. Only those passing all analysis cuts are valid reconstructed tracks which can be used for determining the efficiency. The efficiency can be expressed as

$$\epsilon(p_T, \eta) = \frac{N^{reco}_{tracks}(p_T, \eta)}{N^{input}_{tracks}(p_T, \eta)} \tag{4.1}$$

where N^{input}_{tracks} is the number of input Monte-Carlo tracks and N^{reco}_{tracks} is the number of reconstructed tracks. The efficiency is calculated for each centrality class used in the analysis. In order to apply the necessary corrections as a function of p_T and pseudorapidity, we parametrize the efficiency using the following function:

$$\epsilon(p_T, \eta) = C_0\eta + C_1\eta^2 + C_2\eta^4 + C_3\eta^6 + C_4\eta^8 + C_5 e^{-(C_6/p_T)^{C_7}} \tag{4.2}$$

Fig. 4.1 shows an example of the efficiency distribution as a function of (p_T,η), as well as its projections, revealing its dependence on p_T and η, respectively.

4.3 Analysis procedure

Here we briefly describe the analysis procedure implemented in the software created for this analysis. The events that fulfill the data selection cuts are divided into centrality classes depending on their charged particle multiplicity. The multiplicities corresponding to each centrality class are determined by dividing the $d\sigma/dN_{ch}$ measured distribution into equally sized fractions of the total cross-section (0-10% central collisions meaning the most central 10% of the collisions etc.). The software then loops over all the tracks that pass the track quality cuts and selects particles within a predetermined p_T range - these are the so-called "trigger particles". The p_T ranges used in this work are $4 < p_T^{trig} < 6$ GeV/c and $6 < p_T^{trig} < 10$ GeV/c, in order to select particles predominantly formed in a fragmentation process. For each trigger particle another pass over all other tracks in the event is performed and particles with p_T in a predetermined (lower) range are identified. We refer to these particles as the "associated" particles, and a p_T range we used for many results is

$3 < p_T^{assoc} < p_T^{trig}$. The azimuthal and pseudorapidity separations between the associated and the trigger particle are calculated ($\Delta\phi = \phi^{trig} - \phi^{assoc}$, $\Delta\eta = \eta^{trig} - \eta^{assoc}$) and used to construct the two dimensional $\Delta\phi$-$\Delta\eta$ distributions. Each associated particle contributes a weight $1/\epsilon$ to the distribution, where $\epsilon(p_T, \eta)$ is the track efficiency. No track efficiency correction is applied for the trigger particles, since the results we are interested in will be normalized to the number of triggers.

4.3.1 Pair acceptance correction

While the weighting factor corrects for the single track efficiency, the limited detector acceptance leads to a convolution effect in the two-particle correlations. To understand this effect, let us consider first the (idealized) uniform single-particle distribution in the pseudorapidity coverage of the STAR detector:

$$f(\eta) = \begin{cases} a, & |\eta| < 1 \\ 0, & |\eta| \geq 1 \end{cases} \tag{4.3}$$

Both the trigger and the associated particles follow this η distribution. A Monte Carlo simulation of 1000 triggers and 10000 associated particles drawn from this distribution shows that the trigger-associated $\Delta\eta$ distribution has a triangular shape, as shown in 4.2b. The probability has been normalized such that the maximum has a probability of one, corresponding to the ideal case of no loss due to acceptance limitations. The probabilities less than one correspond to losses due to the limited acceptance and must be corrected for when determining the true correlation yields. The corrections are done using a "mixed event" technique that we will briefly present in the next section.

Acceptance issues also influence the $\Delta\phi$ distributions. The azimuthal distribution of both trigger- and associated-particles has 12 dips due to the gaps between the TPC sectors (see section 3.6). Fig. 4.3a shows a ϕ acceptance schematically reproducing the TPC acceptance. The dips in acceptance influence the two-particle acceptance depending on the position of the trigger and associated particles with respect to the TPC sector gaps. Fig. 4.3b shows the $\Delta\phi$ distribution of 1000 trigger

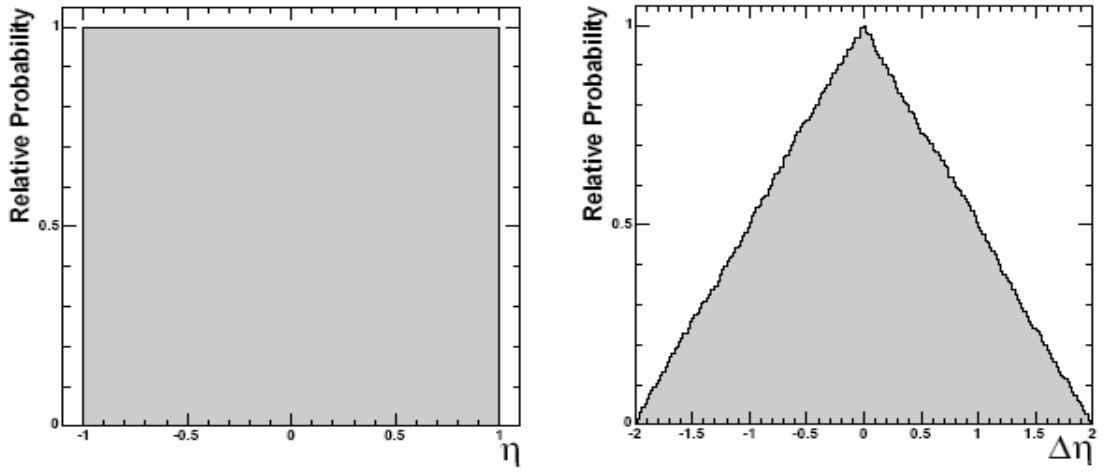

Figure 4.2: (a) Idealized TPC pseudorapidity acceptance. (b) Resulting pseudorapidity difference distribution, normalized to have a peak acceptance of 100% [32].

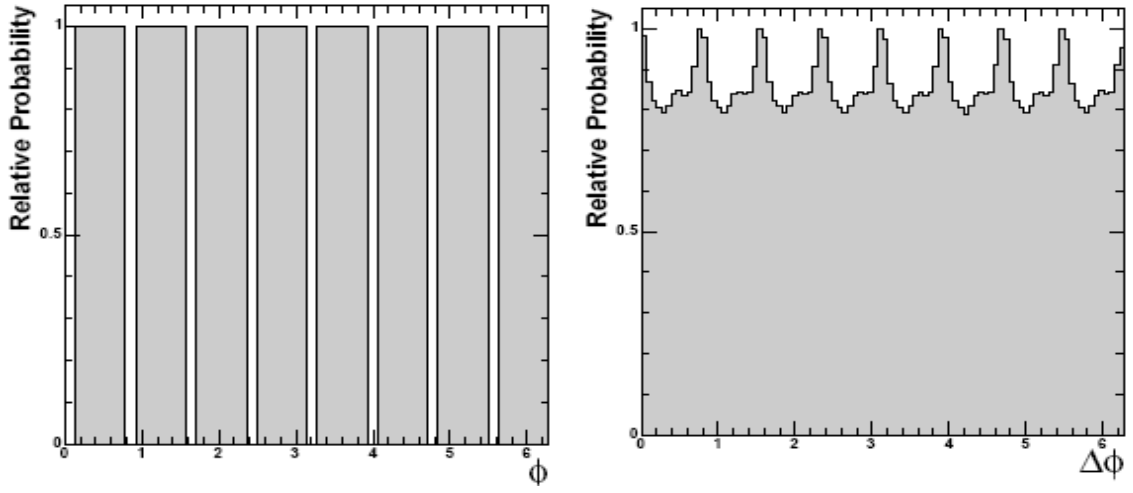

Figure 4.3: (a) Simplified TPC azimuthal acceptance. (b) Resulting $\Delta\phi$ distribution, normalized to have a peak acceptance of 100% [32].

and 10000 associated particles simulated according to the ϕ distribution in Fig. 4.3a.

4.3.2 Mixed events

In practice, the acceptance is p_T-dependent, and the η acceptance is also influenced by the primary vertex position along the beam line. In order to reproduce the pair acceptance in a realistic way, we construct "mixed events" by correlating the trigger in a certain event with the associated particles in a different event. The $\Delta\phi$-$\Delta\eta$ histograms of trigger-associated particles in mixed events will reflect the features of the limited pair acceptance, and will be used to correct for theses effects. The mixing is done with events from the same centrality class and with a similar z position of the primary vertex. For this purpose, the events are divided into 12 classes depending on their vertex position. 12 vertex bins of 5 cm length are defined from -30 cm to +30 cm along the beam axis. The pair acceptance corrections are applied separately for each vertex class.

Fig. 4.4 shows examples of a raw $\Delta\phi$-$\Delta\eta$ distribution (a), a mixed event distribution (b) and the resulting corrected distribution (c). The corrected bin content for each ($\Delta\phi$,$\Delta\eta$) bin is given by

$$n_{corrected}(\Delta\phi,\Delta\eta) = \frac{1}{n_{MixedEv}(\Delta\phi,\Delta\eta)} n_{raw}(\Delta\phi,\Delta\eta) \tag{4.4}$$

4.3.3 Extracting near-side yields

In order to extract the near-side jet-like correlated yield from the efficiency and acceptance corrected histograms, one has to subtract the various background components. Along with the uncorrelated pairs that generate a flat background, there are also correlated background components in the dihadron $\Delta\phi$ - $\Delta\eta$ distributions. As mentioned in section 2.2.1, the initial spatial anisotropy results in a momentum space anisotropy of produced particles. The cosine modulation of the azimuthal distribution of produced particles with respect to the reaction plane

$$\frac{d^3N}{p_T dp_T dy d\phi} = \frac{1}{2\pi} \frac{d^2N}{p_T dp_T dy} \Big[1 + 2v_2 \cos(2(\phi - \Psi_{RP}))\Big]. \tag{4.5}$$

leads to a cos(2$\Delta\phi$) modulation of the two particle azimuthal distributions:

$$Y(\Delta\phi, p_T) \approx B\Big[1 + 2v_2(p_T^{trig})v_2(p_T^{assoc})\cos(2\Delta\phi)\Big] \tag{4.6}$$

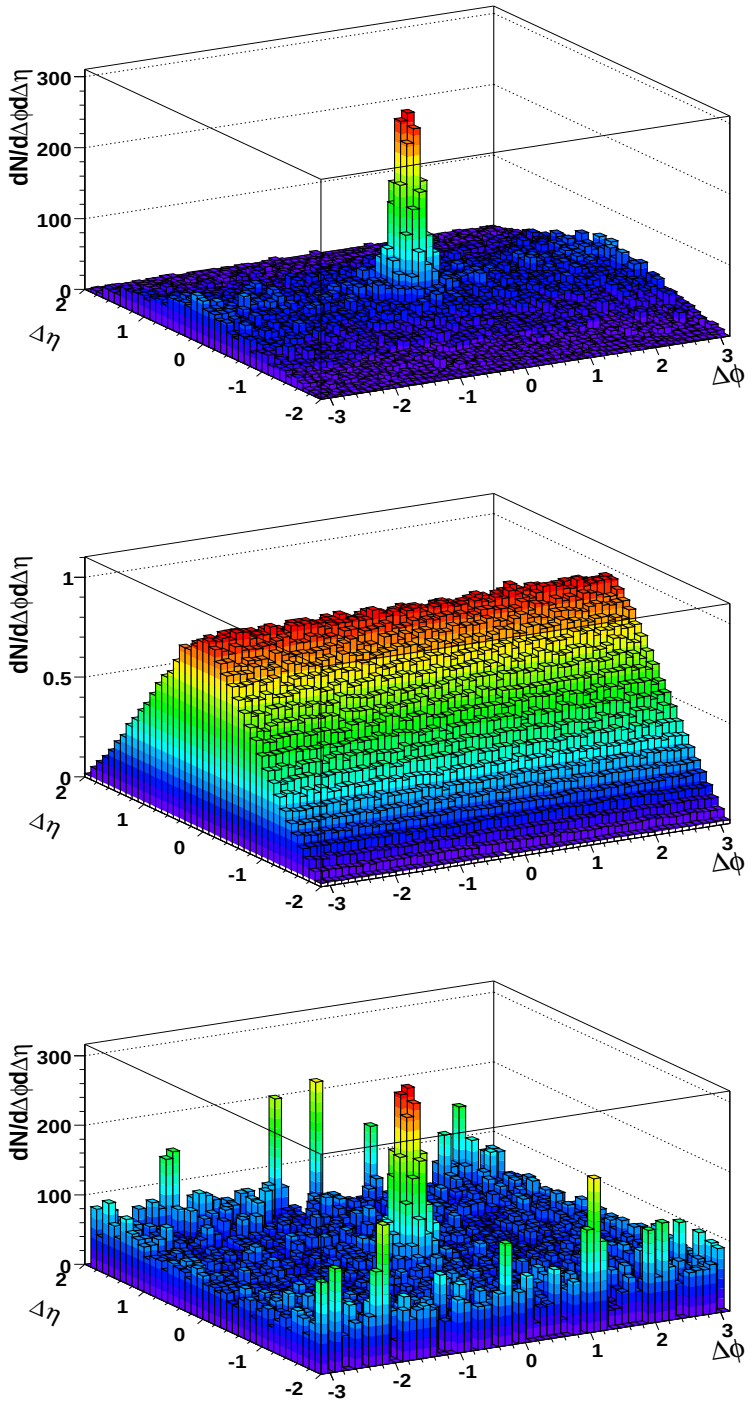

(c)

Figure 4.4: (a) Raw $\Delta\phi$-$\Delta\eta$ histogram for 0-10% Cu+Cu events, $4 < p_T^{trig} < 6$ GeV/c, $3 < p_T^{assoc} < p_T^{trig}$. Mixed events (b) and corrected (c) $\Delta\phi$-$\Delta\eta$ histogram for the same centrality class and p_T cuts. The corrected histogram has a reduced $\Delta\eta$ range $|\Delta\eta| < 1.7$, since the very large correction factors at the edge of the acceptance window lead to very large errors.

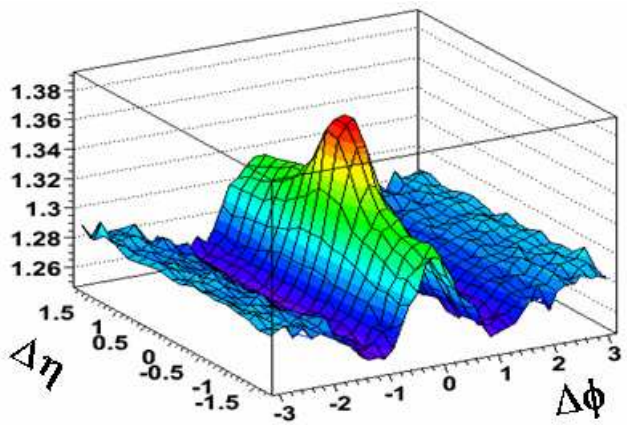

Figure 4.5: $\Delta\phi$ - $\Delta\eta$ dihadron distribution for Au+Au 0-12% central collisions, $3 < p_T^{trig} < 6$, $1.5 < p_T^{assoc} < p_T^{trig}$. The near-side ridge is evident above the v_2 - modulated background.

It has been shown [33] that the elliptic flow is independent of pseudorapidity in the STAR TPC acceptance, therefore the v_2 - modulated background of our dihadron correlations will be independent of $\Delta\eta$.

Studies from STAR [34] have shown the presence of long range psudorapidity correlations of particles close in azimuth ($\Delta\phi \sim 0$). These correlations form the so-called "ridge" in dihadron $\Delta\phi$ - $\Delta\eta$ distributions. The ridge is independent of $\Delta\eta$, as shown in Fig. 4.5.

To extract the near-side jet-like correlation yield, we need to subtract both the v_2-modulated background and the ridge contribution. As a consistency check, two methods have been used to remove the background and they are schematically shown in Fig. 4.6.

We first investigated the azimuthal profile of the distributions by projecting the two dimensional dihadron distributions onto $\Delta\phi$. We defined two $\Delta\eta$ ranges: region **1** in Fig. 4.6, with $|\Delta\eta| < 0.7$, and region **2**, with $0.7 < |\Delta\eta| < 1.7$. The near-side peak in region **1** includes the jet, the ridge and the v_2 - modulated background, whereas in region **2** it only includes the ridge and flow-modulated background, both being backgrounds for our analysis. Taking advantage of the independence of $\Delta\eta$ of both the v_2-modulated background and the ridge, we remove their contribution to the near-side peak by subtracting the (scaled) $\Delta\phi$ projection of region **2**

from the $\Delta\phi$ projection of region **1**. The region **2** $\Delta\phi$ projection is scaled to match the region **1** projection on the away-side. This allows for the near-side peak in region **2** to properly reproduce the ridge and flow background in region **1** and takes advantage of the fact that the away-side is flat over the entire $\Delta\eta$ range (due to the random distribution in η of the back-to-back jet). Fig. 4.7 shows the $\Delta\phi$ projections for the two regions (a), as well as the resulting background subtracted histogram (b) for Au+Au central collisions. Once the background subtracted histogram is obtained, the jet-like near-side yield is calculated by integrating over the range $|\Delta\phi| < 0.78$. The uncertainty on the resultant yield is given by the statistical errors on the data, as well as the normalization error on scaling the region **2** projection.

The other method to determine the near-side yield is by projecting the small $\Delta\phi$ region ($|\Delta\phi| < 0.78$) onto $\Delta\eta$. The ridge and the elliptic flow modulated background will constitute a flat background and the peak we can subtract is just the jet projection. Fig. 4.8 shows an example of $\Delta\eta$ projection (a) and the resulting background subtracted histogram. The yield is calculated by integrating over the region $|\Delta\eta| < 0.7$. As will be presented in the Results section, the yields obtained

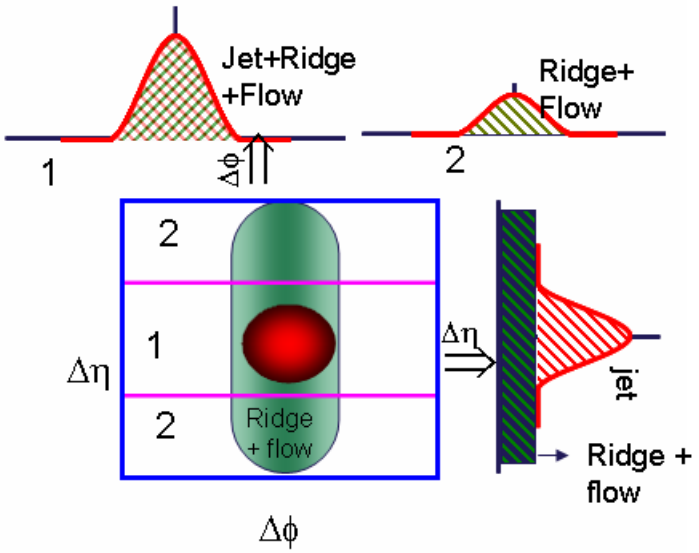

Figure 4.6: Sketch showing the two methods used for extracting the near-side yield from the $\Delta\phi$ - $\Delta\eta$ distributions. The background subtraction techniques are schematically indicated for the projection onto $\Delta\phi$ and $\Delta\eta$, respectively.

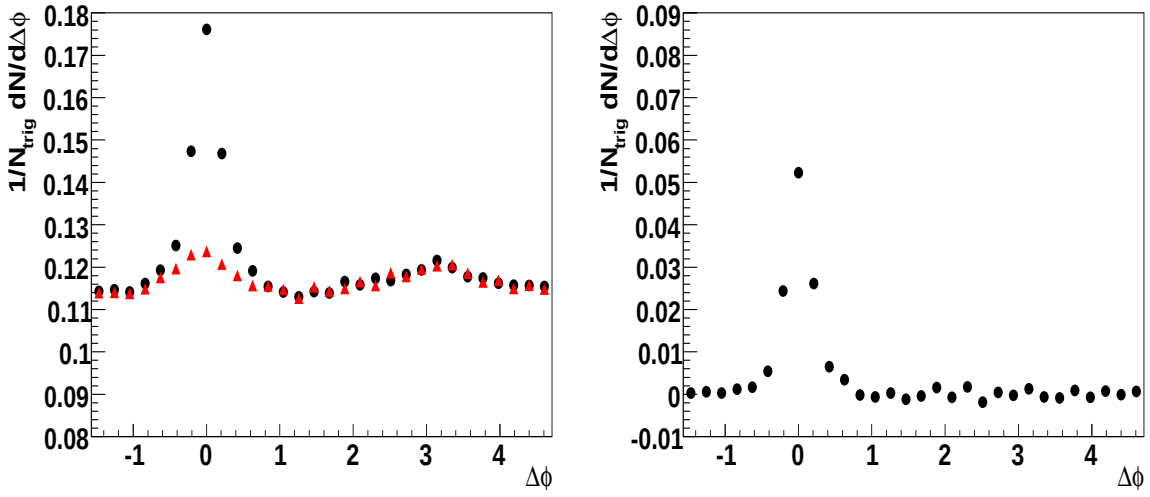

Figure 4.7: Di-hadron correlations in central (0-12%) Au+Au collisions: (a) $\Delta\phi$ correlations - large $\Delta\eta$ ($0.7 < |\Delta\eta| < 1.7$) (red triangles) and small $\Delta\eta$ ($|\Delta\eta| < 0.7$) (black circles), (b) $\Delta\phi$ subtracted distribution for $4 < p_T^{trig} < 6$ GeV/c, $p_T^{assoc} > 3$ GeV/c.

using the two methods are consistent with each other within errors.

4.3.4 Extracting away-side yields

The away-side jet-like yields we extract will be compared to theoretical calculations in order to constrain the present models. For reasons of consistency with both theoretical calculations and previous STAR results, we do not apply the pseudorapidity pair acceptance correction. The technique of extracting the away-side yields consists of projecting the entire two dimensional ($\Delta\phi$-$\Delta\eta$) dihadron distribution onto $\Delta\phi$. An example of such a projection is shown in Fig. 4.9. We need therefore to extract the away-side ($\Delta\phi \sim \pi$) peak of dihadron azimuthal correlations. As mentioned previously, the elliptic flow leads to a v_2-modulated background in azimuthal two particle correlations. The background level constant B from Eq. 4.6 is determined by assuming that there is no associated yield contribution at the minimum of the distribution - in this case at $1 < |\Delta\phi| < 1.5$ (the so-called "Zero Yield

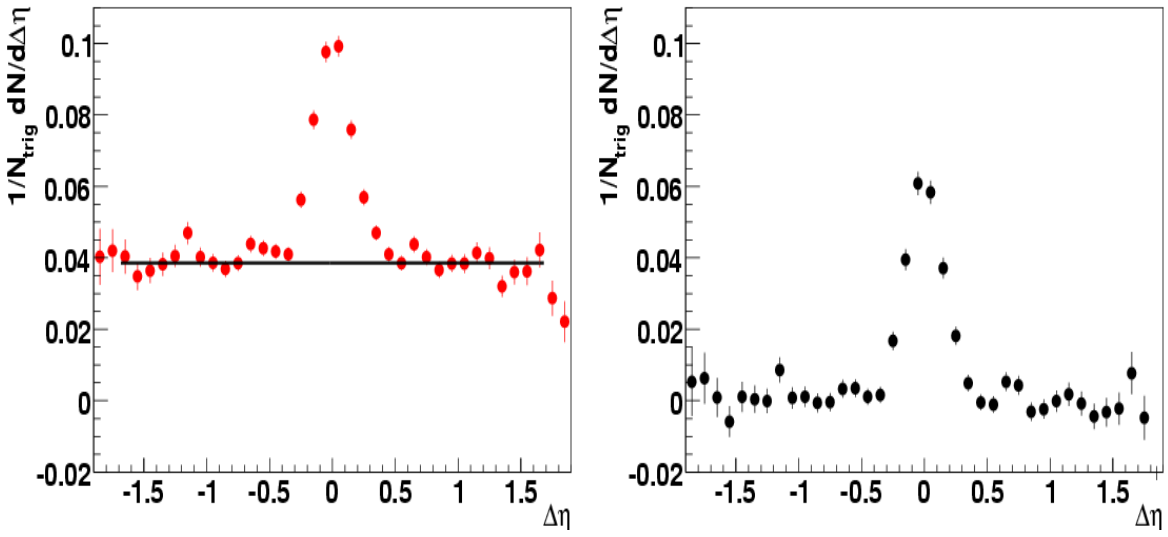

(a) (b)

Figure 4.8: (a) $\Delta\eta$ projections of di-hadron correlations in central (0-10%) Cu+Cu collisions, $4 < p_T^{trig} < 6$ GeV/c, $p_T^{assoc} > 3$ GeV/c. (b) Same as (a), after the background has been subtracted.

At Minimum" method). We used parameterizations of elliptic flow measurements of STAR [33, 35] to obtain the v_2 values ($v_2(p_T^{trig})$, $v_2(p_T^{assoc})$) necessary to describe the background. The away-side jet yield is measured by integrating the azimuthal distributions in the region $1.7 < \Delta\phi < 4.4$ and subtracting the background contribution in the same range.

The uncertainty on the v_2 measured values leads to a systematic error in the away-side yield determination. In order to estimate these errors, we compute the background curves for the upper (lower) bounds on the v_2 and use them to extract the bounds on the away-side yield. We use the results of two different methods of determining elliptic flow to calculate the best estimate of v_2 (taken as the average for most cases) and its upper and lower limits.

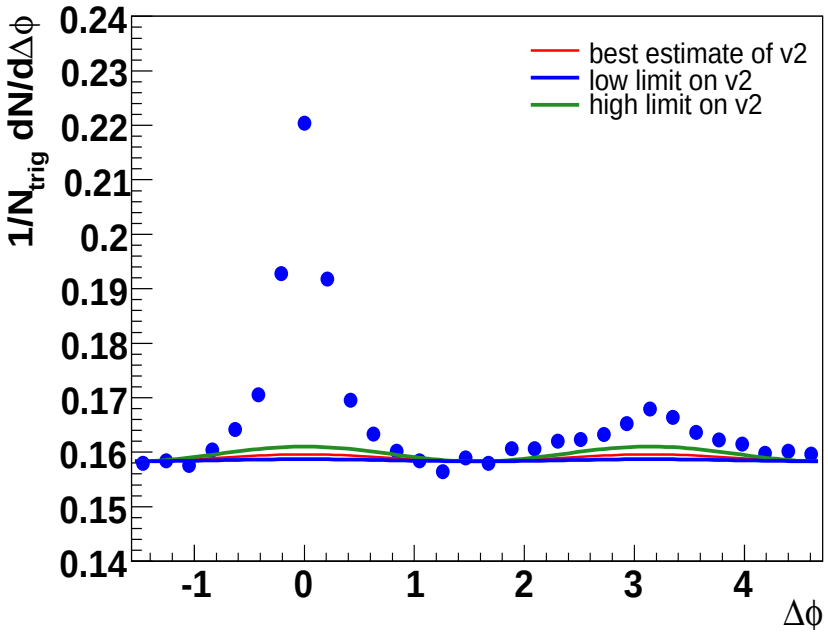

Figure 4.9: $\Delta\phi$ distribution in (0-12%) central Au+Au collisions used to extract the away-side yield, 4 GeV/c < p_T^{trig} < 6 GeV/c, p_T^{assoc} > 3 GeV/c. $\Delta\eta$ triangular pair acceptance correction is not applied.

4.3.5 Elliptic flow determination

The elliptic flow measurements from STAR constitute one of the most important results at RHIC, making the case for strong collective motion. The importance of the subject led to the development of new techniques for determining v_2. The various methods have different sensitivities to non-flow effects and v_2 fluctuations, and therefore provide information on the magnitude of the systematic uncertainty.

"Reaction plane" method

The "standard" method used in STAR is the so-called "reaction plane" method [36]. It correlates each particle with the reaction plane determined using all the other particles in the event. Since they are periodic functions, the azimuthal particle

distributions can be written as a Fourier series:

$$\frac{d^3N}{p_T dp_T dy d\phi} = \frac{1}{2\pi}\frac{d^2N}{p_T dp_T dy}\sum_n \Big[x_n \cos(n(\phi-\psi_r) + y_n \sin(n(\phi-\psi_r)\Big], \tag{4.7}$$

where ψ_r is the azimuthal angle of the reaction plane[1]. Writing the distribution as a function of $(\phi-\psi_r)$, the angle with respect to the reaction plane, allows us to study the distributions over multiple events. Given the symmetry of particle emission with respect to the reaction plane, the sine coefficients are zero. With the choice $x_n = 2\,v_n$, we can rewrite Eq. 4.7 as

$$\frac{d^3N}{p_T dp_T dy d\phi} = \frac{1}{2\pi}\frac{d^2N}{p_T dp_T dy}\sum_n 2v_n \cos(n(\phi-\psi_r)) \tag{4.8}$$

The coefficient v_n will be given by

$$v_n = \frac{1}{\frac{1}{2\pi}\frac{d^2N}{p_T dp_T dy}}\frac{1}{2}\frac{1}{\pi}\int \frac{d^3N}{p_T dp_T dy d\phi}\cos(n(\phi-\psi_r))\,d\phi \tag{4.9}$$

v_n will therefore represent the average of $\cos(n(\phi-\psi_r))$ over all particles in all events:

$$v_n = \Big\langle \cos(n(\phi-\psi_r)) \Big\rangle \tag{4.10}$$

The experimentally determined reaction plane is referred to as the ”event plane”. The event plane angle is defined for each harmonic by the angle (ψ_n) of the flow vector Q_n:

$$Q_n \cos(n\psi_n) = \sum_i w_i \cos(n\phi_i) \tag{4.11}$$

$$Q_n \sin(n\psi_n) = \sum_i w_i \sin(n\phi_i) \tag{4.12}$$

or explicitly:

$$\psi_n = \left(\tan^{-1}\frac{\sum_i w_i \sin(n\phi_i)}{\sum_i w_i \cos(n\phi_i)}\right)/n \tag{4.13}$$

The sums go over the i particles used in the event plane determination and w_i are weights. The weights are chosen to optimize the reaction plane resolution.

[1] As a reminder, the reaction plane is defined by the impact parameter line and the beam line.

Sometimes this can be done by selecting the particles of one particular type, or weighting with transverse momentum of the particles, etc. Because the finite number of detected particles produces limited resolution in the angle of the measured event plane, the coefficients determined using the measured event plane must be corrected with the event plane resolution. The resolution is estimated from the correlation of the event planes of independent sub-events (sub-groups of the particles used for the event plane determination).

For $n = 2$, the procedure described above allows the determination of the elliptic flow coefficient, v_2. STAR used this technique to measure the v_2 as a function of p_T for various centrality classes. This was the first method used to determine v_2, but since the flow itself is used to determine the reaction plane, the method has the implicit assumption that it considers "non-flow" effects as being negligible. Non-flow effects are correlations not associated with the reaction plane: particle correlations due to kinematic constraints between decay products, inter- and intra-jet correlations etc. They have been shown to have a non-negligible contribution in RHIC collisions, and subtracting them in this method would necessitate an exhaustive knowledge of all non-flow sources.

4-particle cumulant method

A method that has the advantage of being much less impacted by the non-flow effects is the 4-particle cumulants method, introduced in [37]. Since elliptic flow is a collective effect, it is a correlation of all particles with the reaction plane and multi-particle correlations are a good candidate to study the elliptic flow. Cumulants are the ideal tool since the cumulant of $2k$-particle azimuthal correlations subtracts the lower order correlations, so that it reflects only genuine $2k$-particle correlations.

The cumulants of 4-particle correlations are defined as

$$\begin{aligned} c_n\{4\} &= \left\langle\left\langle e^{in(\phi_1+\phi_2-\phi_3-\phi_4)}\right\rangle\right\rangle \equiv \left\langle e^{in(\phi_1+\phi_2-\phi_3-\phi_4)}\right\rangle - \left\langle e^{in(\phi_1-\phi_3)}\right\rangle\left\langle e^{in(\phi_2-\phi_4)}\right\rangle - \left\langle e^{in(\phi_1-\phi_4)}\right\rangle\left\langle e^{in(\phi_2-\phi_3)}\right\rangle \\ &= \left\langle e^{in(\phi_1+\phi_2-\phi_3-\phi_4)}\right\rangle - 2\left(\left\langle e^{in(\phi_1-\phi_3)}\right\rangle\left\langle e^{in(\phi_2-\phi_4)}\right\rangle\right)^2 \end{aligned} \tag{4.14}$$

It is obvious from Eq. 4.14 that the 2-particle correlations are subtracted. In the

case of an isotropic distribution (no flow), the cumulant will only involve direct 4-particle correlations, that are of order $1/N^3$, where N is the number of particles measured in the event. It can be shown [38] that for the anisotropic case (flow present), the cumulant is related to flow by the relation:

$$c_n\{4\} = -v_n^4 + O\left(\frac{1}{N^3}\frac{v_{2n}^2}{N^2}\right) \tag{4.15}$$

where v_n is the n-th Fourier coefficient of the azimuthal distribution with respect to the reaction plane : $v_n = \left\langle e^{in(\phi-\psi_r)} \right\rangle$ (This is identical to our previous definition of $v_n = \left\langle \cos(in(\phi-\psi_r)) \right\rangle$ since the sine terms cancel due to symmetry). In the case of v_2, $v_4 << N\,v_2$ and the term v_{2n}^2/N^2 is smaller than $1/N^3$. Therefore $v_2^4 = -c_2\{4\}$ with an error of less than $1/N^3$.

The measurement of v_2 implies therefore determining the cumulant value $c_2\{4\}$. This can be done using the definition relation 4.14 but in practice it is easier to determine it using the generating function defined in [38] as:

$$G_n(z) = \prod_{j=1}^{M}\left(1 + \frac{z^* e^{in\phi_j} + z e^{-in\phi_j}}{M}\right) \tag{4.16}$$

where z is an arbitrary complex number. One averages $G_n(z)$ over many events, obtaining the averaged generating function $\langle G_n(z)\rangle$ ($\langle G_2(z)\rangle$ for v_2 measurements). The cumulants are then related to the generating function by the formula:

$$M\left(\langle G_2(z)\rangle^{1/M} - 1\right) = \sum_k \frac{|z|^{2k}}{(k!)^2} c_2\{2k\} \tag{4.17}$$

The coefficient $c_2\{4\}$ can be then obtained, and v_2 is given by $v_2 = (-c_2\{4\})^{1/4}$

4.3.6 v_2 values used in the analysis

For the Au+Au collisions, STAR measured v_2 using the reaction plane method and the 4-particle cumulant method as a function of p_T for each centrality class. We parametrized the data points obtained with the two methods, and we used those parameterizations as the lower and upper limit on v_2. We used the average of the

two parameterizations as our best estimate of v_2. This allowed us to calculate v_2 for p_T^{trig} and p_T^{assoc} for each case we used.

The Cu+Cu collisions have a much smaller multiplicity, and the statistics does not allow for the use of the 4-particle cumulant method. Also, using the limited number of tracks detected with the TPC to determine the reaction plane and the flow using the reaction plane method would be highly influenced by the non-flow effects. A way to subtract the non-flow effects is to apply the reaction plane method for p+p collisions and subtract their v_2 (which is just non-flow) from the v_2 obtained in Cu+Cu with the same method. The v_2 values obtained this way are used as the lower limit on v_2. Another approach taken by STAR in order to minimize the non-flow effects was to use the tracks from the two forward TPCs (two TPCs situated on both sides of the interaction point that cover the pseudo-rapidity ranges $2.5 < |\eta| < 4.0$). Using the tracks from the two FTPCs as separate sub-events helps determine flow and reduce non-flow effects. This has been used as the upper limit on v_2. The average of the two methods was used as the best v_2 estimate.

Chapter 5

Results

5.1 Near side yields

The analysis technique used to extract the near-side associated yields was presented in Section 4.3.3. We present here the results from the three collision systems under study (d+Au, Cu+Cu and Au+Au collisions), and we investigate their behavior as a function of the number of participants N_{part}.

5.1.1 d+Au results

In order to study the medium modifications of jet-like correlations, we need to measure them in a reference system. The natural choice would be p+p collisions, however, the minimum bias p+p data set available has limited statistics, insufficient for this analysis. d+Au collisions do not produce a medium and it has been shown (see Section 2.3.2) that dihadron correlations have the same characteristics in d+Au collisions and p+p collisions. We can take advantage therefore of the larger data set available for d+Au collisions and use the results from d+Au collisions as a reference for determining the medium modifications in heavy ion collisions.

Fig. 5.1 shows the acceptance and efficiency corrected $\Delta\phi$-$\Delta\eta$ distributions of hadrons associated with a high-p_T trigger hadron. The kinematic ranges of the triggers are $4 < p_T^{trig} < 6$ GeV/c for the left panel and $6 < p_T^{trig} < 10$ GeV/c for the right

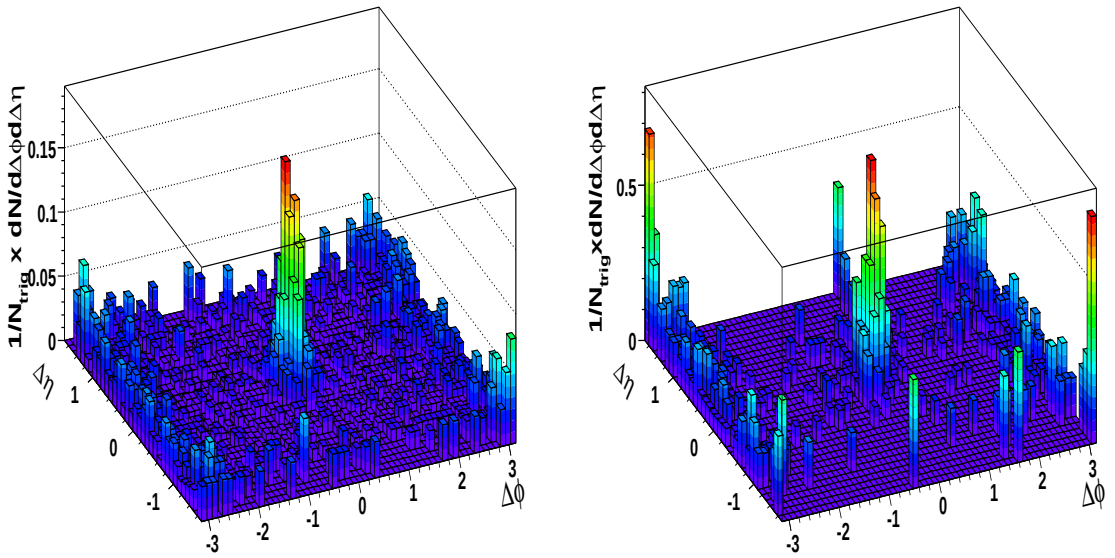

Figure 5.1: Acceptance and efficiency corrected $\Delta\phi$-$\Delta\eta$ histogram for d+Au collisions. (a) $4 < p_T^{trig} < 6$ GeV/c, $3\,\text{GeV/c} < p_T^{assoc} < p_T^{trig}$, (b) $6 < p_T^{trig} < 10$ GeV/c, $3\,\text{GeV/c} < p_T^{assoc} < p_T^{trig}$.

Table 5.1: Number of triggers found in d+Au collisions for each kinematic range

p_T^{trig} range	$N_{triggers}$
$4 < p_T^{trig} < 6$ GeV/c	25787
$6 < p_T^{trig} < 10$ GeV/c	2066

panel. The associated particles have $3\,\text{GeV/c} < p_T^{assoc} < p_T^{trig}$.

As can be seen, for d+Au collisions the dihadron correlations show only the near- and away-side jet-like correlations above a flat uncorrelated background. For the p_T^{trig} and p_T^{assoc} used in this analysis, the background is very small. Table 5.1 shows the number of trigger hadrons found for each kinematic range.

The near-side jet-like yield is defined as

$$Y_{AA}^{near} = \int_{-0.7}^{0.7} d(\Delta\eta) \int_{-0.78}^{0.78} d(\Delta\phi) \frac{1}{N_{trig}} \frac{d^2 N_{corrected}}{d(\Delta\eta) d(\Delta\phi)} \tag{5.1}$$

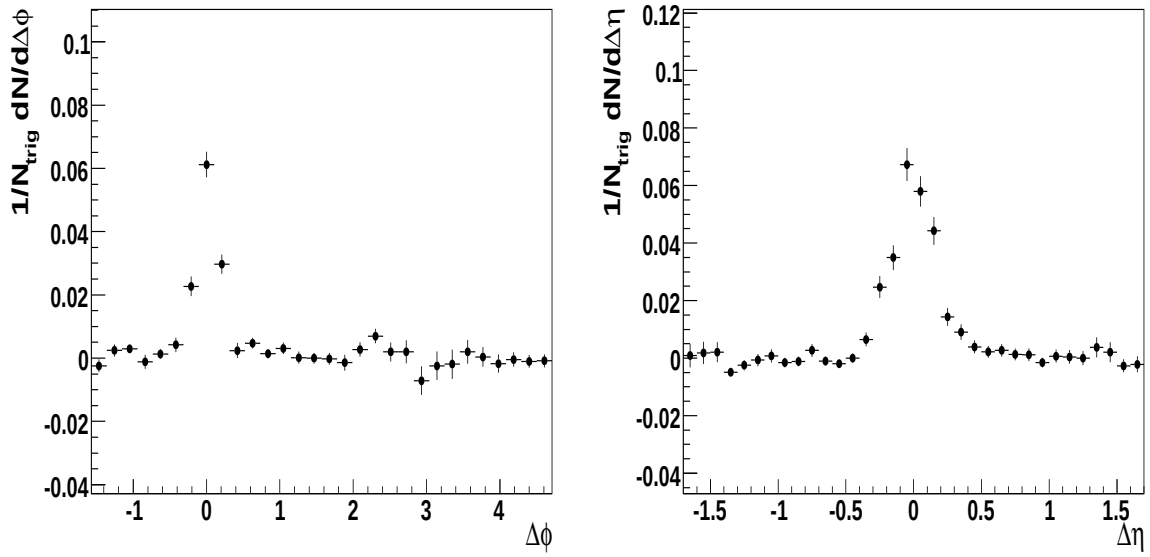

Figure 5.2: (a) Background subtracted $\Delta\phi$ correlations in d+Au collisions. (b) Background subtracted $\Delta\eta$ correlations in d+Au collisions. For both panels $4 < p_T^{trig} < 6$ GeV/c, $3\,\mathrm{GeV/c} < p_T^{assoc} < p_T^{trig}$.

Table 5.2: Near-side yields in d+Au collisions extracted using the $\Delta\phi$ and $\Delta\eta$ methods.

p_T^{trig} range	$Y_{\Delta\phi}$	$Y_{\Delta\eta}$
$4 < p_T^{trig} < 6$ GeV/c	0.0264±0.0016	0.00265±0.0015
$6 < p_T^{trig} < 10$ GeV/c	0.0749±0.0091	0.0803±0.0078

where $N_{corrected}$ denotes the acceptance and efficiency corrected distributions. Although there is no flow or ridge contribution in d+Au collisions, we used the same methods we used for Cu+Cu and Au+Au collisions for consistency. As described in Section 4.3.3, the two methods make use of the projection of the two-dimensional distributions onto $\Delta\phi$ and $\Delta\eta$ respectively. The background subtracted correlations are presented in Fig. 5.2 and Fig. 5.3 for the two trigger ranges used.

The yields obtained with the two methods are listed in Table 5.2. As can be seen, the two methods yield consistent results.

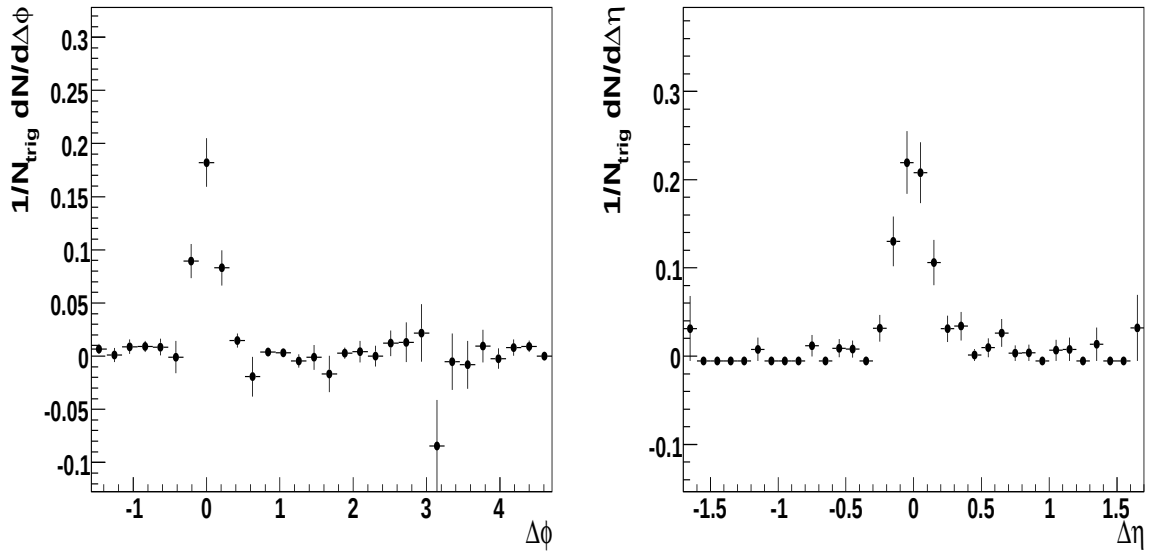

Figure 5.3: (a) Background subtracted $\Delta\phi$ correlations in d+Au collisions. (b) Background subtracted $\Delta\eta$ correlations in d+Au collisions. For both panels $6 < p_T^{trig} < 10$ GeV/c, $3\,\mathrm{GeV/c} < p_T^{assoc} < p_T^{trig}$.

As mentioned in Section 2.5, the effect of the medium on jet fragmentation can be explored in more detail using the dihadron fragmentation functions of near- and away-side associated hadrons. $D(z_T)$, where $z_T = p_T^{assoc}/p_T^{trig}$, is measurable without direct knowledge of the parton energy and provides a theoretically calculable alternative to true fragmentation functions. The definition of $D(z_T)$ is given by

$$D_{AA}(z_T, p_T^{trig}) \equiv p_T^{trig} \frac{d\sigma_{AA}^{h_1h_2}/dp_T^{trig}dp_T^{assoc}}{d\sigma_{pp}^{h_1h_2}/dp_T^{trig}}, \tag{5.2}$$

As mentioned previously, we use the d+Au results as our reference instead of the p+p ones.

In order to determine the dihadron fragmentation functions, we divide the associated particles according to their z_T into 7 z_T bins of 0.1 width. For each z_T bin we construct two-particle correlations including all pairs that have an associated particle in that z_T bin. The same procedure used to obtain the near-side jet yields is applied to each z_T bin $\Delta\phi$-$\Delta\eta$ distribution. We thus obtain the values of the

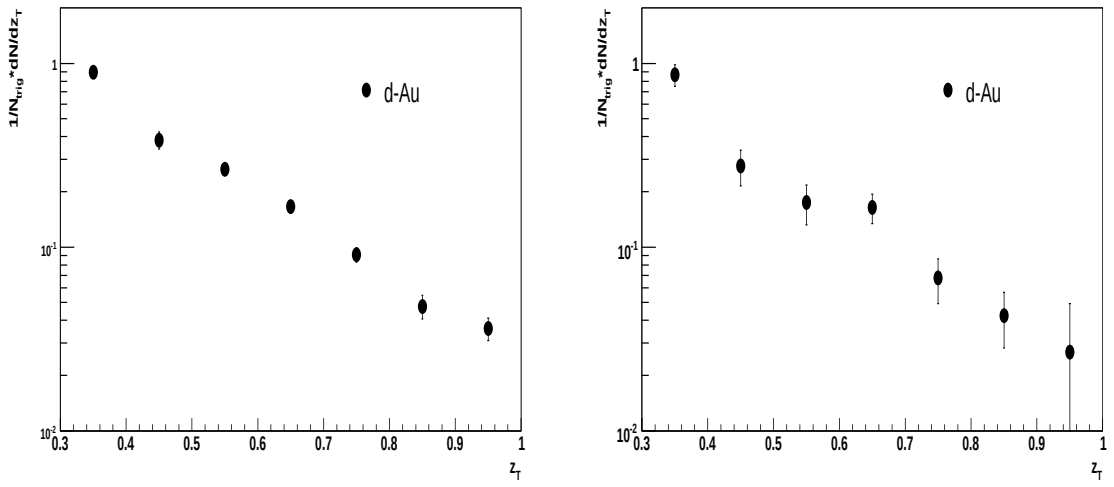

Figure 5.4: Dihadron fragmentation functions in d+Au collisions. (a) $4 < p_T^{trig} < 6$ GeV/c, (b) $6 < p_T^{trig} < 10$ GeV/c.

dihadron fragmentation for each z_T. The dihadron fragmentation functions for the two trigger ranges, $4 < p_T^{trig} < 6$ GeV/c and $6 < p_T^{trig} < 10$ GeV/c are shown in Fig. 5.4. We will use them to compare with the dihadron fragmentation functions obtained in Cu+Cu and Au+Au collisions and look for modifications due to interaction with the medium.

5.1.2 Cu+Cu results

We investigated Cu+Cu collisions in 4 centrality classes: 0-10%, 10-20%, 20-40% and 40-60%. As an example, we show the two-dimensional $\Delta\phi$-$\Delta\eta$ distributions for central (0-10%) Cu+Cu collisions in Fig. 5.5. It is seen that the background is much higher than in d+Au collisons. There is no apparent flow or ridge component. The elliptic flow is small in central collisions, and the ridge has a minimal contribution in Cu+Cu collisions in the kinematic range considered, as we will show later. The number of triggers found for each p_T^{trig} and centrality is listed in Table 5.3.

The $\Delta\phi$ and $\Delta\eta$ background subtracted correlations are presented in Fig. 5.6 and Fig. 5.7 for each centrality for the two trigger ranges used. The near-side jet-like

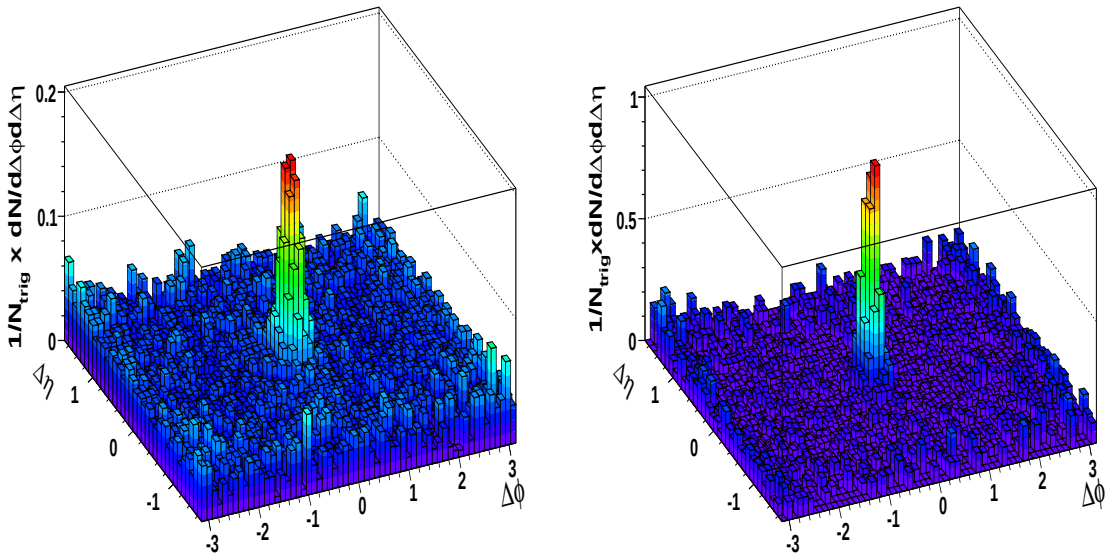

Figure 5.5: Acceptance and efficiency corrected $\Delta\phi$-$\Delta\eta$ histogram for central 0-10% Cu+Cu collisions. (a) $4 < p_T^{trig} < 6$ GeV/c, $3\,\mathrm{GeV/c} < p_T^{assoc} < p_T^{trig}$, (b) $6 < p_T^{trig} < 10$ GeV/c, $3\,\mathrm{GeV/c} < p_T^{assoc} < p_T^{trig}$.

Table 5.3: Number of triggers found in Cu+Cu collisions for each kinematic range and centrality.

	$N_{triggers}$			
p_T^{trig} range	0-10%	10-20%	20-40%	40-60%
$4 < p_T^{trig} < 6$ GeV/c	147307	121674	157098	69673
$6 < p_T^{trig} < 10$ GeV/c	11597	9466	12506	5602

yields are extracted from these histograms by adding the bins in the $|\Delta\phi| < 0.78$ region (for the $\Delta\phi$ method) and the $|\Delta\eta| < 0.7$ region (for the $\Delta\eta$ method).

The near-side jet-like yields obtained are listed in Table 5.4. As can be observed, the two methods give consistent results, which represent a useful consistency check. The yields for the various centrality bins are equal within errors, and they

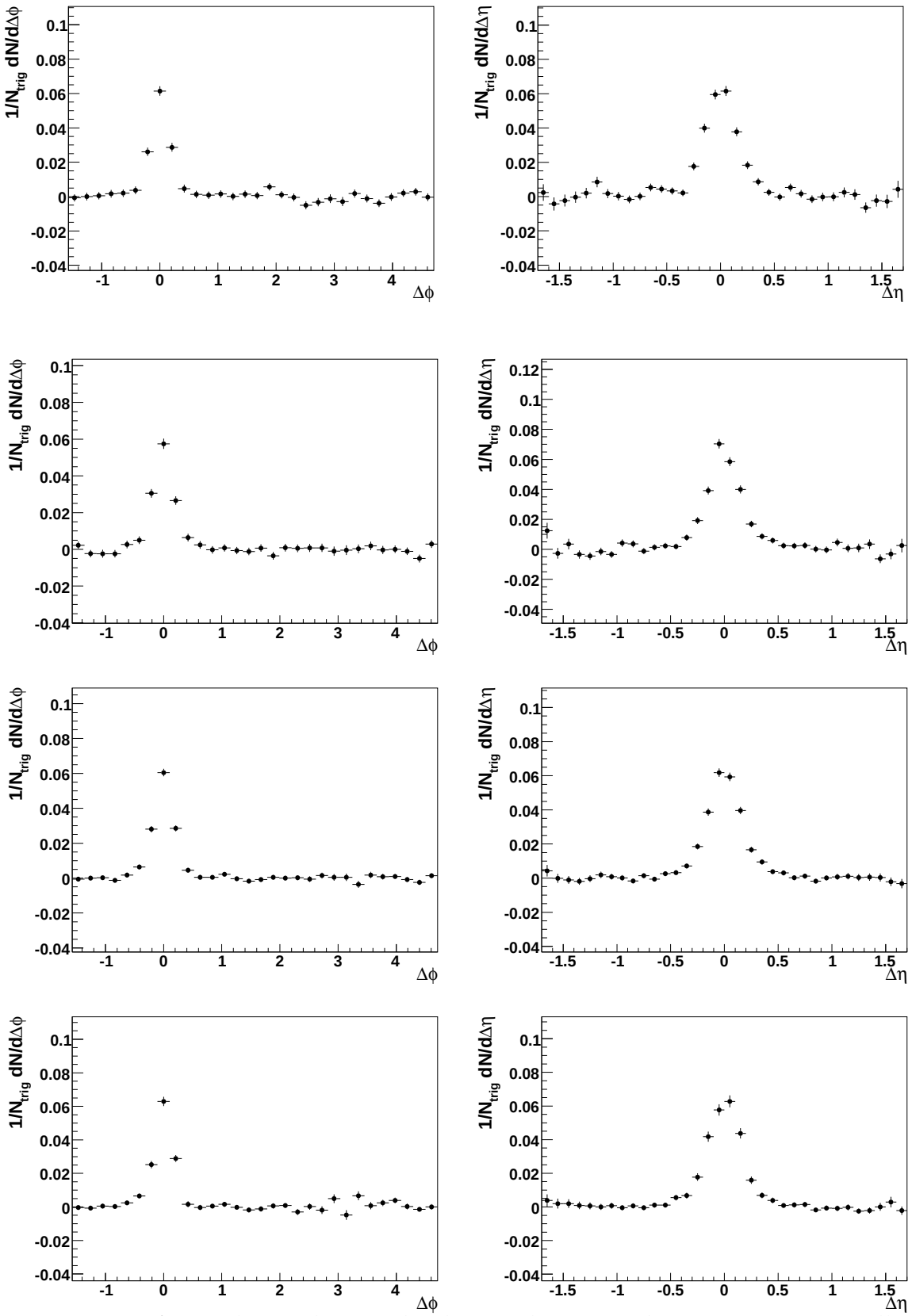

Figure 5.6: Left panels: Background subtracted $\Delta\phi$ correlations in Cu+Cu collisions. Right panels: Background subtracted $\Delta\eta$ correlations in Cu+Cu collisions. For all panels $4 < p_T^{trig} < 6$ GeV/c, $3\,\text{GeV/c} < p_T^{assoc} < p_T^{trig}$. Each row shows the distributions for a centrality class: 0-10%, 10-20%, 20-40% and 40-60% (starting from the top row).

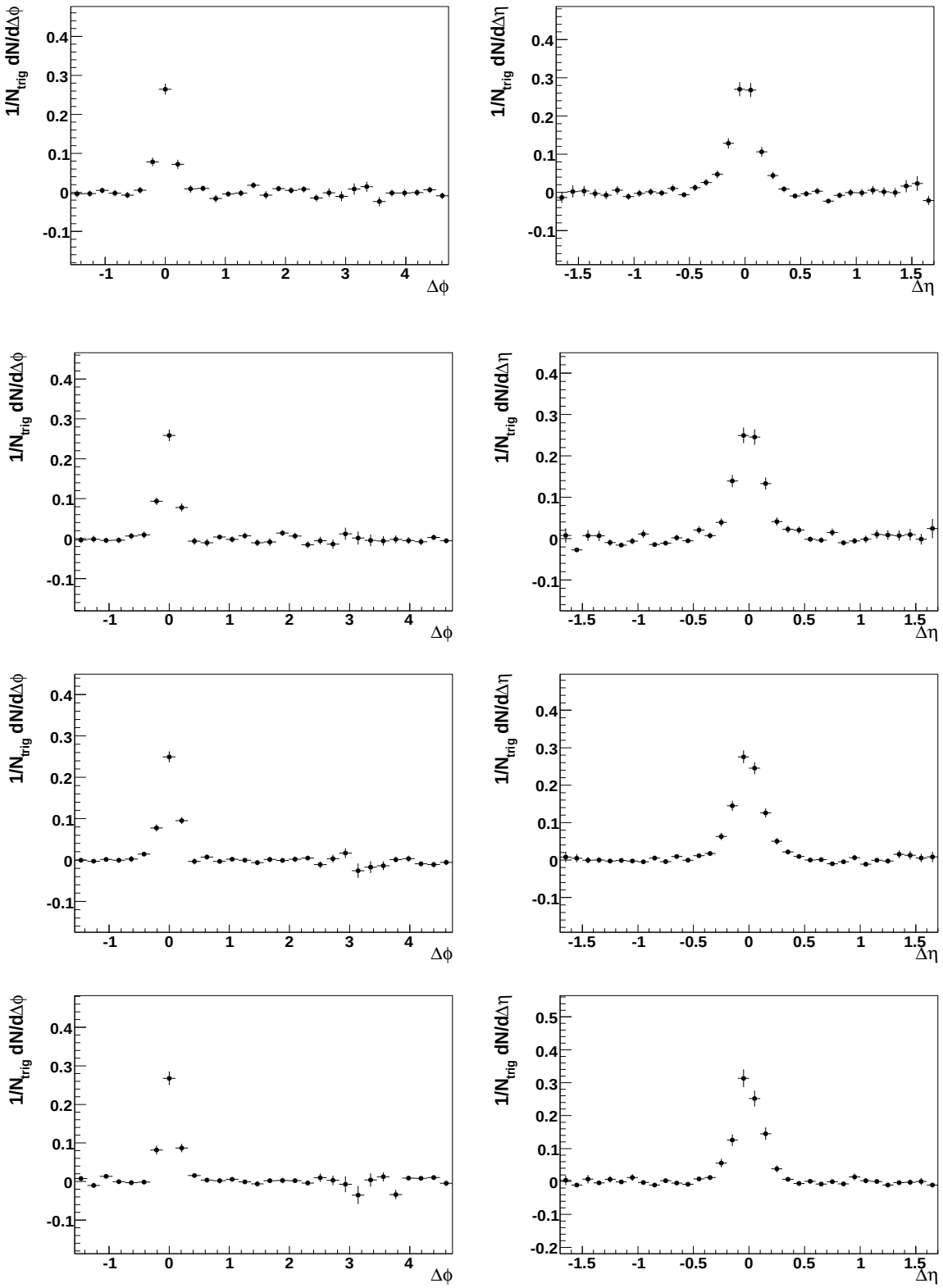

Figure 5.7: Left panels: Background subtracted $\Delta\phi$ correlations in Cu+Cu collisions. Right panels: Background subtracted $\Delta\eta$ correlations in Cu+Cu collisions. For all panels $6 < p_T^{trig} < 10$ GeV/c, $3\,\mathrm{GeV/c} < p_T^{assoc} < p_T^{trig}$. Each row shows the distributions for a centrality class: 0-10%, 10-20%, 20-40% and 40-60% (starting from the top row).

are consistent with the d+Au near-side jet-like yields. We will show later the dependence of near-side yields on the number of participants for the three systems studied.

Table 5.4: Near-side yields in Cu+Cu collisions for each kinematic range and centrality. Results obtained with both the $\Delta\phi$ and $\Delta\eta$ methods are presented.

Centrality	$4 < p_T^{trig} < 6$ GeV/c		$6 < p_T^{trig} < 10$ GeV/c	
	$Y_{\Delta\phi}$	$Y_{\Delta\eta}$	$Y_{\Delta\phi}$	$Y_{\Delta\eta}$
0-10%	0.0267±0.0017	0.0266±0.0013	0.0906±0.0067	0.0906±0.0057
10-20%	0.0274±0.0016	0.0277±0.0012	0.0899±0.0062	0.0910±0.0054
20-40%	0.0273±0.0011	0.0264±0.0009	0.0928±0.0051	0.0976±0.0044
40-60%	0.0266±0.0012	0.0267±0.0011	0.0943±0.0057	0.0930±0.0056

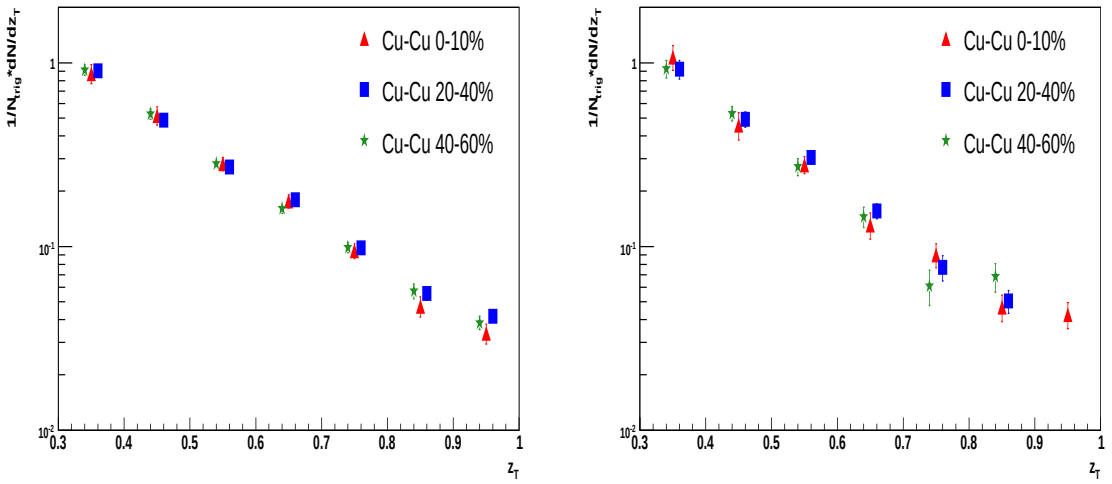

Figure 5.8: Near-side dihadron fragmentation functions in Cu+Cu collisions for the three centrality classes studied. (a) $4 < p_T^{trig} < 6$ GeV/c, (b) $6 < p_T^{trig} < 10$ GeV/c.

The dihadron fragmentation functions are obtained for three Cu+Cu centrality

classes using the method described in Section 5.1.1. The results are presented in Fig. 5.8 for the two trigger selections.

5.1.3 Au+Au results

In order to compare the results in the two collision systems (Cu+Cu and Au+Au collisions) and study their dependence on N_{part}, we investigated Au+Au collisions in 6 centrality classes: 0-12%, 10-20%, 20-30%, 30-40%, 40-60% and 60-80%. The two-dimensional $\Delta\phi$-$\Delta\eta$ distributions for central (0-12%) Au+Au collisions are shown in Fig. 5.9. The background is obviously higher than in Cu+Cu collisons, due to the larger multiplicities of central Au+Au collisions. For the 6 centralities studied, the number of trigger particles found in the two kinematic ranges selected ($4 < p_T^{trig} < 6$ GeV/c and $6 < p_T^{trig} < 10$ GeV/c) are listed in Table 5.5.

Table 5.5: Number of triggers found in Au+Au collisions for each kinematic range and centrality.

	$N_{triggers}$					
p_T^{trig} range	0-12%	10-20%	20-30%	30-40%	40-60%	60-80%
$4 < p_T^{trig} < 6$ GeV/c	2393351	589856	206000	137345	149176	44642
$6 < p_T^{trig} < 10$ GeV/c	158311	39296	14578	9858	11236	3613

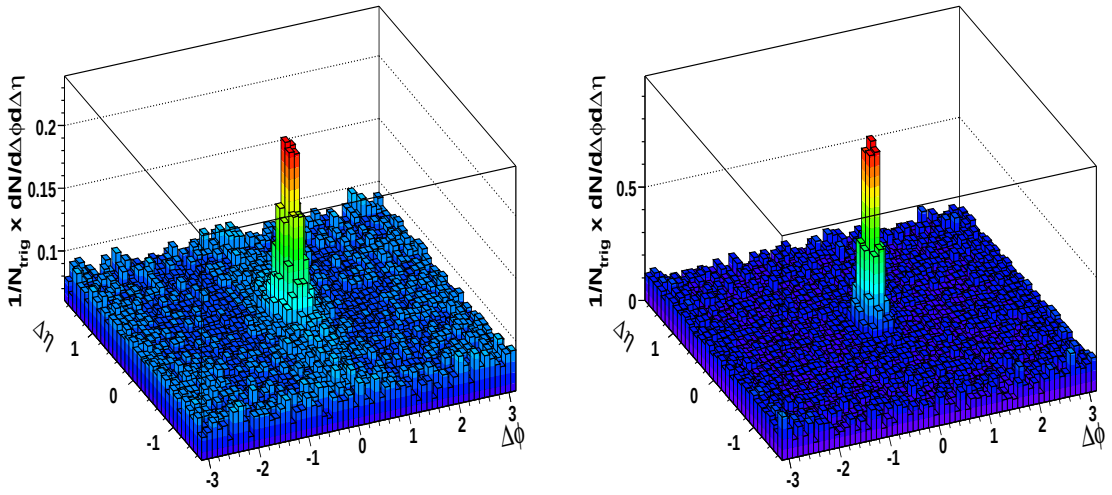

Figure 5.9: Acceptance and efficiency corrected $\Delta\phi$-$\Delta\eta$ histogram for central 0-12% Au+Au collisions. (a) $4 < p_T^{trig} < 6$ GeV/c, $3\,\text{GeV/c} < p_T^{assoc} < p_T^{trig}$, (b) $6 < p_T^{trig} < 10$ GeV/c, $3\,\text{GeV/c} < p_T^{assoc} < p_T^{trig}$.

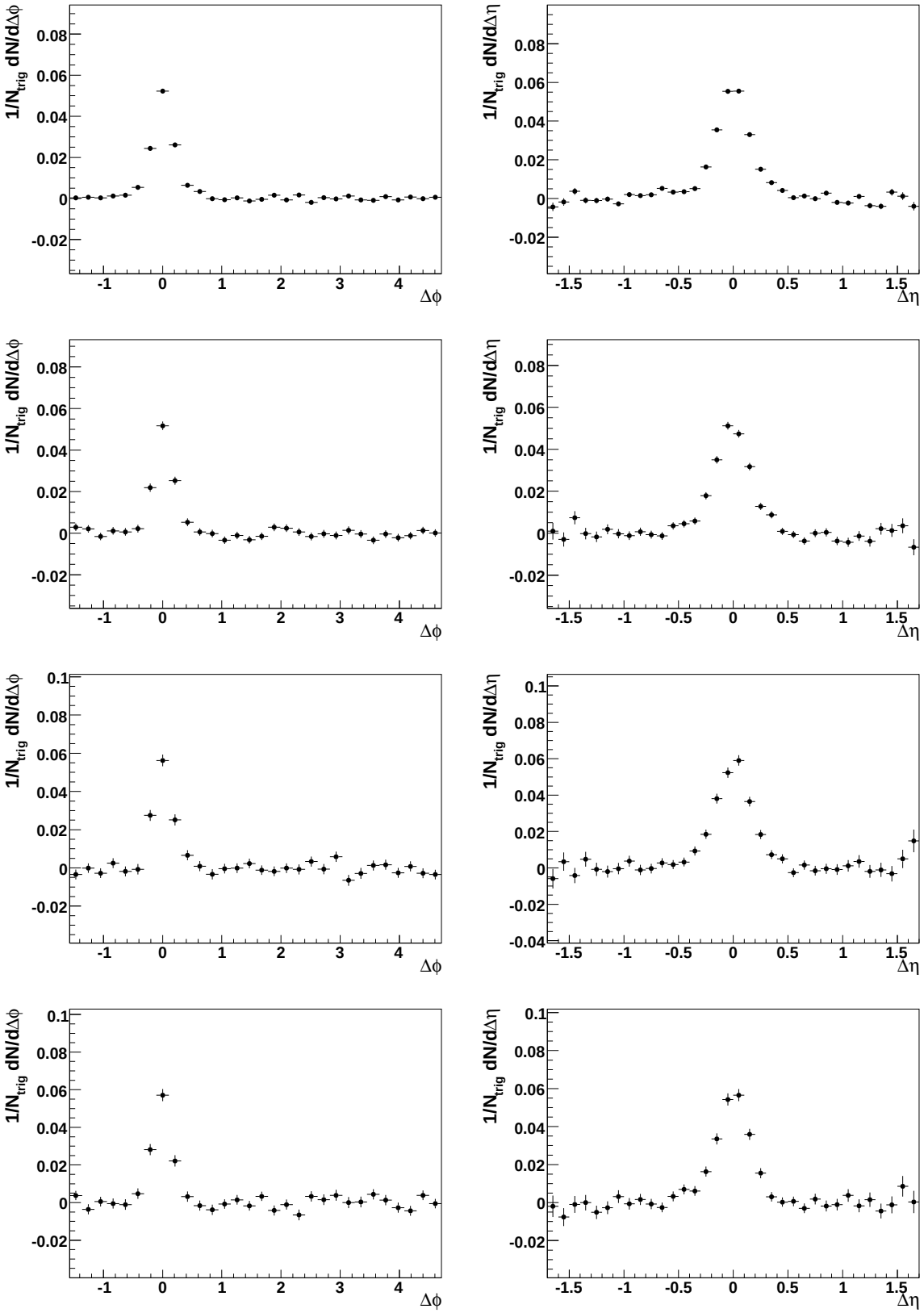

Figure 5.10

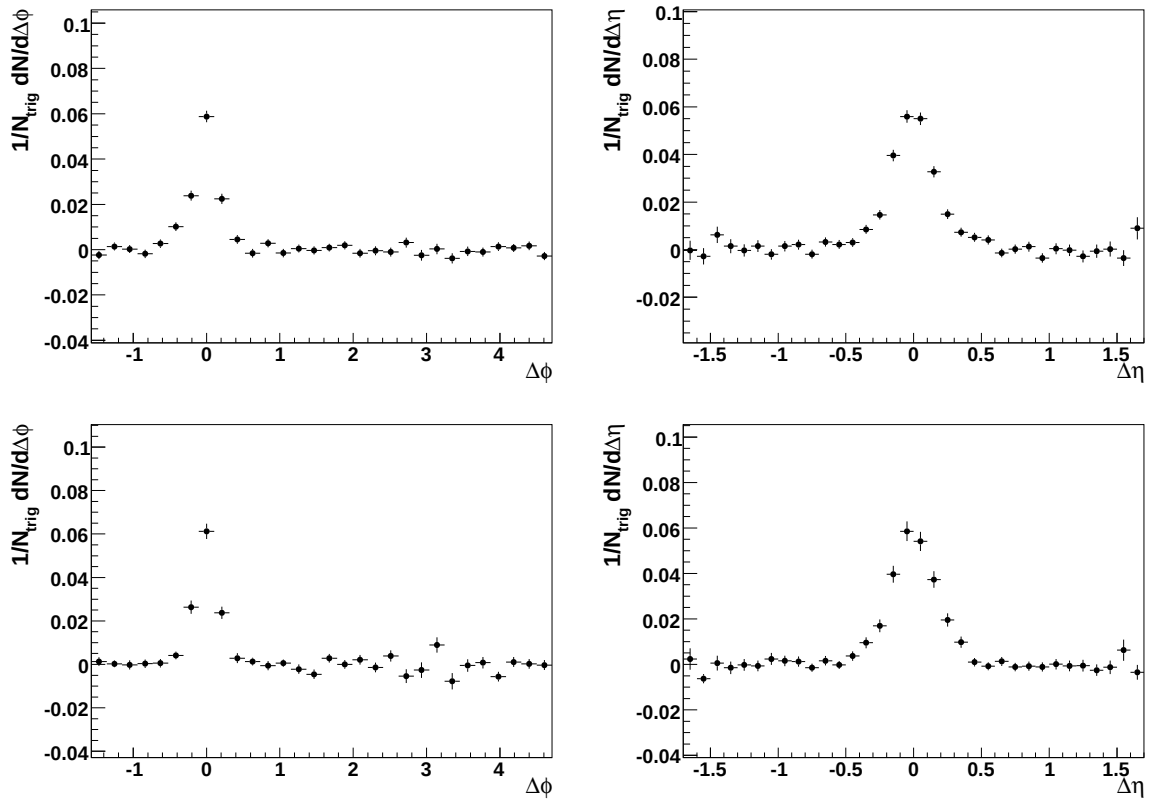

Figure 5.10: Left panels: Background subtracted $\Delta\phi$ correlations in Au+Au collisions. Right panels: Background subtracted $\Delta\eta$ correlations in Au+Au collisions. For all panels $4 < p_T^{trig} < 6$ GeV/c, $3\,\mathrm{GeV/c} < p_T^{assoc} < p_T^{trig}$. Each row shows the distributions for a centrality class: 0-12%, 10-20%, 20-30%, 30-40%, 40-60% and 60-80% (starting from the top row).

The $\Delta\phi$ and $\Delta\eta$ background subtracted correlations used to extract the near-side yields are presented in Fig. 5.10 for $4 < p_T^{trig} < 6$ GeV/c and Fig. 5.11 for $6 < p_T^{trig} < 10$ GeV/c. Each row corresponds to a centrality class, the left panels representing the $\Delta\phi$ background subtracted correlations and the right panels representing the $\Delta\eta$ background subtracted correlations.

The near-side jet-like yields obtained for each centrality selection are listed in Table 5.6. As observed in the Cu+Cu results, the two methods give consistent results, and the yields are similar for all of the centralities studied.

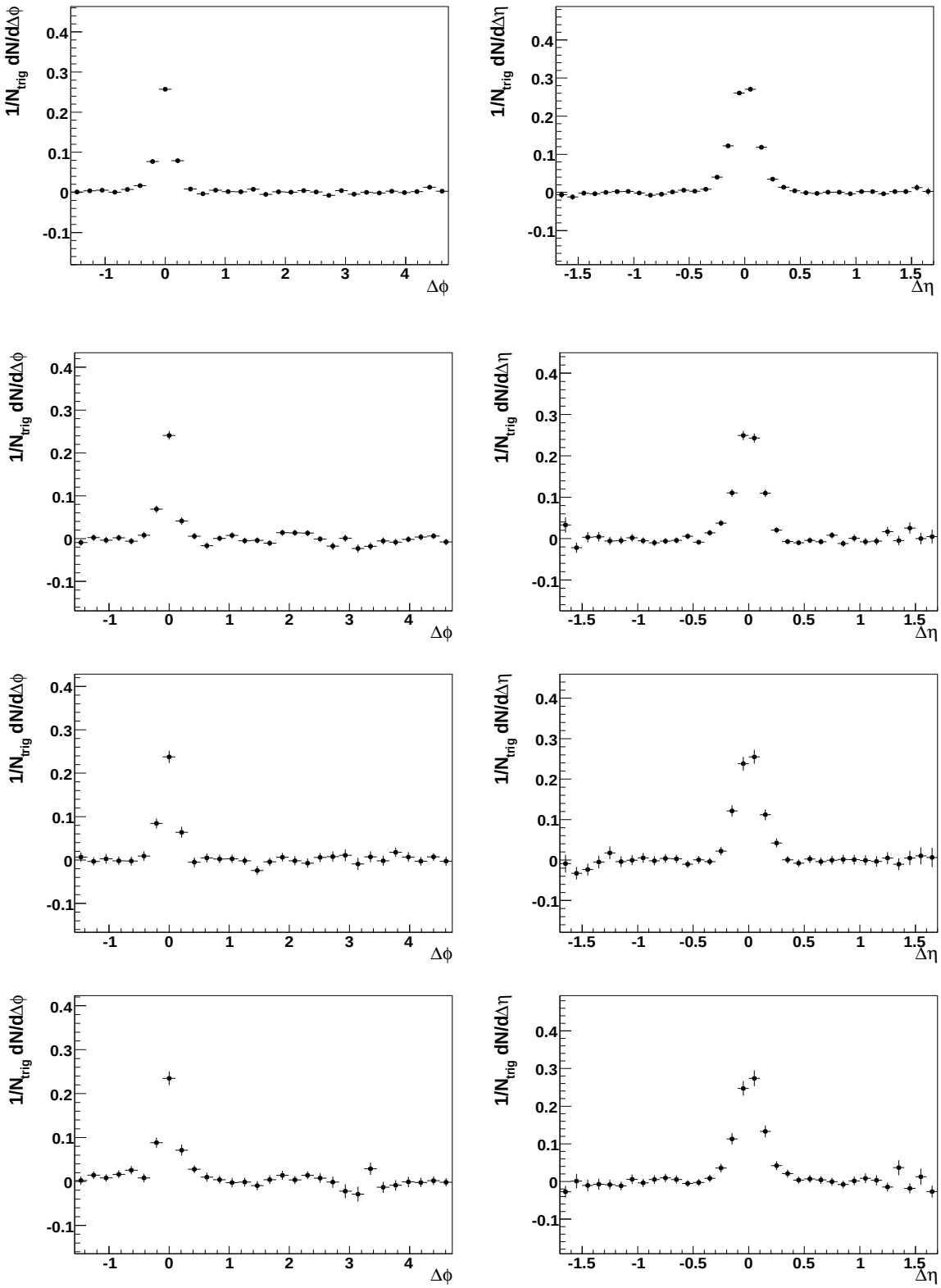

Figure 5.11

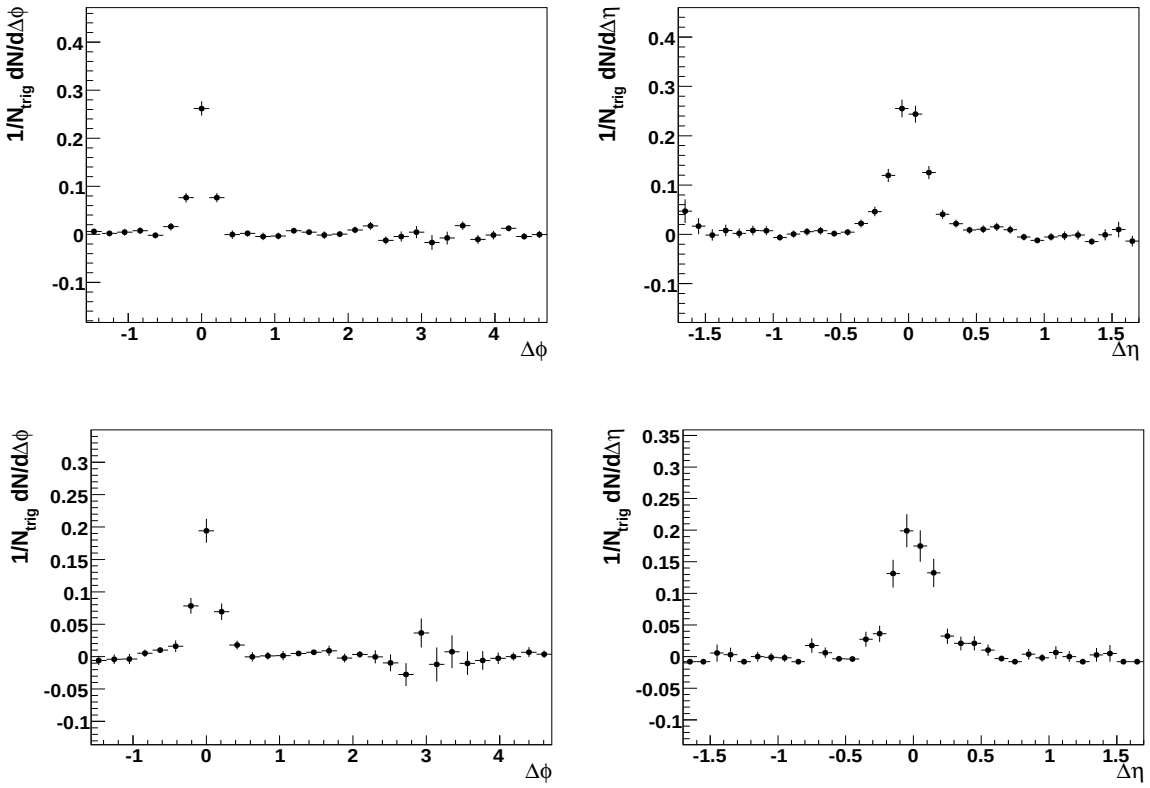

Figure 5.11: Left panels: Background subtracted $\Delta\phi$ correlations in Au+Au collisions. Right panels: Background subtracted $\Delta\eta$ correlations in Au+Au collisions. For all panels $6 < p_T^{trig} < 10$ GeV/c, $3\,\mathrm{GeV/c} < p_T^{assoc} < p_T^{trig}$. Each row shows the distributions for a centrality class: 0-12%, 10-20%, 20-30%, 30-40%, 40-60% and 60-80% (starting from the top row).

The dihadron fragmentation function in central (0-12%) Au+Au collisions was also determined (see Fig. 5.12) and used for comparison with the results in Cu+Cu collisions. This allows us to compare the near-side dihadron fragmentation functions for systems with very different N_{part}- N_{part}=326 for central Au-Au (0-12%) collisions, whereas N_{part}=98 for central (0-10%) Cu+Cu collisions.

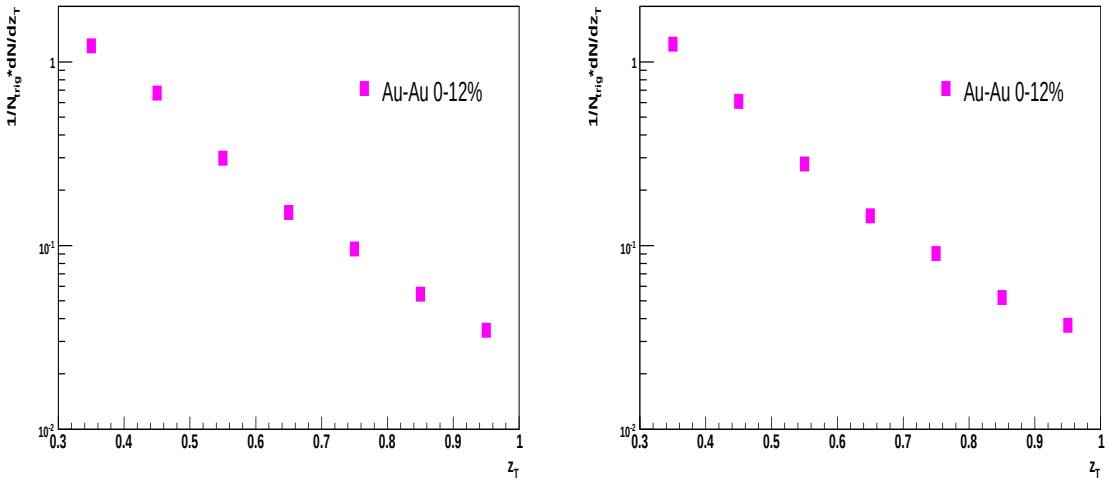

Figure 5.12: Near-side dihadron fragmentation functions in central 0-12% Au+Au collisions. (a) $4 < p_T^{trig} < 6$ GeV/c, (b) $6 < p_T^{trig} < 10$ GeV/c. The error bars are not visible since they are smaller than the marker size.

Table 5.6: Near-side yields in Au+Au collisions for each kinematic range and centrality. Results obtained with both the $\Delta\phi$ and $\Delta\eta$ methods are presented.

Centrality	$4 < p_T^{trig} < 6$ GeV/c		$6 < p_T^{trig} < 10$ GeV/c	
	$Y_{\Delta\phi}$	$Y_{\Delta\eta}$	$Y_{\Delta\phi}$	$Y_{\Delta\eta}$
0-12%	0.0251±0.0008	0.0242±0.0006	0.0927±0.0032	0.0878±0.0025
10-20%	0.0225±0.0015	0.0214±0.0011	0.0716±0.0061	0.0749±0.0045
20-30%	0.0238±0.0021	0.0251±0.0015	0.0822±0.0084	0.0771±0.0065
30-40%	0.0236±0.0021	0227±0.0016	0.0978±0.0076	0.0887±0.0067
40-60%	0.0253±0.0015	0.0245±0.0012	0.0901±0.0060	0.0921±0.0051
60-80%	0.0252±0.0016	0.0252±0.0014	0.0807±0.0061	0.0782±0.0063

5.1.4 N_{part} dependence of near-side yields

The near-side jet-like yield is presented as a function of number of participant nucleons (N_{part}) in Fig. 5.13 (for $4 < p_T^{trig} < 6$ GeV/c) and Fig. 5.14 (for $6 < p_T^{trig} < 10$ GeV/c). As already mentioned, it can be easily seen that the two analysis methods give consistent results. The Cu+Cu and Au+Au near-side associated yields are consistent within errors for similar N_{part}. The near side yields in heavy ion collisions show no centrality dependence and within errors agree with those in d+Au, as seen also in previous studies of Au+Au collisions [39]. The independence of the near-side associated yields on centrality indicates that high-p_T trigger particles select partons for which fragmentation is largely unmodified by the presence of the medium.

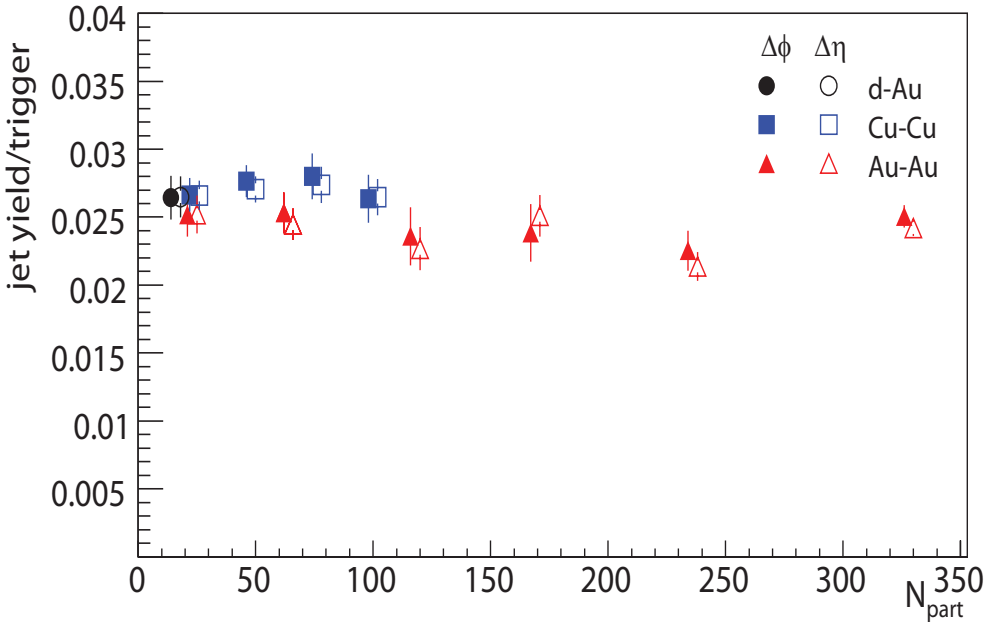

Figure 5.13: N_{part} dependence of the near-side jet yield for $4\,\mathrm{GeV}/c < p_T^{trig} < 6\,\mathrm{GeV}/c$, $p_T^{assoc} > 3$ GeV/c. The solid symbols are the results obtained using the $\Delta\phi$ method, and the hollow symbols are obtained using the $\Delta\eta$ method. The open symbols are horizontally offset for clarity.

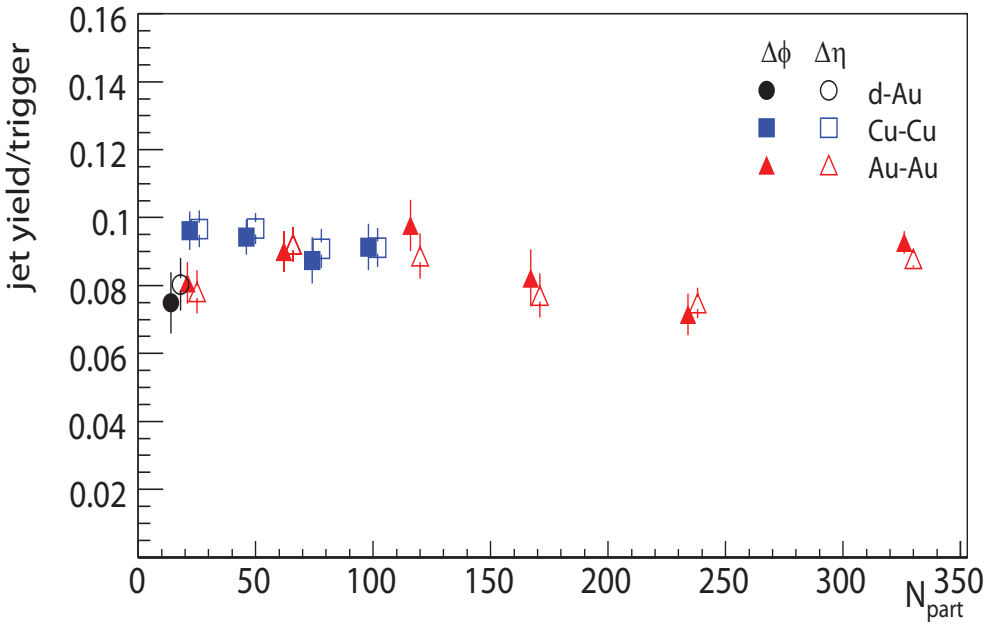

Figure 5.14: N_{part} dependence of the near-side jet yield for $6\,\text{GeV}/c < p_T^{trig} < 10\,\text{GeV}/c$, $p_T^{assoc} > 3\,\text{GeV}/c$. The solid symbols are the results obtained using the $\Delta\phi$ method, and the open symbols are obtained using the $\Delta\eta$ method. The hollow symbols are horizontally offset for clarity.

The lack of modifications in the fragmentation function of the partons producing the dihadron correlations studied is apparent in Fig. 5.15a and 5.15b, which show the ratio of near-side dihadron fragmentation functions in heavy ion collisions to those in d+Au collisions. The ratio is consistent with unity for Cu+Cu collisions, implying no medium modification. Some of the central Au+Au points are slightly above unity, although a similar analysis in STAR has shown the ratio in central Au+Au collisions to be consistent with one, hinting to a larger than estimated systematic uncertainty. It is important to realize that energy loss would reduce the number of trigger particles, so that the independence of the per-trigger near-side yield and dihadron fragmentation functions on centrality does not imply that there is no energy loss for the near-side jet. This behavior occurs if the partons fragment outside the medium, either because the jets selected by the high-p_T trigger

particles are produced close to the surface, or possibly after traversing part of the medium and losing energy in the process. The presence of the ridge in dihadron correlations, especially at lower p_T^{assoc} [34], suggests the latter scenario. However, the ridge production mechanism is still under investigation in the theoretical heavy ion community. It has been shown that the ridge has a significant presence in dihadron correlations with a p_T^{assoc} threshold lower than the one considered in this study (usually $p_T^{assoc} > 2$ GeV/c), suggesting that the ridge is caused by the medium response to an energetic jet. For the kinematic ranges used in this study, the ridge has a small contribution, the only exception being for the lower p_T^{trig} range in central Au+Au collisions. This can be seen in Fig. 5.16, which shows the jet associated yields (squares) and the jet+ridge associated yields (triangles).

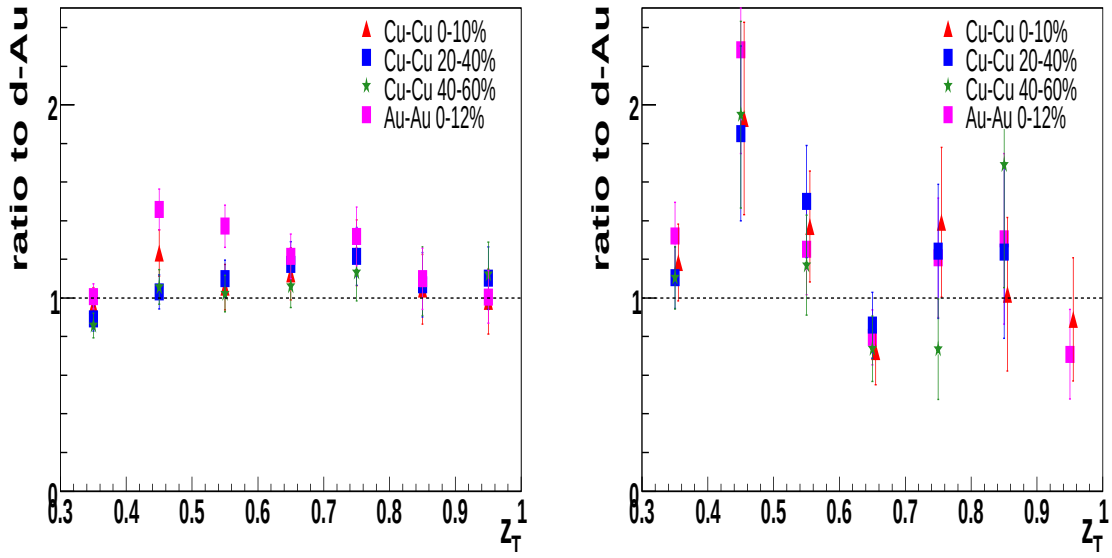

(a) (b)

Figure 5.15: Ratios of dihadron fragmentation functions in heavy ion collisions to d+Au on the near-side for (a)4 GeV/c < p_T^{trig} < 6 GeV/c and (b)6 GeV/c < p_T^{trig} < 10 GeV/c.

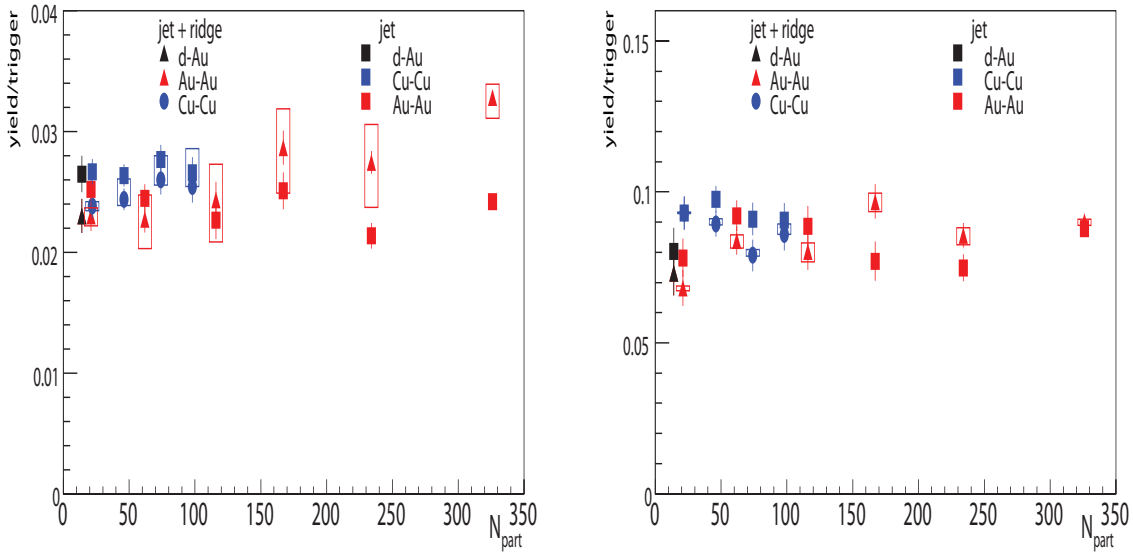

Figure 5.16: N_{part} dependence of the near-side jet yield and jet+ridge yield for (a)4 GeV/c < p_T^{trig} < 6 GeV/c, p_T^{assoc} > 3 GeV/c and (b)6 GeV/c < p_T^{trig} < 10 GeV/c, p_T^{assoc} > 3 GeV/c.

5.2 Away-side yields

As mentioned, the requirement that a high-p_T trigger hadron be observed leads to a geometrical bias. The distribution of hard scattering points that produced the observed hadrons is different for triggered dihadron correlations than for single hadrons. Fig. 5.17 shows the results of a simulation ([40]) showing the probability density of finding a parton production vertex at (x, y) given a trigger hadron with 8 < p_T < 15 GeV/c (left) and the respective probability density given a trigger hadron with 8 < p_T < 15 GeV and an away-side hadron with 4 < p_T < 6 GeV/c. The dihadron correlations appear to be less surface biased than the single hadron spectra. The away-side jet can be used together with the suppression of the single hadron spectra to study the properties of the medium formed by investigating the energy loss of the produced partons.

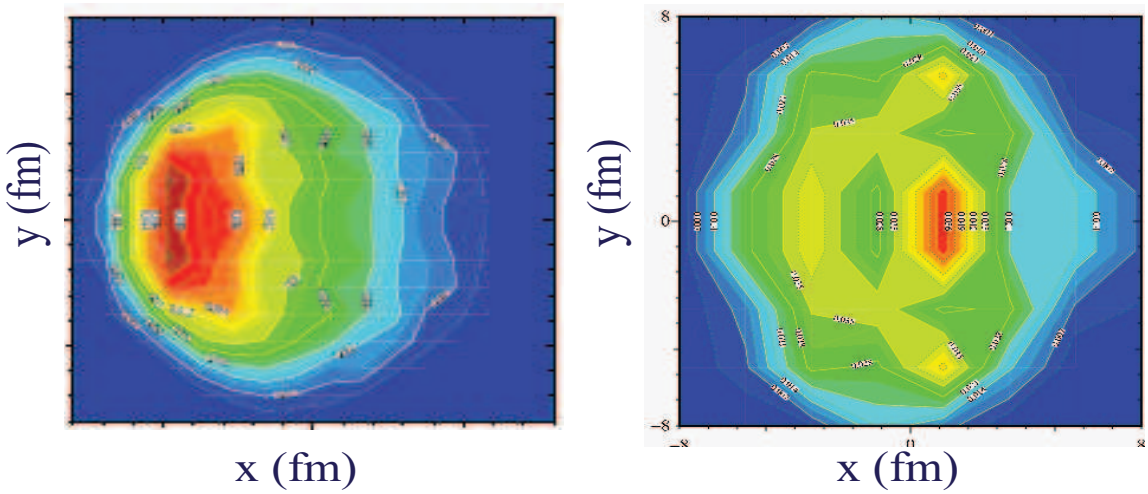

Figure 5.17: (a) Probability density of finding a parton production vertex at (x, y) given a trigger hadron with $8 < p_T^{trig} < 15$ GeV/c. (b) Probability density for finding a vertex at (x, y) leading to a trigger hadron with $8 < p_T^{trig} < 15$ GeV/c and an away-side hadron with $4 < p_T^{assoc} < 6$. For both cases, the near-side (triggered) hadron propagates in the -x direction. Figure from [40].

Earlier studies have shown that the away-side associated yield is suppressed in Au+Au collisions with respect to p+p and d+Au collisions [39, 18]. The suppression is in agreement with several model calculations [25, 41], which use a density and path length distribution that is generated from the initial overlap geometry. The present work investigates the centrality dependence of the suppression in both Au+Au and Cu+Cu collisions. Since the ratio between the shape of the overlap region and the number of participants is different in the two systems, we can test the description of energy loss path length dependence in the models.

5.2.1 d+Au Results

The away-side jet yield is measured by integrating the associated hadrons in the region $|\Delta\phi - \pi| < 1.3$. A background subtraction is applied to remove the dihadron

pairs not originating from jets. In d+Au collisions there is no elliptic flow component, therefore the uncorrelated pairs constitute the only background for our measurement. We thus subtract a flat background, the magnitude of which we determine by assuming we have no jet component in the $0.8 < \Delta\phi < 1.2$ region (at the minimum of our two particle azimuthal correlations). The average of the points in this range will constitute the background level. The standard deviation of the calculated mean is considered to be the error on the background determination and is propagated into our statistical error calculation for the away-side yields. The dihadron azimuthal correlations in d+Au collisions for the two trigger ranges considered are shown in Fig. 5.18. The yields extracted are listed in Table 5.7.

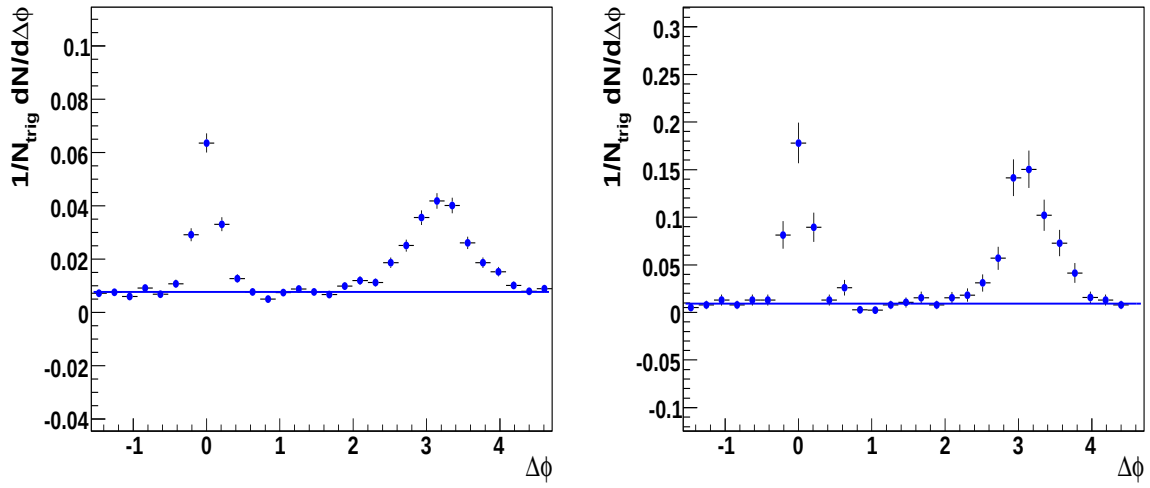

Figure 5.18: Di-hadron azimuthal correlations used to extract the away-side jet-like yields. $4 < p_T^{trig} < 6$ GeV/c, $3\,\text{GeV/c} < p_T^{assoc} < p_T^{trig}$(a) and $6 < p_T^{trig} < 10$ GeV/c, $3\,\text{GeV/c} < p_T^{assoc} < p_T^{trig}$(b).

Table 5.7: Away-side yields in d+Au collisions.

p_T^{trig} range	Y_{away}
$4 < p_T^{trig} < 6$ GeV/c	0.0359 ± 0.0021
$6 < p_T^{trig} < 10$ GeV/c	0.1172 ± 0.0104

As in the study of the near-side jet, we also investigated the away-side dihadron fragmentation functions for all the systems studied. All of the results will be shown and interpreted in a subsequent section.

5.2.2 Cu+Cu Results

In heavy ion collisions, the background for the dihadron jet-like correlations is correlated with the trigger particles through the elliptic flow v_2. As discussed in Section 4.3.5, the correlation of produced particles with the reaction plane (due to elliptic flow) translates into a correlation of the form $dN/d(\Delta\phi) = B(1 + 2\langle v_2^{trig} v_2^{assoc} \rangle \cos(2\Delta\phi))$ in the two particle distributions. The background level is determined using the assumption, already mentioned when discussing background subtraction in d+Au collisions, that there is no jet contribution at the minimum of the distribution ($0.8 < |\Delta\phi| < 1.2$). The nominal values of v_2 used to determine the background modulation is the average of the results given by the two methods used by STAR to measure v_2, as discussed in Section 4.3.5. The v_2 values given by the two methods of estimating elliptic flow are used to determine the systematic uncertainties on the yields.

Figure 5.19 presents the dihadron azimuthal distributions for all centralities studied. The left panels represent the distributions using the lower trigger p_T ($4 < p_T^{trig} < 6$ GeV/c), whereas the right panels represent those for the higher trigger range ($6 < p_T^{trig} < 10$ GeV/c). The red curves represent the background obtained using the best estimate of v_2, and the green and blue curves represent the background obtained using the upper and lower limit on v_2. The extracted yields are listed in Table 5.8.

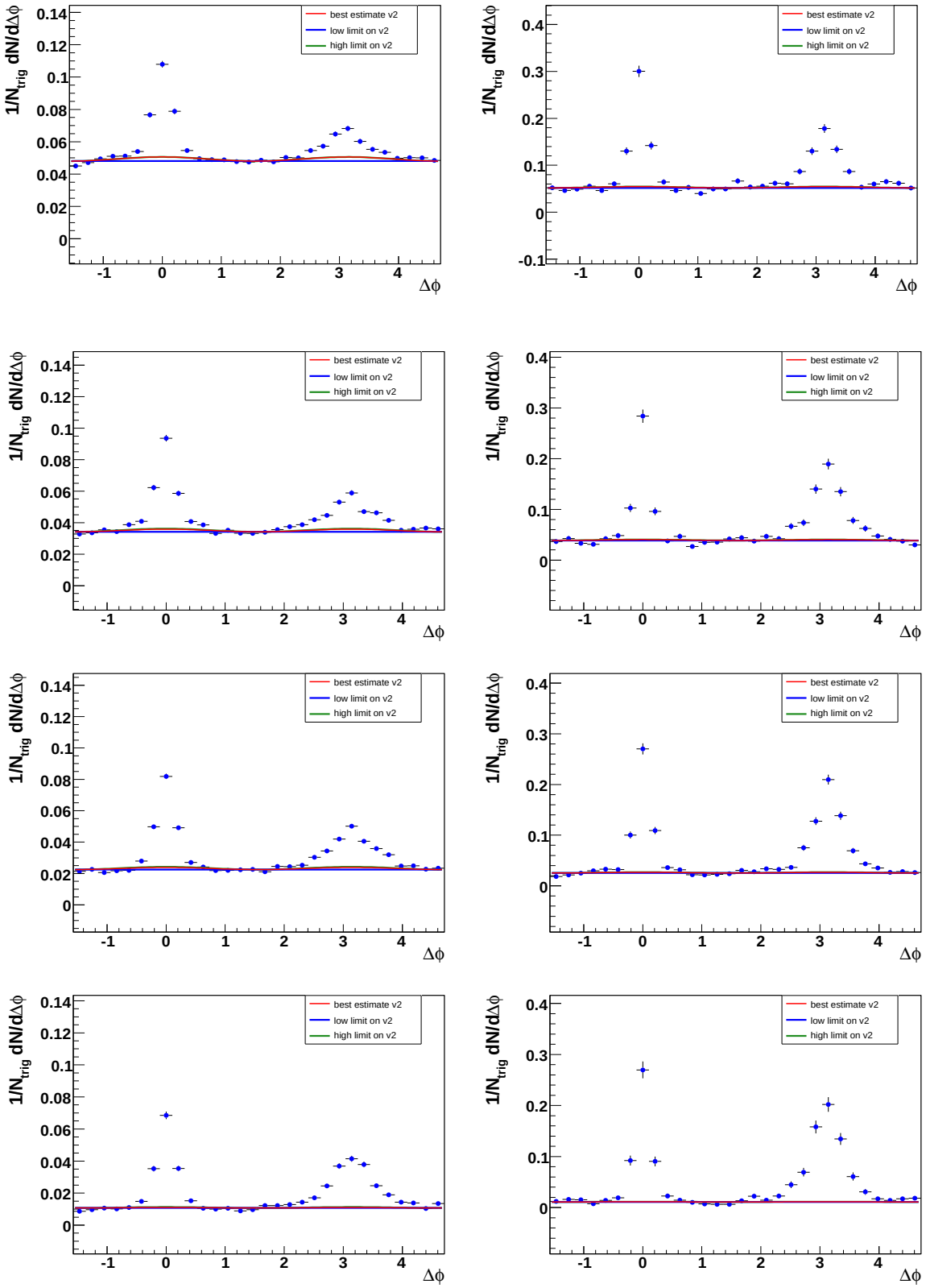

Figure 5.19: Dihadron azimuthal correlations used to extract the away-side jet-like yields for Cu+Cu collisions. Left panels: $4 < p_T^{trig} < 6$ GeV/c, $3\,\mathrm{GeV/c} < p_T^{assoc} < p_T^{trig}$, Right panels: $6 < p_T^{trig} < 10$ GeV/c, $3\,\mathrm{GeV/c} < p_T^{assoc} < p_T^{trig}$. Each row shows the distributions for a centrality class: 0-10%, 10-20%, 20-40% and 40-60% (starting from the top row).

Table 5.8: Away-side yields in Cu+Cu collisions for each kinematic range and centrality. The first error is the statistical error and the second one is the systematical error.

Centrality	Y_{away}	
	$4 < p_T^{trig} < 6$ GeV/c	$6 < p_T^{trig} < 10$ GeV/c
0-10%	$0.01444 \pm 0.0022^{+0.0040}_{-0.0000}$	$0.0857 \pm 0.0084^{+0.0043}_{-0.0000}$
10-20%	$0.0200 \pm 0.0020^{+0.0025}_{-0.0006}$	$0.1020 \pm 0.0083^{+0.0025}_{-0.0003}$
20-40%	$0.0225 \pm 0.0015^{+0.0021}_{-0.0006}$	$0.1151 \pm 0.0063^{+0.0022}_{-0.0004}$
40-60%	$0.0292 \pm 0.0016^{+0.0005}_{-0.0005}$	$0.1393 \pm 0.0075^{+0.0003}_{-0.0002}$

5.2.3 Au+Au results

The same method used for Cu+Cu collisions was applied in the study of the Au+Au away-side associated yields. The dihadron azimuthal distributions are presented in Fig. 5.20 and the corresponding yields are listed in Table 5.9.

Table 5.9: Away-side yields in Au+Au collisions for each kinematic range and centrality. The first error is the statistical error and the second one is the systematical error.

Centrality	Y_{away}	
	$4 < p_T^{trig} < 6$ GeV/c	$6 < p_T^{trig} < 10$ GeV/c
0-12%	$0.0100 \pm 0.0009^{+0.0014}_{-0.0022}$	$0.0456 \pm 0.0036^{+0.0010}_{-0.0016}$
10-20%	$0.0059 \pm 0.0016^{+0.0040}_{-0.0047}$	$0.0476 \pm 0.0064^{+0.0033}_{-0.0039}$
20-30%	$0.0109 \pm 0.0023^{+0.0041}_{-0.0048}$	$0.0756 \pm 0.0089^{+0.0035}_{-0.0042}$
30-40%	$0.0114 \pm 0.0024^{+0.0037}_{-0.0044}$	$0.0810 \pm 0.0095^{+0.0036}_{-0.0044}$
40-60%	$0.0172 \pm 0.0017^{+0.0025}_{-0.0031}$	$0.0947 \pm 0.0069^{+0.0025}_{-0.0031}$
60-80%	$0.0301 \pm 0.0019^{+0.0008}_{-0.0011}$	$0.1324 \pm 0.0091^{+0.0009}_{-0.0012}$

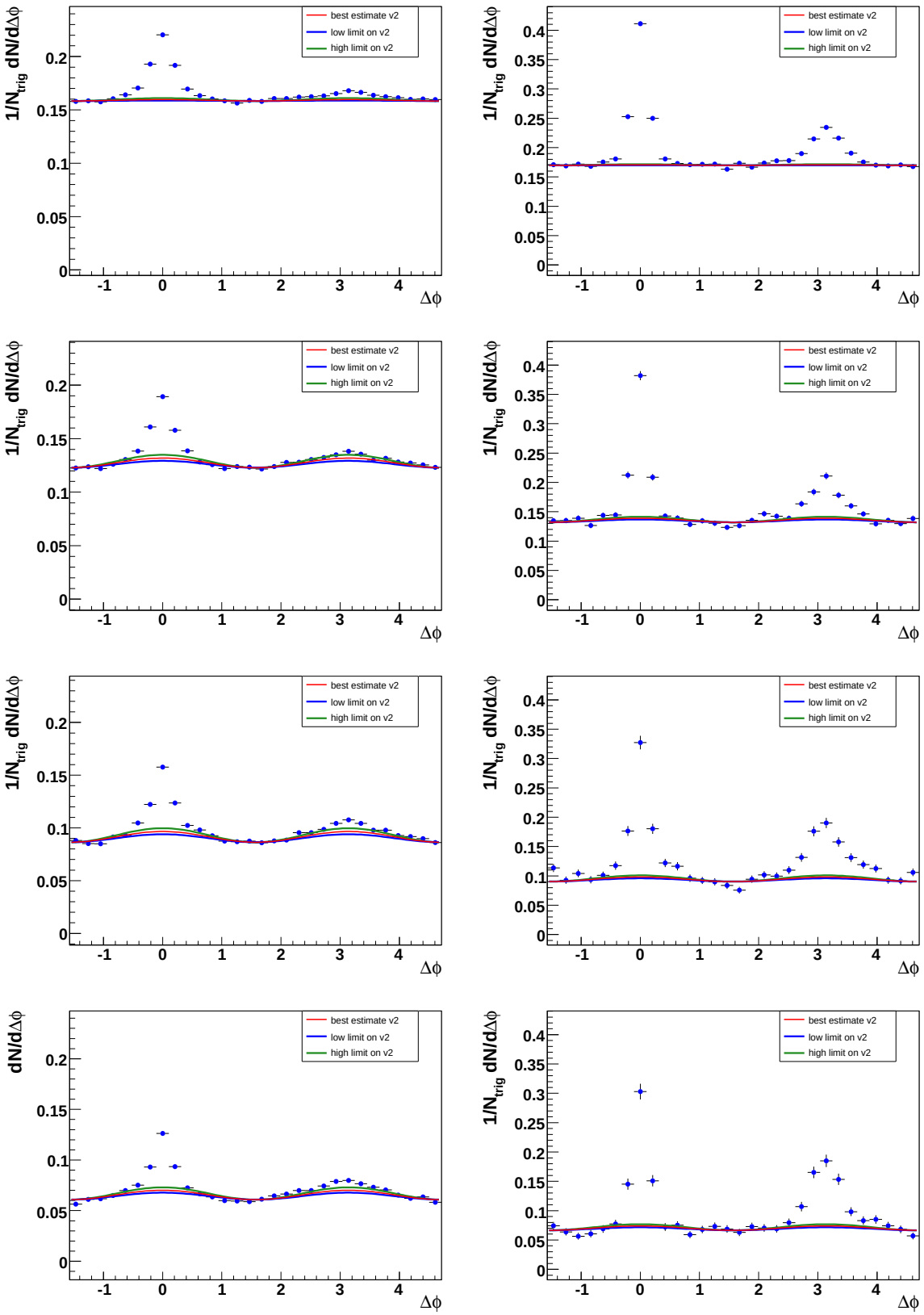
best estimate v2
low limit on v2
high limit on v2
1/N_trig dN/dΔφ
dN/dΔφ
Δφ

Figure 5.20

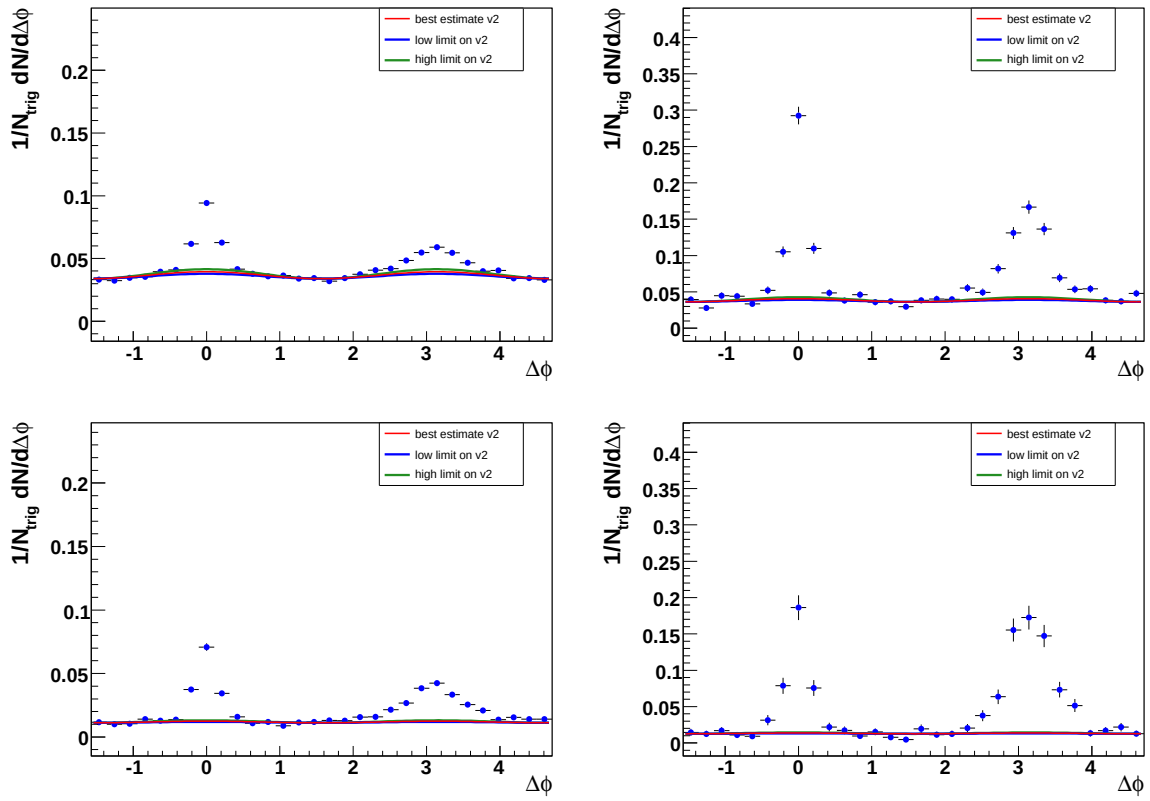

Figure 5.20: Dihadron azimuthal correlations used to extract the away-side jet-like yields for Au+Au collisions. Left panels: $4 < p_T^{trig} < 6$ GeV/c, $3\,\mathrm{GeV/c} < p_T^{assoc} < p_T^{trig}$, Right panels: $6 < p_T^{trig} < 10$ GeV/c, $3\,\mathrm{GeV/c} < p_T^{assoc} < p_T^{trig}$. Each row shows the distributions for a centrality class: 0-12%, 10-20%, 20-30%, 30-40%, 40-60% and 60-80% (starting from the top row).

5.2.4 N_{part} dependence of the away-side suppression

The extracted away-side yields were used to compute the suppression factor $I_{AA} = Y_{AA}^{away}/Y_{pp}^{away}$, where $Y_{AA(pp)}^{away}$ is the away-side dihadron correlation strength in heavy ions and proton-proton collisions, respectively. As previously mentioned, we used the experimental results from d+Au collisions as our baseline instead of those from p+p, given that there is no medium modification in d+Au collisions.

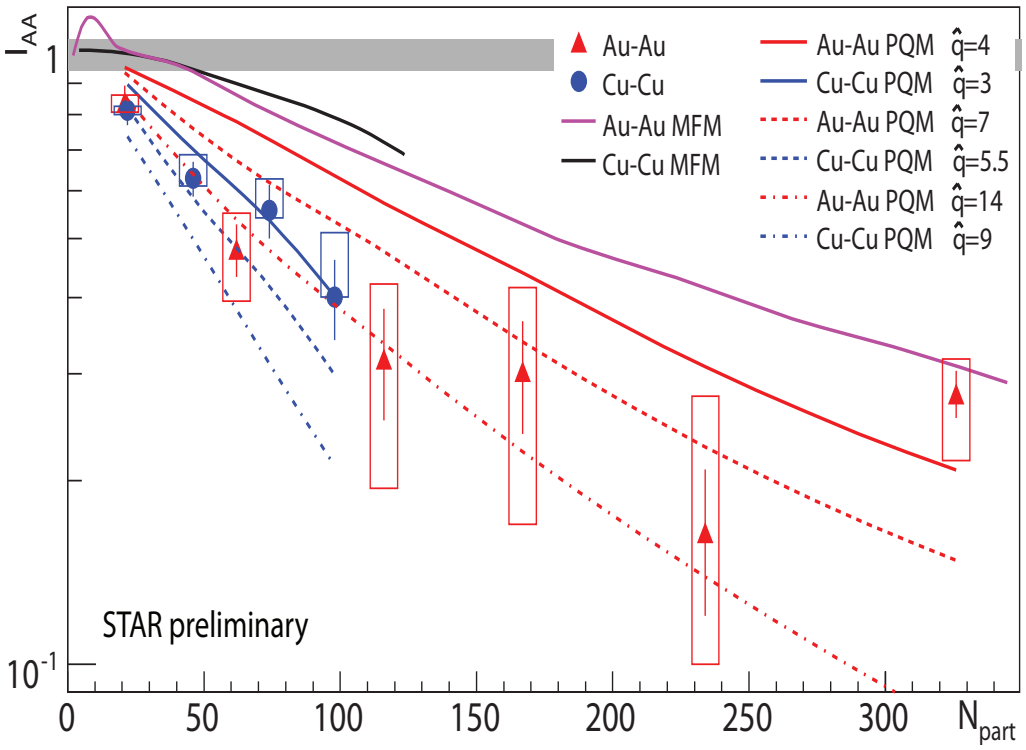

Figure 5.21: N_{part} dependence of the away-side jet yield for 4 GeV/c < p_T^{trig} < 6 GeV/c, p_T^{assoc} > 3 GeV/c. The lines represent calculations in PQM and MFM models.

Fig. 5.21 and Fig. 5.22 show the results for I_{AA} as a function of number of participants for 4 < p_T^{trig} < 6 GeV/c and 6 < p_T^{trig} < 10 GeV/c, respectively. It can be clearly seen that the away-side yield suppression increases with N_{part}, as expected. Somewhat surprisingly, the Cu+Cu results show a similar suppression at the same number of participants as the Au+Au results, despite the expected differences in path length distributions.

Figures 5.21 and 5.22 also show two model calculations that were available at the time of writing. The calculations have been performed for the same kinematic selections that are used in the data analysis. One calculation, the Parton Quenching Model (PQM) [41, 42], uses the "quenching weights" calculated by Salgado-Wiedemann [43]. The quenching weights represent the probability that a hard parton radiates an additional energy fraction ΔE in the medium due to

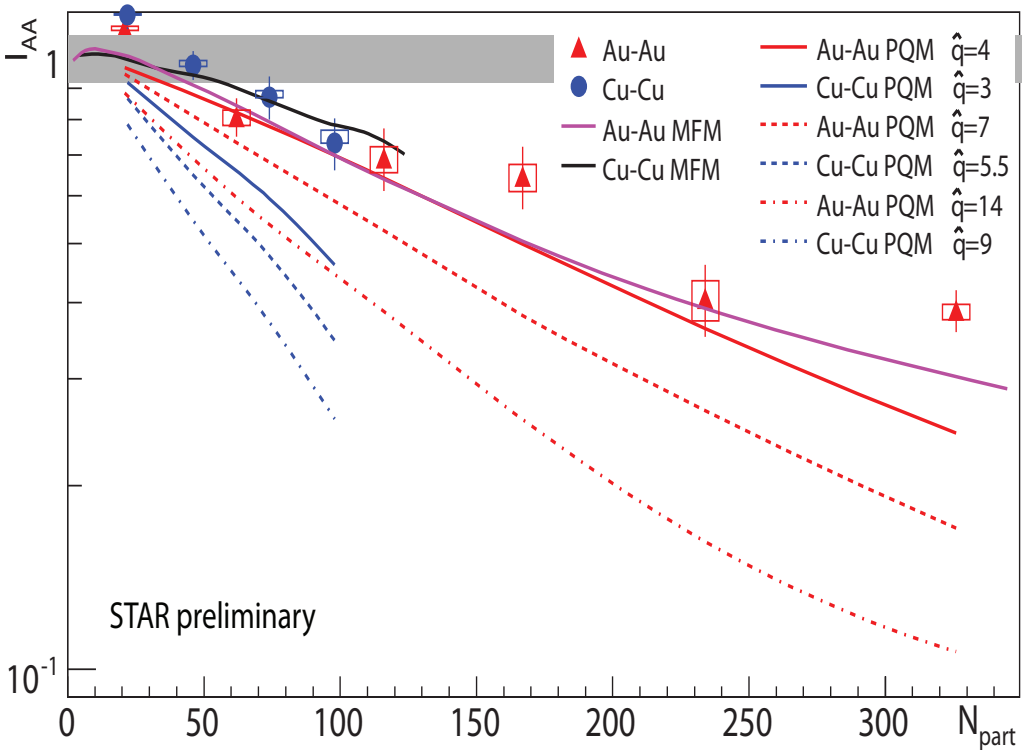

Figure 5.22: N_{part} dependence of the away-side jet yield for 6 GeV/c < p_T^{trig} < 10 GeV/c, p_T^{assoc} > 3 GeV/c. The lines represent calculations in PQM and MFM models.

scattering in spatially extended QCD matter. The quenching weights implemented in PQM are calculated in the multiple soft scattering approximation. An energetic parton produced in a hard collision undergoes, along its path in the dense medium, multiple scatterings with mean free path λ, which decreases as the medium density increases. In this multiple scattering process, the gluons radiated by the parton pick up transverse momentum k_T with respect to the parton direction and they may eventually decohere and be radiated. The scale of the energy loss is set by the characteristic energy of the radiated gluons

$$\omega_c = \hat{q}L^2/2 \tag{5.3}$$

which depends on the in-medium path length L of the parton and on the transport coefficient of the medium, $\hat{q}$. The transport coefficient is defined as the average

medium-induced transverse momentum squared transferred to the parton per unit path length, $\hat{q} = \left\langle k_T^2 \right\rangle_{medium} / \lambda$. For a static medium it is time-independent. In this approach the radiated gluon energy distribution, in an expanding medium with a $q(t)$ that decreases with time, is translated into an equivalent distribution for a static medium, with a time-averaged $\langle \hat{q} \rangle$ = constant. The overlap geometry is determined using a Glauber model calculation and the local density scales with the local density of binary collisions ρ_{coll}.

The other model used for our comparison, which we will refer to as the Modified Fragmentation Model (MFM), uses a next-to-leading order QCD calculation with modified fragmentation functions [25]. The model assumes that the effect of the final-state interaction between the produced parton and the bulk medium can be described by the effective medium-modified fragmentation functions.

$$\begin{aligned} D_{h/c}(z_c, \Delta E_c, \mu^2) &= (1 - e^{-\langle \frac{L}{\lambda} \rangle}) \left[\frac{z_c'}{z_c} D^0_{h/c}(z_c', \mu^2) \right. \\ &\left. + \langle \frac{L}{\lambda} \rangle \frac{z_g'}{z_c} D^0_{h/g}(z_g', \mu^2) \right] + e^{-\langle \frac{L}{\lambda} \rangle} D^0_{h/c}(z_c, \mu^2), \end{aligned} \tag{5.4}$$

where $z_c' = p_T/(p_{Tc} - \Delta E_c)$, $z_g' = \langle L/\lambda \rangle p_T / \Delta E_c$ are the rescaled momentum fractions, ΔE_c is the average radiative parton energy loss and $\langle L/\lambda \rangle$ is the number of scatterings. The energy loss is calculated by computing directly the radiation pattern from the finite number of Feynman diagrams for the case of few collisions, making the assumption of a thin plasma, a few mean free paths thick [44]. The total parton energy loss in a finite and expanding medium is approximated as a path integral,

$$\Delta E \approx \langle \frac{dE}{dL} \rangle_{1d} \int_{\tau_0}^{\infty} d\tau \frac{\tau - \tau_0}{\tau_0 \rho_0} \rho_g(\tau, \mathbf{b}, \mathbf{r} + \mathbf{n}\tau), \tag{5.5}$$

for a parton produced at a transverse position $\mathbf{r}$ at an initial time τ_0 and traveling along the direction $\mathbf{n}$. $\langle dE/dL \rangle_{1d}$ is the average parton energy loss per unit length in a 1-d expanding medium with an initial uniform gluon density ρ_0 at τ_0. The model considers a hard-sphere geometry where the density scales with the local participant density ρ_{part} [45]. Both models were tuned to high-p_T results from central Au+Au collisions [39].

For the lower trigger selection, 4 GeV/$c < p_T^{trig} <$ 6 GeV/c, both models predict a smaller suppression than observed in the data (with a slightly better match for the PQM model). The disagreement between the models and the data suggests that the effect of kinematic limits (energy loss cannot be larger than the jet energy) and non-perturbative effects, which are not explicitly treated in the model, are significant in this p_T-range. For the higher trigger p_T range, 6 GeV/$c < p_T^{trig} <$ 10 GeV/c, a better agreement between the data and the MFM model is observed. There is a striking difference between the system size dependence in the MFM, where an approximate scaling of I_{AA} with N_{part} is observed and in PQM, where no such scaling is observed. Future model studies should clarify whether the different scaling behavior in MFM and PQM is mainly a result of the different quenching formalisms or rather due to differences between the medium density models.

A deeper insight into the energy loss mechanism is gained studying the away-side dihadron fragmentation functions. Fig. 5.24 shows the away-side yield as a function of $z_T = p_T^{assoc}/p_T^{trig}$. The lower panel of Fig. 5.24 shows the z_T-dependence of I_{AA}. The away-side suppression is approximately independent of z_T in the measured range, indicating that the momentum distribution of fragments along the jet axis is not modified by energy loss. This again indicates that partons fragment in the vacuum after energy loss. Also shown in Fig. 5.24 are calculations in the Modified Fragmentation Model [45], which agree with the results within the present statistical uncertainties.

We also investigated the behavior of the di-hadron fragmentation functions as a function of N_{part}Ḟig. **??** shows the away-side di-hadron fragmentation functions for Cu+Cu and Au+Au collisions with similar N_{part}. The red data points are the results in collisions with $N_{part} \sim 100$ and the blue ones correspond to collisions with $N_{part} \sim 20$. The results show the same behavior in the two systems for similar number of participants, consistent with our results on the away-side yield suppression.

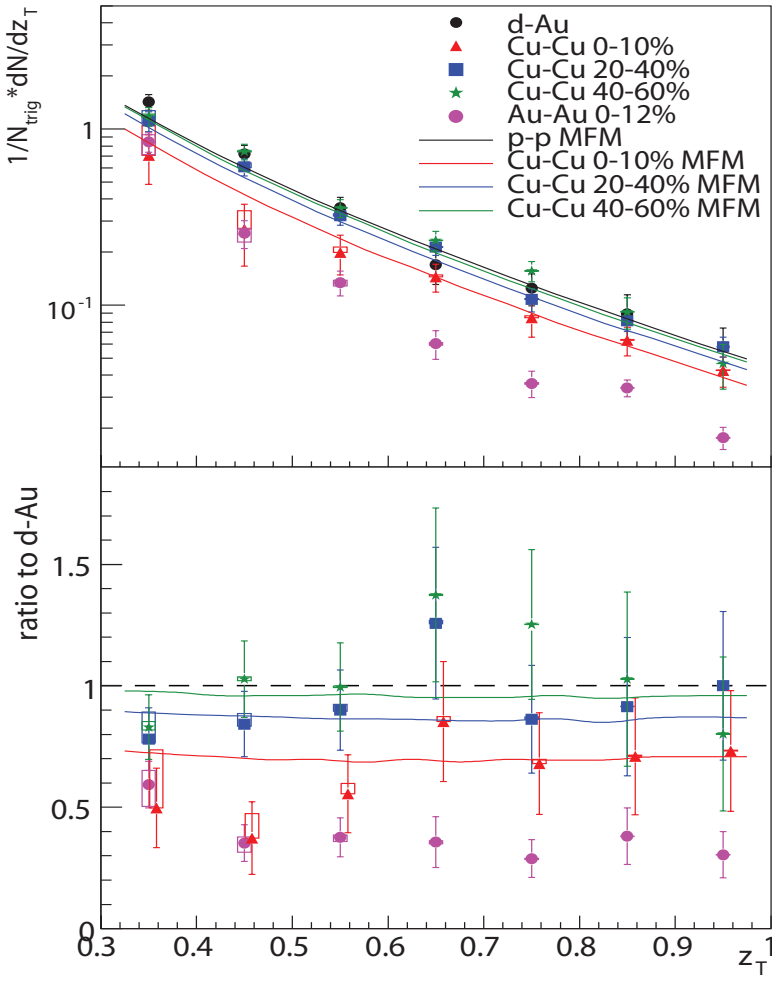

Figure 5.23: Away-side di-hadron fragmentation function and I_{AA} for 6 < p_T^{trig} <10 GeV/c. The lines represent calculations in the MFM model.

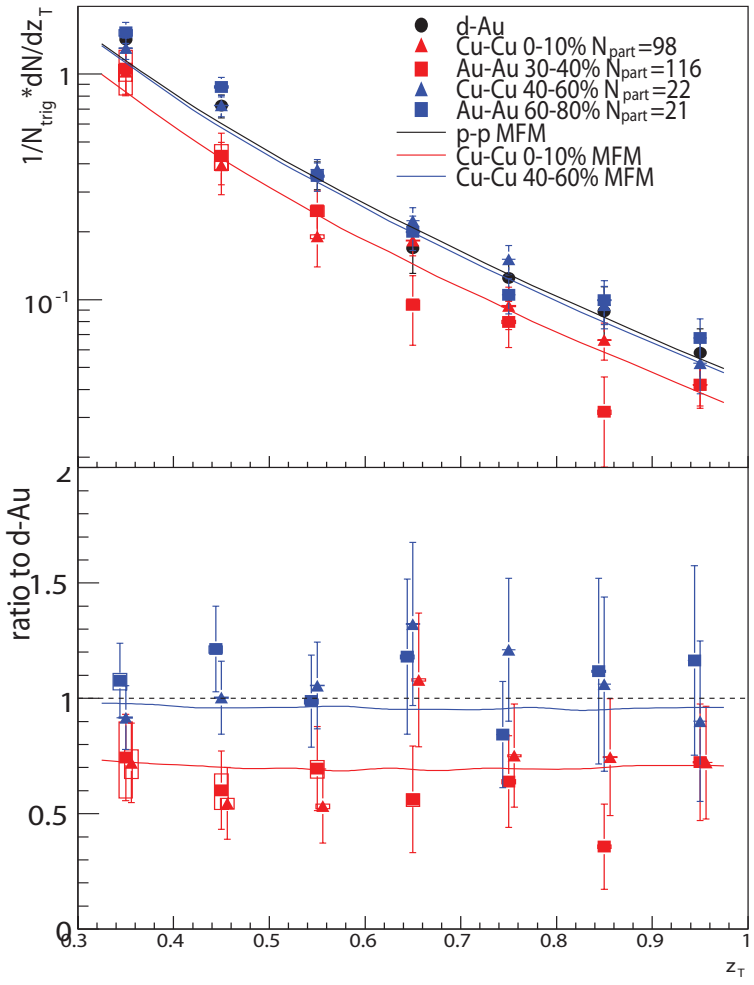

Figure 5.24: Away-side di-hadron fragmentation function and I_{AA} for 6 < p_T^{trig} <10 GeV/c for Cu+Cu and Au+Au collisions with similar N_{part} . The lines represent calculations in the MFM model.

Chapter 6

Conclusions and Outlook

6.1 Conclusions

After the discovery of the phenomenon of jet quenching at RHIC, the focus has been on studying the properties of the medium formed in heavy ion collisions at high energy. The highly energetic partons resulting from hard scatterings in the initial stages of the collisions are used as probes for investigating the properties of the medium created. The partons then fragment into jets of hadrons and we look for modification of the properties of these jets. This is mostly done at RHIC by comparing the various experimental observations in p+p, d+Au and Au+Au collisions. The properties of the medium that we would like to study includes the energy density achieved in the collisions, velocity of sound in the medium, insights into partonic interactions and the mechanism of energy loss of the partons, collectivity, possibility of achieving thermalization and the effect of the medium on the mechanism of particle production. While the suppression of high-p_T single hadron spectra is a useful tool in quantifying the amount of energy loss, correlations between produced particles provide us with more detailed information on the parton-medium interaction.

Using single hadron spectra suppression together with the away-side suppression in dihadron correlations is a powerful way to constrain models and determine

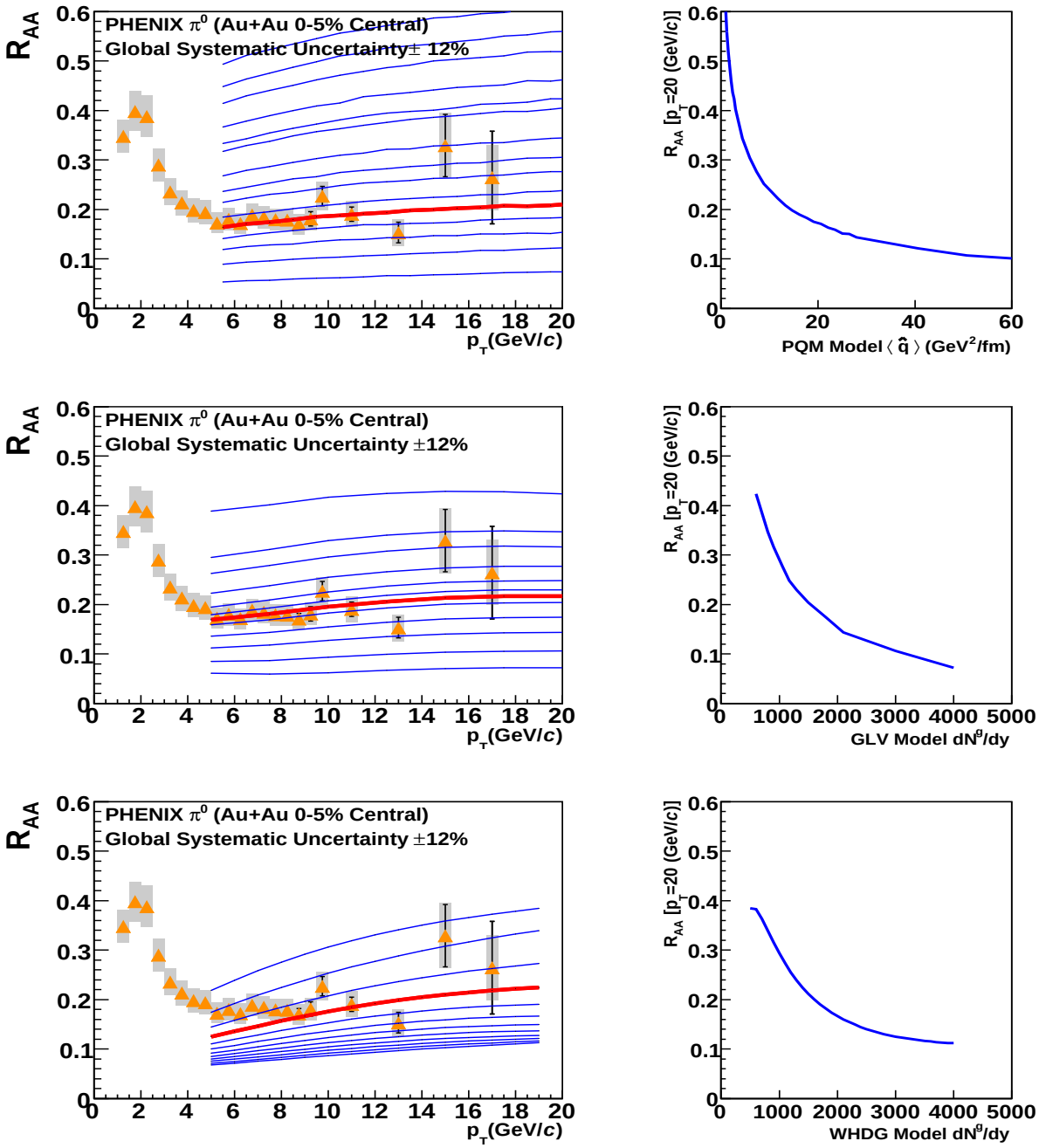

Figure 6.1: The left panels show the PHENIX π^0 nuclear suppression factor R_{AA} as a function of transverse momentum for 0-5% Au+Au collisions at $\sqrt{s_{NN}}$=200 GeV. Also shown are predictions from the (upper) PQM [42], (middle) GLV [23], and (lower) WHDG [46] models with various parameters. The red lines indicate the best fit cases of (upper) $\langle\hat{q}\rangle$=13.2, (middle) dN^g/dy = 1400, and (lower) dN^g/dy = 1400 (where dN^g/dy is the initial gluon density). The right panels show (upper) the PQM nuclear suppression factor at p_T = 20 GeV/c as a function of $\hat{q}$, (middle) the GLV nuclear suppression factor at p_T = 20 GeV/c as a function of dN^g/dy, and (lower) the WHDG nuclear suppression factor at p_T = 20 GeV/c as a function of dN^g/dy.

Table 6.1: Best fit parameters for the PQM, GLV, and WHDG calculations.

Model	Parameter value
PQM	$\langle\hat{q}\rangle = 13.2^{+2.1}_{-3.2}\,\mathrm{GeV}^2/\mathrm{fm}$
GLV	$dN^g/dy = 1400^{+270}_{-150}$
WHDG	$dN^g/dy = 1400^{+200}_{-375}$

the initial gluon density of the medium formed in heavy ion collisions. As mentioned in Section 5.2, the two observables have different geometrical biases (see Fig. 5.17). The use of the two therefore imposes stricter constraints and can help discriminate between the available models, revealing the mechanisms and magnitude of energy loss and properties of the medium. Using high-p_T single hadron suppression and comparing with several models, the energy density of the medium inferred by the various models was extracted by the PHENIX collaboration [47]. Fig. 6.1 shows a comparison of three energy loss models with experimental data on the π^0 nuclear suppression factor R_{AA} as a function of p_T. The WHDG model is based on the same formulation of radiative energy loss as GLV, but also incorporates collisional energy loss. The model parameters are varied and a log-likelihood minimization is performed to determine the parameters that best fit the data. The values obtained are listed in Table 6.1.

This is an important step in quantifying the properties of the medium formed in heavy ion collisions, however we showed in Fig. 5.22 that the PQM calculations do not reproduce the system (Au+Au vs Cu+Cu) and N_{part} dependence for the away-side yield suppression in dihadron correlations. The present data therefore puts constraints on the models and indicates the need to investigate the reasons for the models' failure to describe the system size dependence. By comparing to these data, the collision geometry description and density scaling with collision system can be better understood and implemented in the models. One can then use both the single hadron suppression and away-side correlation yield suppression data to determine quantitative values for the medium properties.

There is an obvious need for improvement in the models so that they can

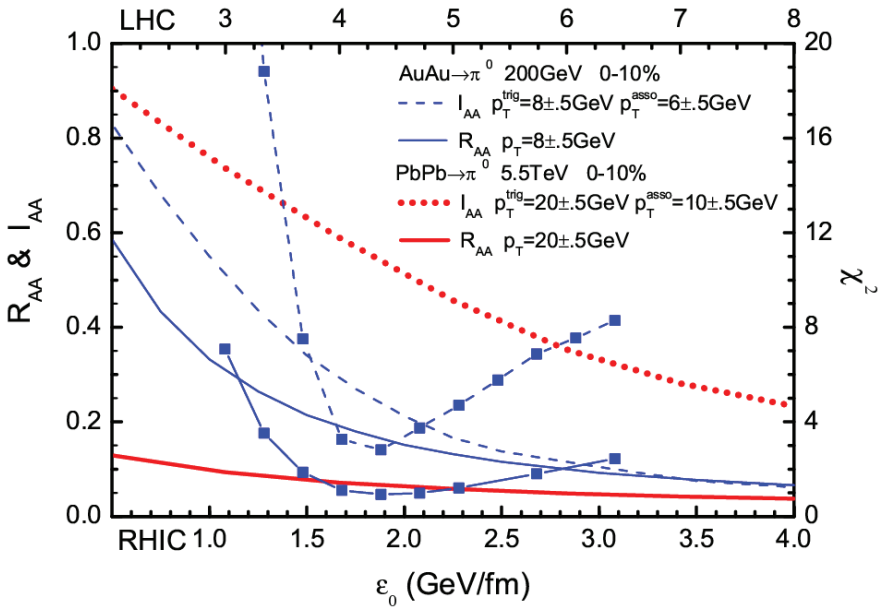

Figure 6.2: χ^2 of R_{AA} and I_{AA} as a function of the initial energy density of the medium ϵ_0.

accurately describe a multitude of available data and extract reliable results for the medium properties. At the moment, the Modified Fragmentation Model is the only calculation available that describes relatively well the data presented in this work, and gives consistent results for both single hadrons and dihadron correlations. A χ^2 analysis of the model curves for the Au+Au data [45] is presented in Fig. 6.2. The initial energy density ϵ_0 extracted from the single hadron data has approximately the same value as the one extracted from dihadron correlation data. The ϵ_0 obtained corresponds to a transport coefficient $\hat{q} = 2.8 \pm 0.3 \text{GeV}^2/\text{fm}$. This is a very different value than the value inferred from PQM in [47]. It underscores the need for the theoretical community to produce calculations in an attempt to reproduce the various experimental observables available. Since the models implement different energy loss calculations, different geometry descriptions, and density scaling, one cannot use a single observable to test the various assumptions. An attempt to describe the whole spectrum of data available on the suppression of single hadron and dihadron correlations can point us in the right direction and allow us to make a robust determination of the medium properties.

6.2 Outlook

The study of dihadron correlations has been a very useful tool for gaining important information about parton energy loss, but it definitely has its limitations. Dihadron correlations triggered by a high p_T hadron have a certain geometrical bias. Also, one cannot measure the fragmentation functions since the energy of the jet is not measured. We thus have resorted to using the "dihadron fragmentation functions" as a way to compare with theory and investigate in more detail the behavior of fragmented hadrons.

A way to circumvent these difficulties is to study γ-hadron correlations. Selecting direct γs, that originate in the hard scattering processes $q + g(\bar{q}) = \gamma + q(g)$, allows us to have a good measure of the jet energy. The energy of the parton generating the jet is balanced by the photon energy, and since the photon does not interact with the colored medium that it traverses, we can directly measure it and hence assess the jet energy. The fact that the direct photons are immune to the color forces in the created medium and thus do not suffer energy loss has another important experimental implication: selecting high-p_T photons does not create a geometrical bias, since the photons are unaffected by the amount of matter they traverse. The limiting factor of this type of study is the available statistics, since the gamma-jet processes have a much lower cross-section than the di-jet ones. The use of the Electromagnetic Calorimeter for triggering on events with high energy deposited in the EMCAL towers (caused mainly by γs or π^0s) improves tremendously the available statistics, allowing for the first γ-hadron correlation studies at RHIC [48]. Fig. 6.3 shows I_{AA} for the away-side hadron yield correlated with direct γ triggers. Within the current uncertainty I_{AA} agrees with the theoretical calculations using the Modified Fragmentation Model. This constitutes just the beginning of the γ-hadron correlation studies. With the factor of ten higher luminosities at RHIC II (the upgrade for RHIC), the statistics will allow us to distinguish between theoretical predictions.

The study of jets in high energy $e^+ + e^-$ and $p + p(\bar{p})$ collisions has a long tradition of well understood and tested methods. They involve jet algorithms that

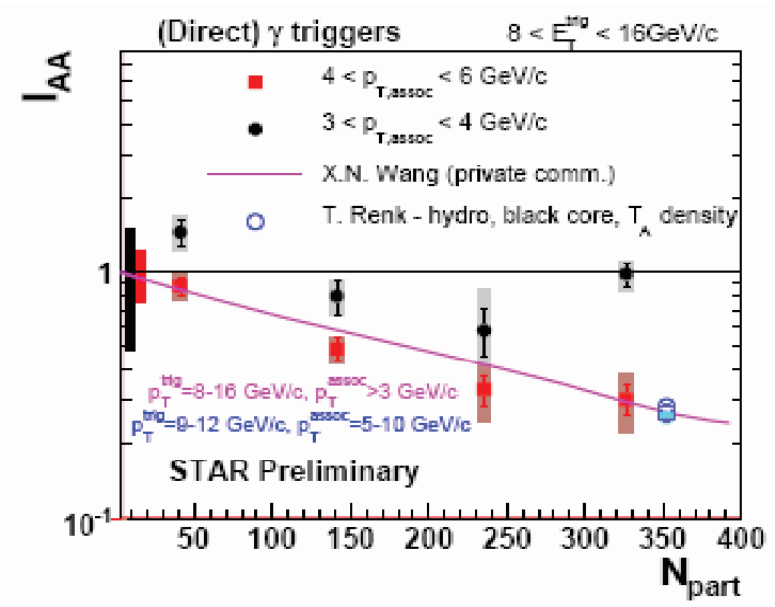

Figure 6.3: I_{AA} for direct γ triggers. The black and red boxes on the left axis, around the I_{AA} value of 1, show the scale uncertainty due to p + p measurements.

identify clusters of particles that compose a jet and reconstruct the jet direction and energy on an event-by-event basis. Unfortunately the high multiplicity and background levels in heavy ion collisions at RHIC have not permitted the use of such algorithms so far. The study of jets in heavy ion collisions at the new Large Hadron Collider at CERN will benefit from much higher jet rates, thus allowing the study of higher momentum jets. The jet particles will have momenta much above the soft particles constituting the bulk and therefore will be much better suited for the jet reconstruction algorithms. The experiments at LHC, especially CMS and ATLAS, have high granularity electromagnetic calorimeters that will enable them to have good resolution of the jet energy. The US component of the ALICE experiment (ALICE-USA) is also building an electromagnetic calorimeter to be installed in ALICE, providing a major contribution to the ALICE jet study program.

The excitement of the approaching start date of LHC has spurred much theoretical research, and there have been major improvements in jet algorithms, especially targeted for high background events. A study of the possibility of applying these improved algorithms at STAR is under way. The increased luminosity at RHIC II

will allow for more detailed measurements with enough precision to distinguish between model calculations and extract reliable values for the medium properties. After starting out as a discovery facility, aimed at creating the quark gluon plasma, RIHC has transitioned into an exploratory mode, aimed at investigating and quantifying the properties, many times surprising, of the new form of matter created. The start of LHC, with much higher collision energies ($\sqrt{s_{NN}}$ = 5.5 TeV for Pb+Pb collisions), will open new opportunities.

Appendix A

v_2 parameterization

The nominal values of v_2 used to determine the background modulation is the average of the results given by the two methods used by STAR to measure v_2. For Au+Au collisions these are the 4-particle cummulant method ($v_2\{4\}$) and the reaction plane method ($v_2\{RP\}$), whereas for Cu+Cu the two methods are the reaction plane using FTPC tracks ($v_2\{FTPC\}$) and the CuCu-pp method($v_2\{CuCu-pp\}$).

The parametrization form for $v_2\{FTPC\}$ is $a * p_T^b * e^{-(p_T/c)^d}$, where the coefficients are given in Table A.1 for each centrality. The parametrization form for $v_2\{CuCu-pp\}$ is $a * p_T^b * e^{-(p_T/c)^d}$ for $p_T < 4$ GeV/c, and c_0 (const.) for $p_T < 4$ GeV/c. The parameters are given in Table A.2.

The parametrization for Au+Au collisions uses Landau functions with the parameters listed in Table A.3, where par0 is the normalization coefficient, par1 is the

Table A.1: Coefficients of $v_2\{FTPC\}$ parametrization for each centrality.

centrality	a	b	c	d
0-10%	0.3641	1.6377	0.3548	0.5294
10-20%	0.1841	1.3955	1.3097	0.7639
20-30%	0.2463	1.4885	1.0709	0.7472
30-40%	5.0449	2.3212	0.0340	0.3998
40-50%	0.1023	0.7419	4.5000	2.3333
50-60%	0.2169	1.5022	1.4147	0.9866

Table A.2: Coefficients of $v_2\{FTPC\}$ parametrization for each centrality.

centrality	a	b	c	d	c_0
0-10%	0.5036	1.518	0.3562	0.5608	0.09763
10-20%	0.1187	0.9754	2.78	1.219	0.1184
20-30%	0.105	0.9408	3.085	1.749	0.09306
30-40%	0.09731	0.9435	3.255	1.707	0.1184
40-50%	0.0768	0.8618	3.326	2.531	0.1033
50-60%	0.05756	0.7992	3.171	3.419	0.07779

Table A.3: Coefficients of v_2 parametrization in Au+Au collisions. The parameters depend on centrality via the parameter $c = 10 - centralitybin$ - where the $centralitybin$ is 1 for most central 0-5%collisions and 9 for most peripheral 70-80%.

	$v_2\{4\}$	$v_2\{RP\}$
par0	$0.2618 + 0.3735 \cdot c - 0.0444 \cdot c^2$	$0.759 + 0.278 \cdot c - 0.0367 \cdot c^2$
par1	3.1	$4.11 - 0.0934 \cdot c$
par2	1.5	$2.623 - 0.15 \cdot c$

most probable value and par2 is the width (λ).

Appendix B

Efficiency parameterizations

The efficiency has been calculated by simulating particle tracks and embedding them in a real STAR event. For the d+Au data a constant function $\epsilon(\eta, p_T)$=0.89 was used. For Cu+Cu and Au+Au collisions the efficiency as a function of (η,p_T) has been fitted with a two-dimensional function. The functional form used for Cu+Cu is

$$\epsilon(\eta, p_T) = c_0 + c_1 * \eta^2 + c_2 * \eta^4 + c_3 * \eta^6 + c_4 * \eta^8 + c_5 * e^{c_6 * p_T^{c_7}} \tag{B.1}$$

and the form used for the Au+Au collisions is

$$\epsilon(\eta, p_T) = c_0 + c_1 * \eta^2 + c_2 * \eta^4 + c_3 * \eta^6 + c_4 * \eta^8 + c_5 * e^{c_6 * p_T} \tag{B.2}$$

The parameters obtained by fitting the efficiency in Cu+Cu and Au+Au are listed in Tables B.1 and B.2.

Table B.1: Coefficients of the efficiency parametrization for each centrality in Cu+Cu collisions.

centrality	c_0	c_1	c_2	c_3	c_4	c_5	c_6	c_7
0-10%	0.0116	0.0049	0.2082	-0.3322	-0.06757	0.8654	0.1333	0.9890
10-20%	0.0061	0.2059	-0.6794	0.9429	-0.6623	0.8735	0.1206	0.9330
20-30%	0.0132	-0.0160	0.1636	-0.1823	-0.1309	0.8642	0.1503	1.1071
30-40%	0.0097	-0.0064	0.3011	-0.5329	0.0753	0.8692	0.1269	0.9921
40-50%	0.0261	-0.1003	-0.0951	0.9617	-0.9999	0.8608	0.1511	1.1616
50-60%	0.0095	0.1225	-0.5110	1	-0.8187	0.8606	0.1970	1.3211

Table B.2: Coefficients of the efficiency parametrization for each centrality in Au+Au collisions.

centrality	c_0	c_1	c_2	c_3	c_4	c_5	c_6
0-12%	0.7605	0.0620	-0.0793	0.3313	-0.5532	-0.2101	-0.8939
10-20%	0.8137	0.0142	0.0398	0.1117	-0.3903	-0.1373	-0.5700
20-30%	0.8230	0.0222	0.0365	0.0217	-0.2980	-0.1636	-0.8678
30-40%	0.8402	0.0189	-0.0583	0.2760	-0.4692	-0.1365	-0.7043
40-60%	0.8505	-0.0525	0.3364	-0.5114	0.0293	-0.1845	-1.0971
60-80%	0.8693	-0.0390	0.2331	-0.3051	-0.0951	-0.1061	-0.7001

Bibliography

[1] Siegfried Bethke. Alpha(s) 2002. 2002.

[2] F. Karsch. Lattice results on QCD thermodynamics. *Nucl. Phys.*, A(698):199, 2002.

[3] Michael L. Miller. *Measurement of Jets and Jet Quenching at RHIC*. PhD thesis, Yale University, New Haven, CT, 2004.

[4] S. S. Adler et al. Systematic studies of the centrality and $\sqrt{s_{NN}}$ dependence of the $dE_T/d\eta$ and $dN_{ch}/d\eta$ in heavy ion collisions at midrapidity. *Phys. Rev.*, C(71):034908, 2005.

[5] J. Adams et al. Experimental and theoretical challenges in the search for the quark gluon plasma: the STAR collaboration critical assessment of the evidence from RHIC collisions. *Nucl. Phys.*, A(757):102, 2005.

[6] J. Sollfrank E. Schnedermann and U. Heinz. Thermal phenomenology of hadrons from 200A GeV S+S collisions. *Phys. Rev.*, C(48):2462, 1993.

[7] K. Adcox et al. Flow measurements via two-particle azimuthal correlations in Au+Au collisions at $\sqrt{s_{NN}}$ = 130 GeV. *Phys. Rev. Lett.*, (89):212301, 2003.

[8] E. Shuryak. Why does the quark-gluon plasma at RHIC behave as a nearly ideal fluid. *Prog. Part. Nucl. Phys.*, (53):273, 2004.

[9] J. Adams et al. Particle-type dependence of azimuthal anisotropy and nuclear modification of particle production in Au+Au collisions at $\sqrt{s_{NN}}$=200 GeV. *Phys. Rev. Lett.*, (92):052302, 2004.

[10] C. Adler et al. Identified particle elliptic flow in Au+Au collisions at $\sqrt{s_{NN}}$ = 130 GeV. *Phys. Rev. Lett.*, (87):182301, 2001.

[11] C. Nonaka R.J. Fries, B. Muller and S.A. Bass. Hadron production in heavy ion collisions: Fragmentation and recombination from a dense parton phase. *Phys. Rev.*, C(68):044902, 2003.

[12] C.M. Ko V. Greco and P. Levai. Parton coalescence at RHIC. *Phys. Rev.*, C(68):034904, 2003.

[13] R. C. Hwa and C. B. Yang. Recombination of shower partons at high p_T in heavy-ion collisions. *Phys. Rev.*, C(70):024905, 2004.

[14] J. Adams et al. Azimuthal anisotropy in Au+Au collisions at $\sqrt{s_{NN}} = 200$ GeV. *Phys. Rev.*, C(72):014904.

[15] K. Adcox et al. Formation of dense partonic matter in relativistic nucleus-nucleus collisions at RHIC: Experimental evaluation by the PHENIX collaboration. *Nucl. Phys.*, A(757):184, 2005.

[16] D. Antreasyan et al. Production of hadrons at large transverse momentum in 200-, 300-, and 400-GeV p-p and p-nucleus collisions. *Phys. Rev.*, D(19):764, 1979.

[17] M. Arneodo. Nuclear effects in structure functions. *Phys. Rept.*, 240:301, 1994.

[18] C. Adler et. al. Disappearance of back-to-back high-p_T hadron correlations in central Au+Au collisions at $\sqrt{s_{NN}}$=200 GeV. *Phys. Rev. Lett.*, 90.

[19] R. Baier, Yuri L. Dokshitzer, Alfred H. Mueller, S. Peigne, and D. Schiff. Radiative energy loss of high energy quarks and gluons in a finite-volume quark-gluon plasma. *Nucl. Phys.*, B483:291–320, 1997.

[20] U. A. Wiedemann A. Kovner. Gluon radiation and parton energy loss. *Quark Gluon Plasma*, 3, 2003.

[21] X.-N. Wang B.-W. Zhang M. Gyulassy, I. Vitev. Jet quenching and radiative energy loss in dense nuclear matter. *Quark Gluon Plasma*, 3, 2003.

[22] M. Djordjevic S. Wicks, W. Horowitz and M. Gyulassy. Elastic, inelastic, and path length fluctuations in jet tomography. *Nucl. Phys.*, A(784):426, 2007.

[23] M. Plumer X.-N. Wang, M. Gyulassy. Landau-Pomeranchuk-Migdal effect in QCD and radiative energy loss in a quark-gluon plasma. *Phys. Rev.*, D(51):3436, 1995.

[24] B. G. Zakharov R. Baier, D. Schiff. Energy loss in perturbative QCD. *Ann. Rev. Nucl. Part. Sci.*, (50):37, 2000.

[25] X.-N. Wang. *Phys. Lett.*, B(595):165, 2004.

[26] F. Bergsma et al. The STAR detector magnet subsystem. *Nucl. Inst. Meth.*, A(499):633–639, 2003.

[27] T. Ludlam. Overview of experiments and detectors at RHIC. *Nucl. Inst. Meth.*, A(499):428–432, 2003.

[28] F.S. Bieser et al. The STAR trigger. *Nucl. Inst. Meth.*, A(499):766–777, 2003.

[29] M. Anderson et al. The STAR time projection chamber: a unique tool for studying high multiplicity events at RHIC. *Nucl. Inst. Meth.*, A(499):659–678, 2003.

[30] M. Anderson et al. A readout system for the STAR time projection chamber. *Nucl. Inst. Meth.*, A(499):679–691, 2003.

[31] M. Hansroul R. Brun, R. Hagelberg and J. C. Lassalle. Technical report. *CERN-DD-78-2-REV*, CERN.

[32] Mark Horner. *Systematic Studies of Low- and Intermediate-p_T Correlated Angular Distributions in Au+Au Collisions at $\sqrt{s_{NN}}$ = 200 GeV from the STAR Experiment*. PhD thesis, University of Capetown, 2007.

[33] B. I. Abelev et al. Mass, quark-number, and $\sqrt{s_{NN}}$ dependence of the second and fourth flow harmonics in ultrarelativistic nucleus-nucleus collisions. *Phys. Rev.*, C(75):054906, 2007.

[34] STAR Collaboration. Intra-jet correlations in high energy nuclear collisions. *Phys. Rev.*, C(submitted for publication), 2008.

[35] C. Nattrass for the STAR Collaboration. System size dependence of strange particle correlations in Cu+Cu and Au+Au collisions at $\sqrt{s_{NN}}$ = 200 GeV. *J. Physics*, J(35), 2007.

[36] A. M. Poskanzer and S. A. Voloshin. Methods for analyzing anisotropic flow in relativistic nuclear collisions. *Phys. Rev.*, C(58):1671, 1998.

[37] P.M. Dinh N. Borghini and J.-Y. Ollitrault. Flow analysis from multiparticle azimuthal correlations. *Phys. Rev.*, C(64):054901, 2001.

[38] P.M. Dinh N. Borghini and J.-Y. Ollitrault. A new method for measuring azimuthal distributions in nucleus-nucleus collisions. *Phys. Rev.*, C(63):054906, 2001.

[39] J. Adams et al. Direct observation of dijets in central Au+Au collisions at $\sqrt{s_{NN}}$ = 200 GeV. *Phys. Rev. Lett.*, 97:162301, 2006.

[40] T. Renk and K. Eskola. Prospects of medium tomography using back-to-back hadron correlations. *Phys. Rev.*, C(75):054910, 2007.

[41] A. Dainese, C. Loizides, and G. Paic. Leading-particle suppression in high energy nucleus-nucleus collisions. *Eur. Phys, J. C*, 38:461–474, 2005.

[42] Constantin Loizides. High transverse momentum suppression and surface effects in Cu+Cu and Au+Au collisions within the PQM model. *Eur. Phys, J. C*, 49:339, 2007.

[43] Carlos A. Salgado and Urs Achim Wiedemann. Calculating quenching weights. *Phys. Rev. D*, 68:014008, 2003.

[44] M. Gyulassy, P. Levai, and I. Vitev. Reaction operator approach to non-abelian energy loss. *Nucl. Phys. B*, 594:371, 2001.

[45] Hanzhong Zhang, Joseph F. Owens, Enke Wang, and Xin-Nian Wang. 'di-hadron tomography of high-energy nuclear collisions in next-to-leading order perturbative QCD. *Phys. Rev. Lett.*, 98(21):212301, 2007.

[46] Simon Wicks, William Horowitz, Magdalena Djordjevic, and Miklos Gyulassy. Elastic, inelastic, and path length fluctuations in jet tomography. *Nucl. Phys. A*, 784:426, 2007.

[47] A. Adare et al. Quantitative constraints on the opacity of hot partonic matter from semi-inclusive single high transverse momentum pion suppression in Au+Au collisions at $\sqrt{s_{NN}}$ = 200 GeV. *Phys. Rev.*, C(77):064907, 2008.

[48] Ahmed Hamed for the STAR Collaboration. γ-hadron azimuthal correlations in STAR. *J. Physics*, G, 2008.